Experimental Investigation and Modelling of Incidents in Liquid Helium Cryostats

zur Erlangung des akademischen Grades eines
DOKTORS DER INGENIEURWISSENSCHAFTEN (Dr.-Ing.)

der Fakultät für Chemieingenieurwesen und Verfahrenstechnik des
Karlsruher Instituts für Technologie (KIT)

genehmigte
DISSERTATION

von
Dipl.-Ing. Carolin Zoller geb. Heidt
aus Stuttgart

Referent: Prof. Dr.-Ing. Steffen Grohmann
Korreferent: Prof. Dr.-Ing. Thomas Wetzel
Tag der mündlichen Prüfung: 11. Mai 2018

Abstract

Liquid helium is often used for the cooling of superconducting magnets. Due to the low operating temperature around 4 K and helium's low enthalpy of vaporization, the pressure inside a liquid helium cryostat increases very fast during incidents such as the venting of the insulating vacuum. Therefore, great care must be taken in the design of cryogenic safety relief devices. However, the established standards and design codes are not fully tailored to liquid helium cryogenics. For instance, safety relief devices are commonly sized under the simplifying assumption of a constant heat flux based on little experimental data, resulting in potentially over-sized devices with implications on acquisition costs and space requirements. In case of safety relief valves, over-sizing can also cause unstable operation with reduced discharge capacity. The physical mechanisms and process dynamics of failure scenarios have not yet been fully analysed. As the heat transport cannot be described purely analytically, a dynamic model requires significant simplifications, which must be parametrized and validated by experiments.

In this project, the processes during loss of insulating vacuum (LIV) in liquid helium cryostats have been studied in order to improve the reliability and efficiency of cryogenic safety relief devices. The main result of this work was the successful planning, assembly and commissioning of the cryogenic safety test facility PICARD, which stands for **P**ressure **I**ncrease in **C**ryostats and **A**nalysis of **R**elief **D**evices. With a cryogenic liquid volume of 100 L, a maximum allowable working pressure of 16 bar(g) and the capacity of measuring helium discharge mass flow rates of up to 4 kg/s, the test facility allows the systematic investigation of failure modes and incidents in cryostats under realistic conditions. An experimental method for measuring the relevant process parameters with sufficiently low uncertainties has been developed. It includes the use of 31 sensors and a data acquisition system allowing sampling rates of up to 1 kHz in order to take the process dynamics, the temperature gradients and the thermodynamic non-equilibria into account.

As part of this project, a first set of experiments at PICARD was conducted within the framework of a research and development (R&D) collaboration between the Karlsruhe Institute of Technology (KIT) and the European Organisation for Nuclear Research (CERN) established for this purpose. During these experiments, the insulating

vacuum was vented with atmospheric air or gaseous nitrogen under variation of the venting diameter, the liquid level and the set pressure in order to investigate the impact on the heat flux and hence on the process dynamics. The results of the experiments indicate large overpressures in the system during unstable safety relief valve operation. Besides this, the experimental data suggests highly dynamic heat fluxes with lower values relevant for the design of safety relief valves, yielding smaller valves with more reliable performance.

The experimental results emphasized the necessity of modelling the process dynamics during LIV. An earlier developed dynamic model was refined especially with regard to the heat and mass transfer based on the experimental data. As a result, both the shapes and the absolute values of the experimental results of LIV under very different conditions could be reproduced with good accuracy. The refined model therefore presents a significant improvement on the previous state of the art with considerable potential for further generalizations on the basis of a broader range of experimental data. The model thus represents a first promising step towards a fully general method for the sizing of cryogenic safety relief devices in the context of the ongoing German and European standardization efforts in the field of cryogenic safety.

Kurzfassung

Flüssighelium wird oft zur Kühlung supraleitender Magnete eingesetzt. Aufgrund der tiefen Betriebstemperaturen im Bereich von 4 K und der niedrigen Verdampfungsenthalpie von Helium steigt der Druck in Flüssighelium-Kryostaten bei Störungen, wie dem plötzlichen Verlust des Isoliervakuums, schnell an. Der Auslegung von Sicherheitseinrichtungen kommt in der Kryotechnik daher besondere Bedeutung zu, wobei die etablierten Regelwerke für die Dimensionierung die in der Kryotechnik und insbesondere bei Flüssighelium auftretenden Bedingungen nur unzureichend erfassen. So werden beispielsweise Sicherheitseinrichtungen häufig unter der vereinfachenden Annahme einer konstanten Wärmestromdichte auf Basis weniger experimenteller Daten ausgelegt. Dies kann zu einer Überdimensionierung der Sicherheitseinrichtungen und folglich zu erhöhten Anschaffungskosten und Platzbedarf sowie im Falle von Sicherheitsventilen zu instabilem Ventilverhalten mit reduzierter Abblasekapazität führen. Die physikalischen Mechanismen und die Prozessdynamik bei Störungen wurden bisher nicht vollständig analysiert. Da insbesondere der Wärmeübergang nicht rein analytisch modelliert werden kann, sind in einem dynamischen Modell erhebliche Vereinfachnungen nötig, welche durch Experimente parametrisiert und validiert werden müssen.

In der vorliegenden Arbeit werden die Abläufe bei Zusammenbruch des Isoliervakuums in Flüssighelium-Kryostaten studiert mit dem Ziel der Verbesserung von Zuverlässigkeit und Effizienz von Sicherheitseinrichtungen in der Kryotechnik. Das wichtigste Ergebnis dieser Arbeit war die Planung, der Aufbau und die erfolgreiche Inbetriebnahme des kryotechnischen Sicherheitsversuchsstands PICARD. Mit einem Fassungsvermögen von 100 L kryogener Flüssigkeit, einem maximalen Arbeitsdruck von 16 bar(g) und der Möglickkeit, Helium-Abblasemassenströme von bis zu 4 kg/s zu messen, ermöglicht der Versuchsstand die systematische Untersuchung von Störungen in Kryostaten unter realistischen Bedingungen. Dazu wurde eine experimentelle Methode zur Messung der relevanten Prozessparameter mit ausreichend geringer Messunsicherheit entwickelt. Diese schließt die Verwendung von 31 Sensoren und eines Datenerfassungssystems mit Abtastraten von bis zu 1 kHz ein, um Prozessdynamik, Temperaturgradienten sowie thermodynamische Ungleichgewichte zu berücksichtigen.

Als Teil des Projekts wurde eine erste Reihe von Experimenten im Rahmen einer

hierfür etablierten Kollaboration zwischen KIT und CERN durchgeführt. Dabei wurde das Isoliervakuum mit Luft oder gasförmigem Stickstoff bei Variation von Belüftungsdurchmesser, Füllstand und Einstelldruck des Sicherheitsventils geflutet, um die Auswirkungen auf die Wärmestromdichte und damit auf die Prozessdynamik zu untersuchen. Die Ergebnisse der im Rahmen dieser Arbeit durchgeführten Versuche zeigen hohe Überdrücke im System während des instabilen Ventilverhaltens. Außerdem lassen die experimentellen Daten auf hochdynamische Wärmestromdichten mit geringen Werten im für die Auslegung von Sicherheitsventilen relevanten Bereich schließen, was kleinere Ventile mit zuverlässigerer Funktion zur Konsequenz hat.

Die experimentellen Ergebnisse unterstreichen die Notwendigkeit einer Modellierung der Prozessdynamik. Ein zuvor entwickeltes dynamisches Modell wurde auf Basis der experimentellen Daten insbesondere in Bezug auf den Wärme- und Stoffübergang deutlich verfeinert. Dadurch konnten sowohl der Kurvenverlauf, als auch die Absolutwerte der Messergebnisse bei Zusammenbruch des Isoliervakuums mit guter Genauigkeit für sehr unterschiedliche experimentelle Bedingungen reproduziert werden. Daher stellt das verfeinerte Modell eine signifikante Verbesserung gegenüber dem bisherigen Stand der Technik mit großem Potential für weitere Verallgemeinerungen auf Basis von mehr experimentellen Daten dar. Das Modell ist damit ein erster wichtiger Schritt zu einem umfassenden dynamischen Modell für die Auslegung von Sicherheitseinrichtungen in der Kryotechnik im Kontext der fortwährenden deutschen und europäischen Normungsarbeit im Bereich der kryogenen Sicherheitstechnik.

Contents

CHAPTER 1

Introduction

Cryogenics refers to all phenomena, processes, techniques and apparatus occurring or used at temperatures below 120 K [1]. The *cryogenic fluids* include helium, hydrogen, neon, nitrogen, carbon monoxide, fluorine, argon, oxygen and methane, whose vapour pressure curves can be seen in Figure 1.1. Cryogenic temperatures are needed for a variety of applications, for instance for the storage and transport of fluids. Besides this, low temperatures are used for the separation of gas mixtures such as air or natural gas through cryogenic distillation. In biology and medicine, it is beneficial to preserve e.g. cells or blood plasma at cryogenic temperatures. Furthermore, low temperatures are needed to reduce thermal noise in electronics, for instance in detectors. One of the main applications of cryogenic temperatures in research and technology, however, is superconductivity [3–5].

While normal conducting materials such as copper and steel have an electrical resistivity and thus produce heat when a continuous current is applied, superconducting (sc.) materials such as NbTi and Nb_3Sn have no electrical resistivity below a material-specific critical temperature, critical current density and critical magnetic field. There are many applications of superconductivity: Cables made of high temperature sc. materials cooled with liquid nitrogen, as used for instance in the AmpaCity Project [6, 7], allow a higher power density in comparison to conventional cables. Furthermore, sc. magnets can produce strong and stable magnetic fields and at the same time do not consume electric power once the magnetic field is established [4]. An example for this application is the Large Hadron Collider (LHC) at CERN, which is a 27 km ring where proton beams at velocities close to the speed of light are bent and focused by sc. magnets before they are collided [8]. More information on sc. magnets can be found e.g. in [9–11]. In order to operate sc. magnets at higher current densities and magnetic fields, it is necessary to reduce their operating temperature. Therefore, liquid helium is the coolant of choice for many sc. applications since it has the lowest critical point of all fluids as shown in Figure 1.1.

Of the nine known isotopes of helium (He) only two isotopes are stable: helium-3

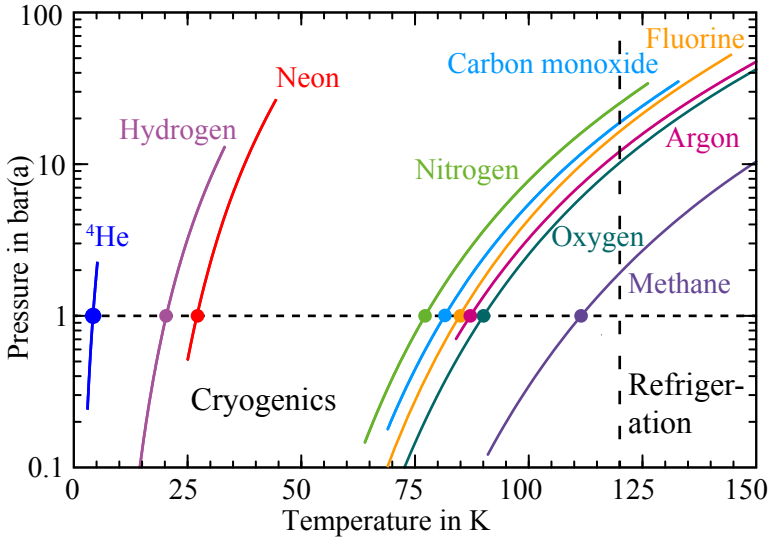

Figure 1.1: Vapour pressure curves of cryogenic fluids [2].

(^{3}He) and helium-4 (^{4}He). As shown in Figure 1.2(a), ^{3}He consists of two protons, one neutron and two electrons, while ^{4}He contains two protons, two neutrons and two electrons as illustrated in Figure 1.2(b). ^{4}He is by far the most abundant helium isotope on earth [3, 12] and the term *helium* in this work always refers to ^{4}He. Apart from ^{3}He, ^{4}He has the lowest normal boiling point of all fluids of 4.2 K[1]. The phase diagram of ^{4}He is shown in Figure 1.2(c). Because of its weak molecular interactions, helium condenses only at temperatures below $T_{\mathrm{Crit}} = 5.2\,\mathrm{K}$. It has no solid state at any temperature below $p = 25\,\mathrm{bar(a)}$, thus remaining liquid under its own vapour pressure down to the lowest temperatures. At temperatures below the *lambda temperature* $T_\lambda(1\,\mathrm{bar(a)}) = 2.17\,\mathrm{K}$, helium becomes a superfluid. The so-called He II has a normal and a superfluid phase, resulting in many special properties such as an extremely small viscosity and a thermal conductivity that exceeds the thermal conductivity of solids by many orders of magnitude [3, 12]. However, helium has a very low enthalpy of evaporation: at the normal boiling point, the enthalpy of evaporation per litre liquid volume is $\Delta h_{\mathrm{v}} = 2.6\,\mathrm{kJ/L}$, which is about 62 times smaller compared to nitrogen, and 835 times smaller compared to water [13]. Thus, liquid helium evaporates very fast even at little heat input, resulting in large pressure raise velocities and relief flow rates.

Special care must be taken in designing the pressure relief system of liquid helium cryostats [14]. Hazard analyses often refer to the venting of the insulating vacuum with atmospheric air as the worst-case failure scenario "under reasonably foreseeable conditions" [15] for liquid helium cryostats [14, 16]. However, the complete physical mechanisms in this highly dynamic failure scenario have not been fully analysed yet [16]. For instance, the process dynamics is often neglected in the established standards and design codes [17–22]. Instead, the sizing of cryogenic safety relief devices is based on few constant maximum heat flux data e.g. from [23–25], yielding potentially

[1]The normal boiling point of ^{3}He is $T_{\mathrm{nb}} = 3.191\,\mathrm{K}$ [3].

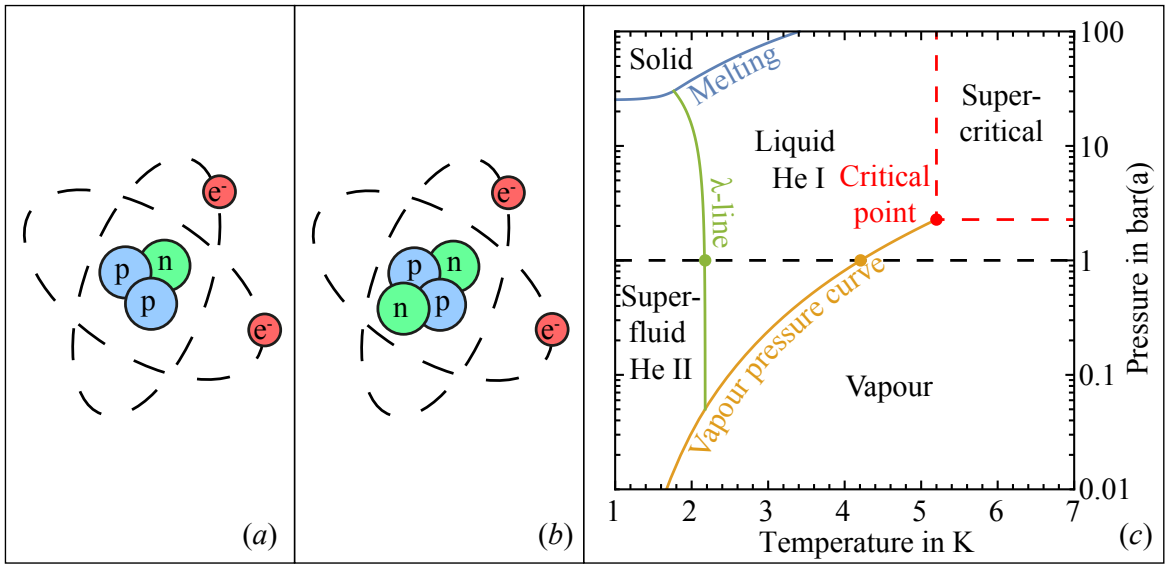

Figure 1.2: Scheme of the two stable helium isotopes (a) ^{3}He and (b) ^{4}He consisting of protons (p), neutrons (n) and electrons (e^-), and (c) the phase diagram of helium [13] with the normal fluid He I and the superfluid He II.

over-sized safety relief devices with implications on acquisition costs, space requirements and helium leakage [26, 27]. Besides this, over-sizing of safety relief valves often leads to unstable operation, the so-called pumping or chattering, where the safety relief valve opens and closes repeatedly within a very short time [27]. Chattering is known to reduce the discharge capacity and is likely to damage the safety relief valve [14,27]. Consequently, the sizing of cryogenic safety relief devices requires dynamic modelling of the evolution of the heat flux and pressure increase in cryostats following incidents [26, 27]. However, the heat transport cannot be described purely analytically because of gradients, non-equilibria and lacking data on solid air. Therefore, a dynamic model requires significant simplification that must be parametrized and validated by targeted experiments, which are challenging due to the high process dynamics and large gradients in the system.

An overview on the state of the art of cryogenic safety engineering is given in Chapter 2. Special focus is given to the established dimensioning of cryogenic safety relief devices and on an existing simplified dynamic model that describes the processes in liquid helium cryostats during the venting of the insulating vacuum. Chapter 3 presents the experimental setup, instrumentation, operation as well as the data processing and analysis of the cryogenic safety test facility PICARD, which stands for **P**ressure **I**ncrease in **C**ryostats and **A**nalysis of **R**elief **D**evices. PICARD has been designed, constructed and commissioned in the course of this work. The results of the first venting experiments conducted within the framework of an R&D collaboration between KIT and CERN are discussed in Chapter 4. The evolution and validation of a dynamic model based on first experimental data is explained in Chapter 5. An outlook on further projects is given in Chapter 6, before this work is summarized in Chapter 7.

Parts of Chapter 3 and 4 have previously been published in [26, 27].

CHAPTER 2

State of the art

2.1 Cryostat design

Other than vessels or containers for cryogenic liquid storage (so-called dewars), liquid helium cryostats involve active components such as sc. magnets and cavities, heaters, pumps and valves. Figure 2.1 shows a schematic drawing of a liquid helium cryostat that consists of a cryogenic vessel surrounded by a vacuum vessel. From a helium liquefier or storage, liquid helium is transferred through a filling line into the cryogenic vessel. During filling, operation and idle time, the evaporating cryogenic fluid is lead out of the cryostat through a return or exhaust line.

Different measures can be taken to reduce evaporation of the cryogenic fluid due to heat input caused by convection, conduction and radiation. The convection term is eliminated by insulating vacua at pressures below 0.1 Pa. The conduction through warm-cold connections is limited by the choice of materials, the conduction length and by heat-sinking [14]. Further, there are several methods to protect the cryogenic vessel from thermal radiation. First of all, the metal surfaces can be treated to reduce the emissivity ϵ from $\epsilon \approx 1.0$ for oxidized metals to $\epsilon \approx 0.1$ for mechanically and chemically polished metals [3, 28]. Especially efficient is electro-polishing and silver-plating. Since thermal radiation scales with the fourth power of absolute surface temperatures, it is very effective to add intermediate shields with reduced temperatures. One solution for dewars are conduction-cooled radiation shields e.g. made from electro-polished aluminium connected to the return line. In liquid helium cryostats, the radiation shield is often cooled with liquid nitrogen or with gaseous helium to keep the shield temperature at 77 K or below. This reduces the heat flux $\dot{q}$ to the liquid helium by two orders of magnitude to $\dot{q} \approx 50\,\mathrm{mW/m^2}$. Besides, the use of multilayer insulation (MLI) consisting of typically $10 \ldots 50$ layers of reflecting foil with spacers made of e.g. glass wool is often required in order to minimize thermal radiation in liquid helium cryostats [12]. For $\epsilon \ll 1$, the heat input is theoretically reduced by a factor of $(n+1)^{-1}$, where n is the number of layers [3]. To protect the cryogenic vessel and the vacuum vessel from

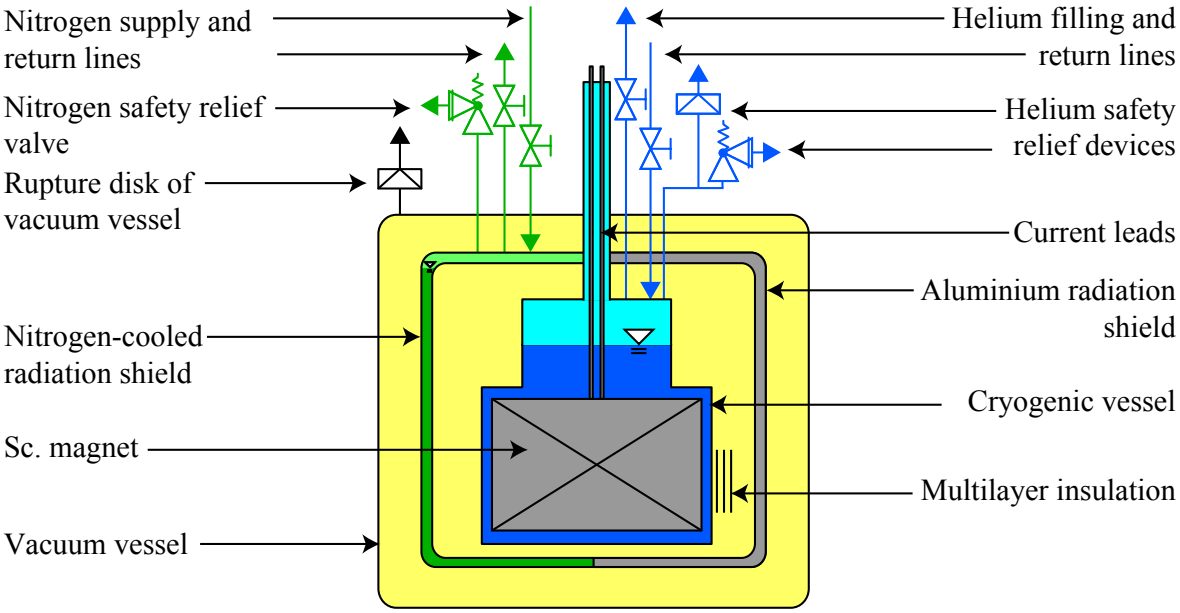

Figure 2.1: Schematic overview of a typical liquid helium cryostat for a sc. magnet [14].

overpressure during incidents and failure modes, safety relief devices such as rupture disks and safety relief valves must be provided [14].

2.2 Cryostat protection against overpressure

For the safe operation of liquid helium cryostats, a risk assessment must be conducted, including a *hazard and operability study* (HAZOP) to identify and evaluate possible risks to people and environment as well as a *failure mode effects and criticality analysis* (FMECA) to identify the probability of failure modes and the severity of their consequences [14]. Liquid helium cryostats usually contain pressure vessels, which are vessels with design pressures above $p > 0.5\,\mathrm{bar(g)}$, and are therefore subject to the European Pressure Equipment Directive (PED) [15].

2.2.1 Staged pressure protection

An exemplary approach for the pressure protection system consisting of several stages with regard to the maximum allowable working pressure p_S is shown in Figure 2.2 [14,15,29]. The first level is the operating level. During operation, the main parameters such as pressure, temperature and liquid level are controlled by the operating system or by the operator through e.g. the opening and closing of valves.

If the pressure increases above the acceptable default range, the measures of the monitoring level prevent further pressure increase, often based on programmable logic control (PLC). These measures may include alarms and automatic shut-down. If PLC measures also fail, shut-down may be enforced by hard-wired pressure switches.

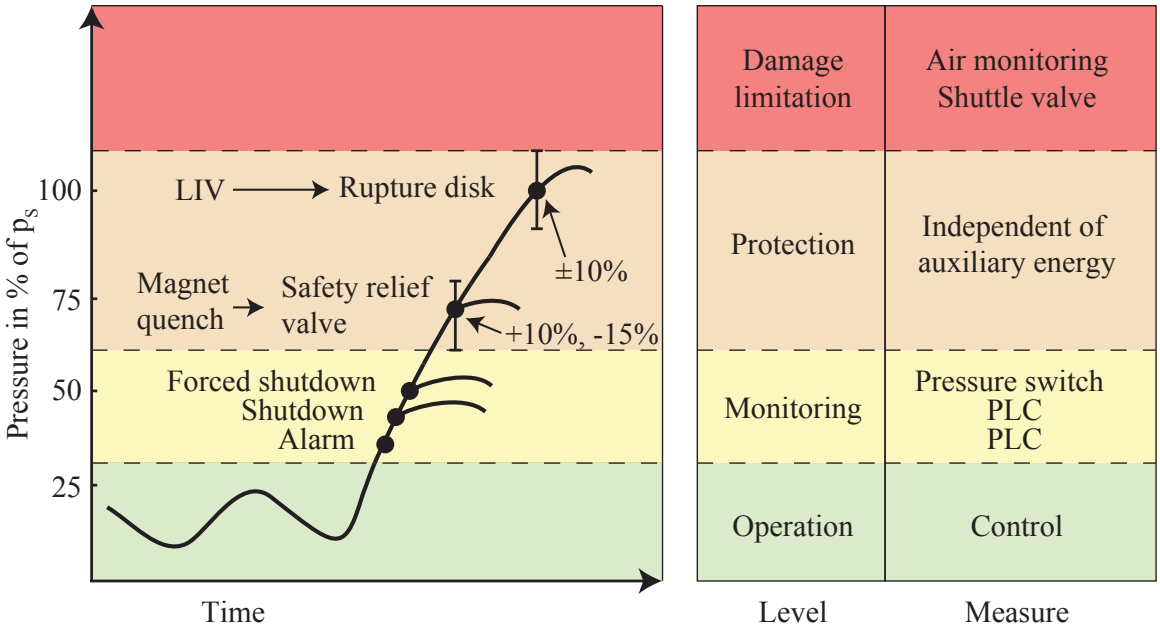

Figure 2.2: Typical pressure protection levels for the safety design of liquid helium cryostats able to cope with incidents such as the loss of insulating vacuum (LIV) [14, 29].

In the subsequent protection level, the vessel has to be protected from overpressure independently of auxiliary energy. For redundancy and diversity of the safety relief system, the measures in the protection level preferably include both a safety relief valve and a rupture disk as the ultimate level of protection. For damage limitation, helium recovery lines, shuttle valves and air monitoring systems are used. As the impact of fire is not foreseen in the typical HAZOP study for liquid helium cryostats, the absence of flammable objects in the cryostat's surroundings is necessary [14].

According to the PED [15], the pressure inside a pressure vessel may exceed p_S for short times by maximum 10 %. The pressure levels in a staged pressure relief system must therefore be carefully designed in order to take tolerances and time constants into account. The pressure vessel itself must be designed to withstand the hydrostatic test pressure of $1.43 \cdot p_S$ or other tests of equivalent validity [15]. As illustrated in Figure 2.2, the bursting pressure of the rupture disk is typically equal to p_S, considering the rupture disk's bursting pressure tolerance of ±10 %. A typical safety margin between the bursting pressure of the rupture disk and the relieving pressure of the safety relief valve is 30 % of p_S, considering the maximum opening pressure difference of 10 % of the safety relief valve [14, 17, 29]. The relieving pressure p_0 is the pressure when a safety relief valve is fully open under the actual operating conditions and is used for the sizing [17]. Safety relief valves are usually adjusted by valve manufacturers to the set pressure p_{set}, where the valve commences to open. Full opening must be achieved at $p_0 \leq 1.1 \cdot p_{set}$ according to DIN EN ISO 4126 [17].

In order to accommodate alarms in the monitoring level, the operating pressure

may be as low as 30 % of p_S. Consequently, p_S should be chosen sufficiently high in order to benefit from a staged protection system [14, 29]. However, it is not always possible to implement all these safety levels due to other design constraints.

2.2.2 Reasons for pressure increase in cryostats

In the course of this thesis, significant contributions to a German standardisation project on the safety of liquid helium cryostats were given, leading to DIN SPEC 4683 [14]. It lists numerous causes for the pressure increase in cryostats, including:

- blocking of exhaust or return lines
- operating errors
  - overfilling
  - faulty switching of valves and pumps
- thermoacoustic oscillations
- loss of insulating vacuum
  - leaking of liquid helium from the cryogenic vessel to the vacuum space
  - leaking of liquid nitrogen from a nitrogen-cooled radiation shield to the vacuum space
  - leaking of atmospheric air through a hole in the vacuum vessel
- quench of a sc. magnet

The quench of a sc. magnet is one of the most common failure modes in liquid helium cryostats, signifying the transition from the superconducting state with zero resistivity to the normal conducting state. Superconductivity exists below the critical surface established by the critical temperature, the critical current density and the critical magnetic field as shown in Figure 2.3. Quenches due to local values above the critical surface essentially turn a sc. magnet into a heater. The processes following such an event are schematically shown in Figure 2.4 (*a*) to (*d*). Because of the resistivity in the normal conducting state, heat is produced locally by Joule heating from an electric current as illustrated in Figure 2.4 (*a*), yielding either the automatic or enforced quench of the complete magnet as shown in Figure 2.4 (*b*). The energy stored in the magnet is released in form of heat and transferred to the coolant, increasing both its pressure and temperature (Figure 2.4 (*c*)). Once the relieving pressure is reached, helium is released through an opening safety relief device, for example a safety relief valve (Figure 2.4 (*d*)).

The maximum credible accident (MCA) in liquid helium cryostats is often the venting of the insulating vacuum with atmospheric air with subsequent magnet quench as shown in Figure 2.4 (*e*) to (*h*). Through an opening in the vacuum vessel, atmospheric air vents into the vacuum space of the cryostat (Figure 2.4 (*e*)). The air freezes out or condenses on the cryogenic vessel and the resulting heat flux is transferred to the liquid

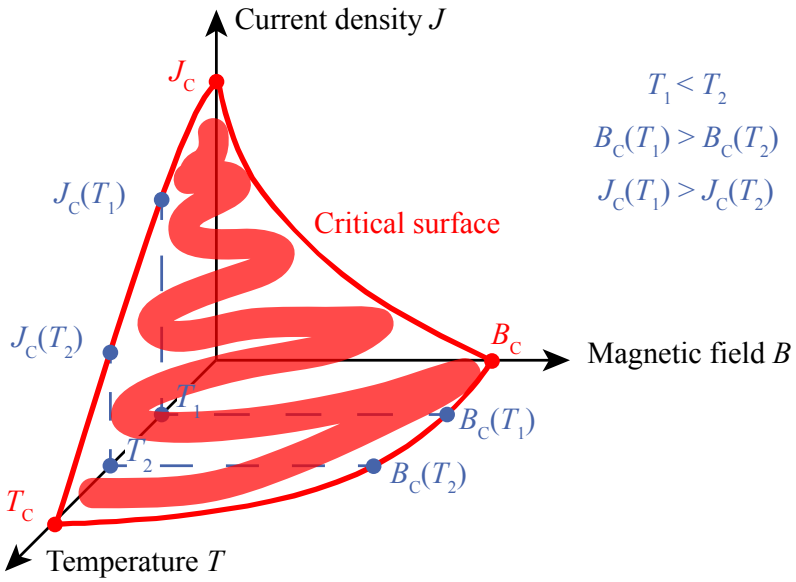

Figure 2.3: Above its critical surface that is limited by the critical temperature T_C, the critical current density J_C, and the critical magnetic field B_C, a sc. material becomes a normal conductor. Within the sc. region, higher magnetic fields and current densities can be applied without loosing the sc. properties the lower the temperatures are [30].

helium inside the cryogenic vessel (Figure 2.4 (f)). Again, the helium temperature and pressure rise, triggering the subsequent magnet quench that further increases the heat input to the helium (Figure 2.4 (g)). Same as for the failure mode of a pure sc. magnet quench, the helium has to be released from the system. During the MCA, helium is discharged through both the rupture disk and the safety relief valve, as presented in Figure 2.4 (h). More information and recommendations for the pressure protection system of liquid helium cryostats are given in DIN SPEC 4683 [14].

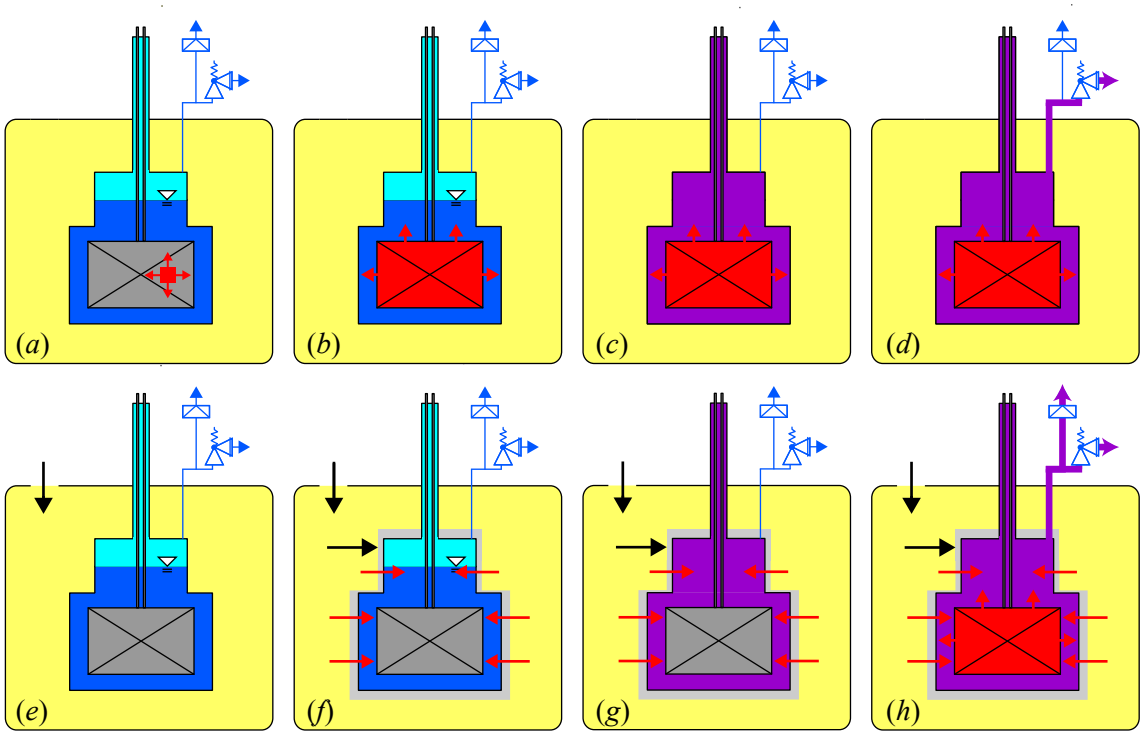

Figure 2.4: Schematic overview of the processes during (a)-(d) a magnet quench and (e)-(h) venting of the insulating vacuum with atmospheric air and a subsequent magnet quench. Heating is indicated in red, the supercritical state of the cryogenic fluid as consequence of the pressure and temperature increase is highlighted in purple. The layer of desublimating or condensing venting fluid is indicated in light grey.

2.3 General dimensioning of cryogenic safety relief devices

The required discharge area A_0 of safety relief devices is calculated following the applicable standards [17–19, 22] assuming an ideal nozzle and adiabatic expansion as

$$A_0 = \frac{\dot{m}_{\mathrm{Out}}}{\Psi \cdot K_{\mathrm{dr}} \cdot \sqrt{2 \cdot \frac{p_0}{v_0}}} \tag{2.1}$$

with the discharge mass flow rate $\dot{m}_{\mathrm{Out}}$, the discharge function Ψ, the certified discharge coefficient K_{dr}, the relieving pressure p_0 and the specific volume v_0. The notation for this section is illustrated in Figure 2.5.

The relieving pressure p_0 is determined by the safety concept as explained in Section 2.2. The specific volume follows from the relieving pressure and the worst-case discharge temperature T_0, which is determined in the course of the calculation of the discharge mass flow rate explained below. With the back pressure p_{b} and the relieving

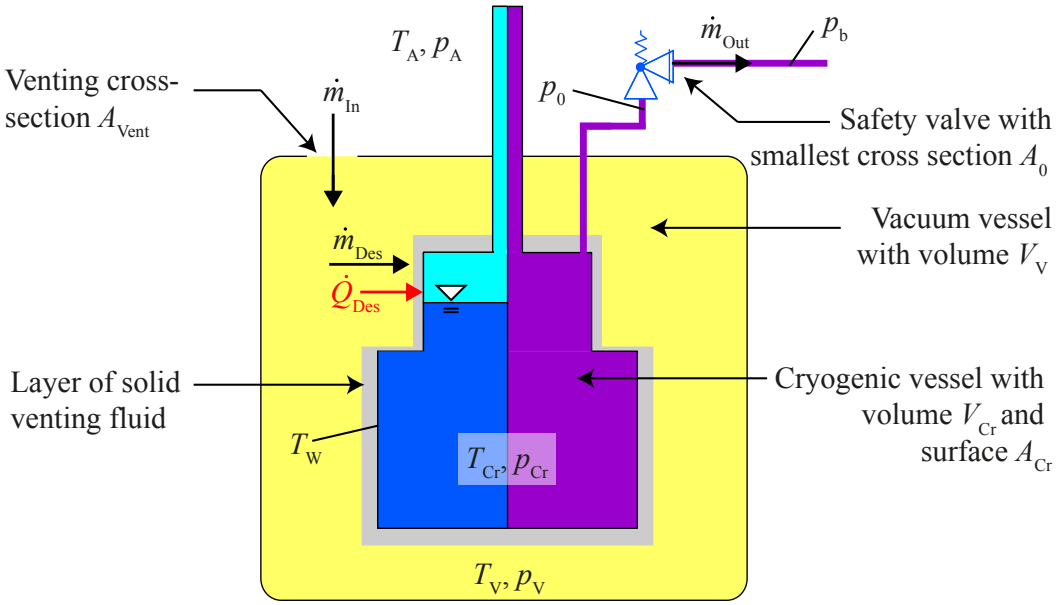

Figure 2.5: Illustrated nomenclature for the dimensioning of cryogenic safety relief devices.

pressure p_0, Ψ is a function of the isentropic exponent κ and is defined for gaseous and supercritical inlet conditions for subcritical flow

$$\frac{p_b}{p_0} > \left(\frac{2}{\kappa+1}\right)^{\frac{\kappa}{\kappa-1}} \tag{2.2}$$

and for critical flow

$$\frac{p_b}{p_0} \leq \left(\frac{2}{\kappa+1}\right)^{\frac{\kappa}{\kappa-1}} \tag{2.3}$$

as

$$\Psi = \begin{cases} \sqrt{\frac{\kappa}{\kappa-1}\left[\left(\frac{p_b}{p_0}\right)^{\frac{2}{\kappa}} - \left(\frac{p_b}{p_0}\right)^{\frac{\kappa+1}{\kappa}}\right]} & \text{, subcritical flow} \\ \sqrt{\frac{\kappa}{\kappa+1}}\left(\frac{2}{\kappa+1}\right)^{\frac{1}{\kappa-1}} & \text{, critical flow .} \end{cases} \tag{2.4}$$

For single-phase liquid inlet $\Psi = 1$ is used. The discharge function for two-phase inlet conditions can be calculated as explained in [22, 31]. The certified discharge coefficient is defined as

$$K_{dr} = 0.9\,\frac{\dot{m}_{Out,measured}}{\dot{m}_{Out,ideal\ orifice}}\,. \tag{2.5}$$

K_{dr} is determined by the manufacturer of the safety relief device. Values are typically in the range of $K_{dr} \approx 0.7$ for gaseous discharge conditions [18, 19]. Depending on the code, K_{dr} is sometimes referred to as α_w [18, 19].

The most common method for calculating the discharge mass flow rate for cryogenic applications is given in ISO 21013-3 [21]. In this static model, two different pressure ranges are distinguished: $p_0 < p_{Crit}$ and $p_0 \geq p_{Crit}$, where p_{Crit} is the fluid's critical

pressure. In the first case, the discharge mass flow rate is calculated for low relieving pressures as

$$\dot{m}_{\mathrm{Out}} = \frac{v_{\mathrm{v}} - v_{\mathrm{l}}}{v_{\mathrm{v}}} \cdot \frac{\dot{Q}}{\Delta h_{\mathrm{v}}} \,, \tag{2.6}$$

with the specific volume of saturated vapour v_{v} and liquid v_{l} at p_0, respectively, with the heat input to the system $\dot{Q}$ and the latent heat of evaporation Δh_{v}. In this case, the specific vapour volume $v_0 = f(p_0, T_{\mathrm{Sat}})$ at the saturation temperature T_{Sat} is used in Eq. (2.1).

The second pressure range is the most common case for liquid helium applications since the relieving pressure of safety relief devices is usually above $p_{\mathrm{Crit,He}} = 2.27\,\mathrm{bar(a)}$. Thus, $\dot{m}_{\mathrm{Out}}$ is calculated from

$$\dot{m}_{\mathrm{Out}} = \frac{\dot{Q}}{L'} \,, \tag{2.7}$$

with the specific heat input L' defined as

$$L' = v \cdot \left(\frac{\delta h}{\delta v} \right)_{p_0} \tag{2.8}$$

at the worst-case conditions where the parameter θ reaches its maximum. θ is defined as

$$\theta = \frac{\sqrt{v}}{v \cdot \left(\frac{\delta h}{\delta v} \right)_{p_0}} \,. \tag{2.9}$$

The derivation of Eq. (2.9) is explained in [20]. The maximum of θ is found by variation of the temperature and hence calculating the specific volume $v = f(p_0, T)$ of the critical or supercritical fluid and the enthalpy $h = f(p_0, T)$ of the fluid at the same conditions. This worst-case temperature T_0 is hence also used for calculating $v_0 = f(p_0, T_0)$ to be inserted in Eq. (2.1).

The heat load $\dot{Q}$ that is transferred into the cryogenic vessel during the venting of the insulating vacuum is calculated from a constant heat flux $\dot{q}$ and the surface of the cryogenic vessel A_{Cr} as

$$\dot{Q} = \dot{q} \cdot A_{\mathrm{Cr}} \,. \tag{2.10}$$

Data on the maximum occurring heat flux during this scenario can be found in literature as listed in Table 2.1. Heat flux data for other cryogenic fluids can be found for instance in [32–35]. The heat fluxes listed in Table 2.1 are calculated from measurement data of experiments conducted with very different test setups. For instance, Dhuley and Van Sciver [38, 39] vent nitrogen into a vacuum tube cooled at the outside with 7.7 L liquid helium [40]. While the heat flux caused by deposition of nitrogen is estimated to up to $6\,\mathrm{W/cm^2}$ from measurement data in [39], this value is further increased to up to $40\,\mathrm{W/cm^2}$ in [38]. However, it is stated that the heat flux transferred to the helium is with up to $3\,\mathrm{W/cm^2}$ considerably lower because the heat transfer is limited by film boiling [38, 39]. The difference is assumed to accumulate in the tube material and to be conducted axially along the tube wall [38, 39]. Ercolani et al. [37] and Harrison [25] use very small helium vessels with a volume of $10 \ldots 12\,\mathrm{L}$, and Lehmann and Zahn [23]

Table 2.1: Literature values for the heat input caused by loss of insulating vacuum in a liquid helium (LHe) cryostat.

Reference	Heat input without additional insulation in W/cm^2	Heat input with additional insulation in W/cm^2
Bartenev et al. [36]	-	$0.95 \dots 1.93$ (50 layers of MLI) $0.3 \dots 0.63$ (N_2 shield)
Harrison [25]	3.1	0.44 (composite insulation)
Lehmann and Zahn [23]	3.8	0.6 (10 layers of MLI)
Cavallari et al. [24]	4.0	-
Ercolani et al. [37]	4.5	-
Dhuley and Van Sciver [38,39]	$6.0 \dots 40.0$ (deposition) 3.0 (transferred to LHe)	-

release helium at ambient pressure, while Cavallari et al. [24] measure the heat fluxes in the prototypes of the cryostat for the CERN sc. cavities with very specific geometry. The different methods for calculating the heat flux used in [23–25, 37–39] can be found in Appendix A.1.

2.4 Dynamic model for cryogenic safety relief devices

For the design of the helium safety relief system of a cryostat for the Karlsruhe Tritium Neutrino Experiment (KATRIN), Chorowski et al. [41, 42] consider the process dynamics inside the cryogenic vessel. The changes of state are calculated applying the first law of thermodynamics

$$\frac{\mathrm{d}(m_{\mathrm{He}} \cdot u_{\mathrm{He}})}{\mathrm{d}\tau} = \dot{Q}_{\mathrm{tot}} + \dot{m}_{\mathrm{Out,He}} \cdot h_{\mathrm{He}} \tag{2.11}$$

with the helium mass m_{He}, the internal helium energy u_{He}, the time τ, the total heat load to the helium (including optionally the additional heat input by a quenching sc. magnet) $\dot{Q}_{\mathrm{tot}}$, the discharge mass flow rate $\dot{m}_{\mathrm{Out,He}}$ and the helium enthalpy h_{He}. Constant maximum heat flux data based on literature values [23, 25] are used for the calculation. The calculated discharge mass flow rate is hence used for the determination of the minimal required area of the safety relief valve based on Eq. (2.1).

The dynamic model was further developed in [14, 16, 43, 44] as shown in the block diagram in Figure 2.6. This model considers the process dynamics in the vacuum space as well as in the cryogenic fluid as highlighted in the yellow and light blue boxes in Figure 2.6, respectively. The pressure increase in the vacuum vessel due to the air

influx is based on the *ideal gas law* differentiated with respect to the time τ

$$\frac{\mathrm{d}p_\mathrm{V}(\tau)}{\mathrm{d}\tau} = \frac{[\dot{m}_\mathrm{In}(\tau) - \dot{m}_\mathrm{Des}(\tau)] \cdot R_\mathrm{V} \cdot T_\mathrm{V}}{V_\mathrm{V} - V_\mathrm{Cr}} \tag{2.12}$$

with the vacuum pressure p_V, the specific gas constant of the venting fluid R_V, the ambient temperature $T_\mathrm{V} = T_\mathrm{A} = 300\,\mathrm{K}$ and the notation according to Figure 2.5.

At constant ambient pressure p_A and density ρ_A, the mass flow rate $\dot{m}_\mathrm{In}$ venting into the vacuum space is a function of the vacuum pressure p_V and the isentropic exponent of the venting fluid κ_V. It is defined for critical flow and subsonic flow (with $p_\mathrm{b} = p_\mathrm{V}$ and $p_0 = p_\mathrm{A}$ with respect to Eq. (2.2) and Eq. (2.3)) as

$$\dot{m}_\mathrm{In}(p_\mathrm{V}) = A_\mathrm{Vent} \cdot \sqrt{2 \cdot p_\mathrm{A} \cdot \rho_\mathrm{A}} \begin{cases} \sqrt{\frac{\kappa_\mathrm{V}}{\kappa_\mathrm{V}-1} \cdot \left[\left(\frac{p_\mathrm{V}}{p_\mathrm{A}}\right)^{\frac{2}{\kappa_\mathrm{V}}} - \left(\frac{p_\mathrm{V}}{p_\mathrm{A}}\right)^{\frac{\kappa_\mathrm{V}+1}{\kappa_\mathrm{V}}} \right]} & \text{, subcritical flow} \\ \left(\frac{2}{\kappa_\mathrm{V}+1}\right)^{\frac{1}{\kappa_\mathrm{V}-1}} \cdot \sqrt{\frac{\kappa_\mathrm{V}}{\kappa_\mathrm{V}+1}} & \text{, critical flow}\,. \end{cases} \tag{2.13}$$

The desublimation mass flow rate $\dot{m}_\mathrm{Des}$ is modelled as a function of the mass transfer coefficient k_Des and the difference between the gaseous air density ρ_V and the saturation density $\rho_\mathrm{Sat,W}$ on the cold surface

$$\dot{m}_\mathrm{Des}(p_\mathrm{V}, T_\mathrm{W}) = A_\mathrm{Cr} \cdot k_\mathrm{Des} \cdot \left[\frac{p_\mathrm{V}}{R_\mathrm{V}\ T_\mathrm{V}} - \rho_\mathrm{Sat,W}(T_\mathrm{W}) \right]. \tag{2.14}$$

As a first approximation, $k_\mathrm{Des} = 0.75\,\mathrm{m/s}$ is assumed based on literature data on the desublimation of snow [45]. The condensation of the venting fluid occurring at wall temperatures T_W above the triple point is not considered.

Because of a typical frost layer thickness in the millimetre range [24], the cold surface A_Cr is regarded as constant. The resulting desublimation heat load $\dot{Q}_\mathrm{Des}$ is modelled as a function of the specific enthalpy difference between the gaseous and the solid air as

$$\dot{Q}_\mathrm{Des}(p_\mathrm{V}, T_\mathrm{W}) = \dot{m}_\mathrm{Des}(p_\mathrm{V}, T_\mathrm{W}) \cdot [h_\mathrm{V}(p_\mathrm{V}) - h_\mathrm{W}(T_\mathrm{W})] \tag{2.15}$$

using thermodynamic property data of solid nitrogen from [11].

The changes of state inside the cryogenic vessel are hence calculated from the first law of thermodynamics. For the closed cryogenic vessel, the initial total mass $m_\mathrm{Cr,0}$ and thus the average density of the cryogenic fluid remain constant (isochoric process), yielding

$$\frac{\mathrm{d}u_\mathrm{Cr}}{\mathrm{d}\tau} = \frac{\dot{Q}_\mathrm{Cr}}{m_\mathrm{Cr,0}}\,. \tag{2.16}$$

The discharge of the cryogenic fluid starting from the moment the pressure reaches p_0 is also modelled with an ideal safety relief valve operating at $p_0 = \text{constant}$. Contrary to the model presented in [41, 42], both the enthalpy and the kinetic energy of the discharge mass flow rate are considered as

$$\frac{\mathrm{d}u_\mathrm{Cr}}{\mathrm{d}\tau}\ m_\mathrm{Cr} = \dot{Q}_\mathrm{Cr} - \dot{m}_\mathrm{Out} \cdot \left(h_\mathrm{Cr} - u_\mathrm{Cr} + \frac{1}{2}\ w_\mathrm{Out}^2\right). \tag{2.17}$$

The flow velocity w_{Out} is calculated by applying the continuity equation for critical and subcritical flow as

$$w_{\mathrm{Out}}(u_{\mathrm{Cr}}) = \sqrt{2 \cdot p_0 \cdot v_{\mathrm{Cr}}(u_{\mathrm{Cr}})} \cdot \begin{cases} \sqrt{\frac{\kappa_{\mathrm{Cr}}}{\kappa_{\mathrm{Cr}}-1} \cdot \left[1 - \left(\frac{p_{\mathrm{b}}}{p_0}\right)^{\frac{\kappa_{\mathrm{Cr}}-1}{\kappa_{\mathrm{Cr}}}}\right]} & \text{, subcritical flow} \\ \sqrt{\frac{\kappa_{\mathrm{Cr}}}{\kappa_{\mathrm{Cr}}+1}} & \text{, critical flow .} \end{cases} \tag{2.18}$$

The equations for describing the states in the vacuum space and inside the cryogenic vessel are interconnected by the heat transfer through the cryogenic vessel wall as indicated in the purple box in the block diagram displayed in Figure 2.6. As a simplification, the thermal resistance between the vacuum space and the helium inside the cryogenic vessel is neglected, yielding $T_{\mathrm{Cr}} = T_{\mathrm{W}}$. This influences the heat load values, resulting in $\dot{Q}_{\mathrm{Des}} = \dot{Q}_{\mathrm{Cr}}$, which directly links Eq. (2.15) with Eq. (2.16) and Eq. (2.17). The system of differential equations must therefore be solved simultaneously, using e.g. a numerical solver in *Mathematica* [46]. Initial conditions $p_{\mathrm{V}}(0)$ and $u_{\mathrm{Cr}}(0)$ for the isochoric heat input are obtained from the operating parameters. The states at τ_{S} when the safety relief device opens serve as initial conditions for the subsequent isobaric process as shown in Figure 2.6. The solution of the differential equation system yields time-dependent results for all relevant process parameters such as pressures, temperatures, heat load and flow rates. With these, a time-dependent required discharge diameter based on for instance AD-2000 [19] can be calculated as

$$A_0(\tau) = \frac{\dot{m}_{\mathrm{Out}}(\tau)}{\Psi(\tau) \cdot K_{\mathrm{dr}} \cdot \sqrt{2 \cdot \frac{p_0}{v(\tau)}}} \tag{2.19}$$

with

$$\Psi(\tau) = \begin{cases} \sqrt{\frac{\kappa_{\mathrm{Cr}}[T_{\mathrm{Cr}}(\tau)]}{\kappa_{\mathrm{Cr}}[T_{\mathrm{Cr}}(\tau)]-1} \left[\left(\frac{p_{\mathrm{b}}}{p_0}\right)^{\frac{2}{\kappa_{\mathrm{Cr}}[T_{\mathrm{Cr}}(\tau)]}} - \left(\frac{p_{\mathrm{b}}}{p_0}\right)^{\frac{\kappa_{\mathrm{Cr}}[T_{\mathrm{Cr}}(\tau)]+1}{\kappa_{\mathrm{Cr}}[T_{\mathrm{Cr}}(\tau)]}}\right]} & \text{, subcritical flow} \\ \sqrt{\frac{\kappa_{\mathrm{Cr}}[T_{\mathrm{Cr}}(\tau)]}{\kappa_{\mathrm{Cr}}[T_{\mathrm{Cr}}(\tau)]+1}} \left(\frac{2}{\kappa_{\mathrm{Cr}}[T_{\mathrm{Cr}}(\tau)]+1}\right)^{\frac{1}{\kappa_{\mathrm{Cr}}[T_{\mathrm{Cr}}(\tau)]-1}} & \text{, critical flow .} \end{cases} \tag{2.20}$$

This method enables the consideration of a time-dependent isentropic exponent of the cryogenic fluid $\kappa_{\mathrm{Cr}}(\tau)$, which is highly temperature dependent at $T < 15\,\mathrm{K}$ [14]. The real-gas isentropic exponent must be used in Eq. (2.20) because it strongly deviates from the quotient of the isobaric and isochoric specific heat capacities c_p/c_v for helium at low temperatures.

The dynamic model contains simplifying assumptions concerning the kinetics of desublimation and heat transfer into the cryogenic vessel. Therefore, experimental data are essential to validate the model and to determine scaling parameters for absolute values. An experimental facility has therefore been developed, designed, constructed and commissioned, which is described in the next chapter.

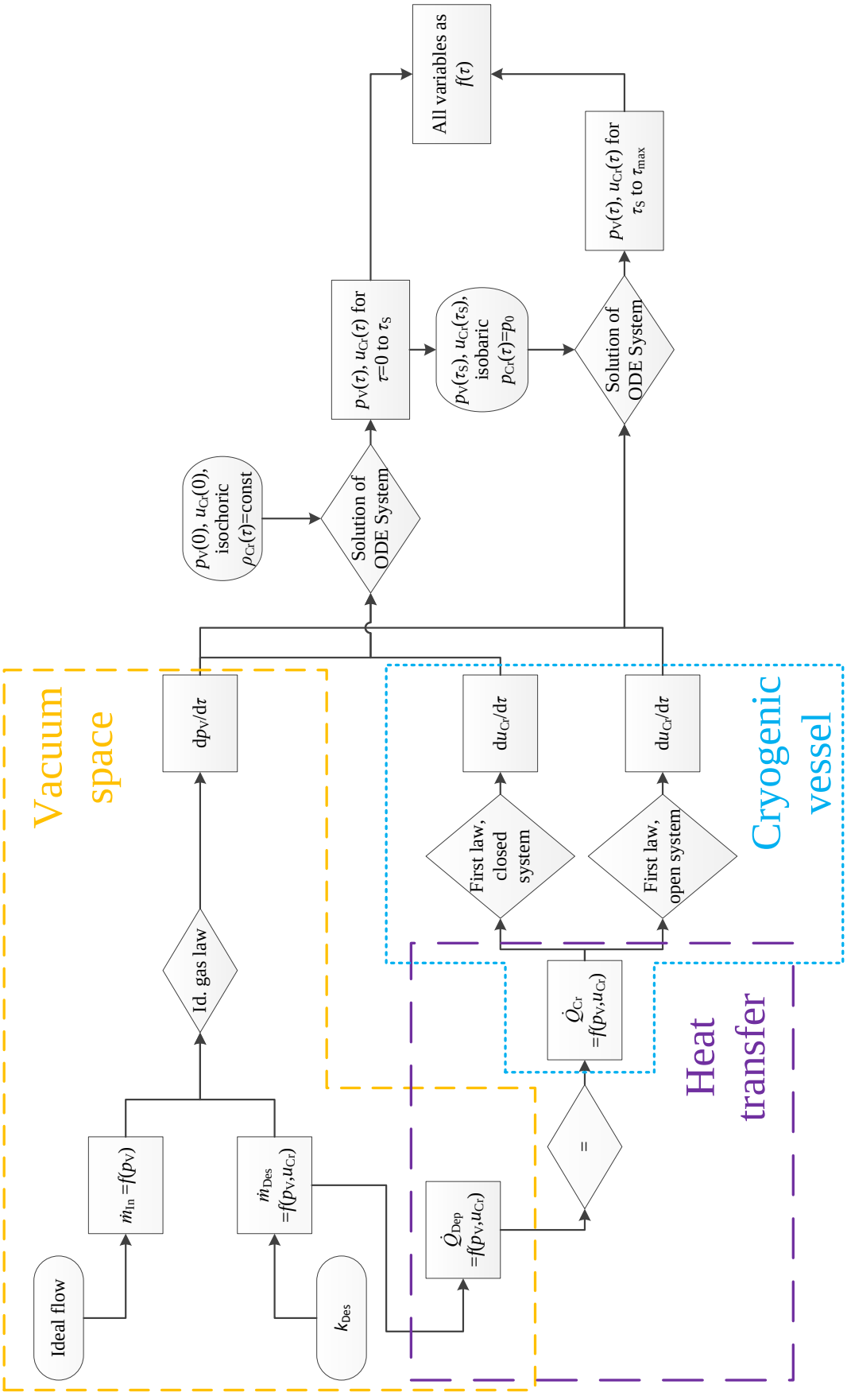

Figure 2.6: Block diagram of the dynamic model developed in [16, 43, 44].

CHAPTER 3

The safety test facility PICARD

3.1 Experimental setup

The cryogenic test facility PICARD, which stands for **P**ressure **I**ncrease in **C**ryostats and **A**nalysis of **R**elief **D**evices, has been designed and constructed at the Institute of Technical Physics at the Karlsruhe Institute of Technology in the course of this work. An overview of PICARD, consisting of a cryostat with a vacuum pumping station, piping, safety relief devices, a dewar for supplying the cryogenic fluid, an assembly jig for mounting of e.g. MLI and a water bath for warming the evaporating cryogen is given in Figure 3.1. Because of the low operating temperatures, the materials for all components are selected according to [47]. A picture of the cryogenic vessel mounted on the assembly jig is shown in Figure 3.2(a). The cryogenic vessel has a volume of 107 L, the liquid level should, however, be limited to 80 % in order to avoid overfilling. In comparison, existing experimental test facilities have a typical cryogenic liquid volume of about 7.7 ... 12 L [25, 37, 40]. The pressurized volume is protected with a rupture disk at $p_S = 16\,\mathrm{bar(g)}$.

A vacuum pumping station of type *HiCube 80 Classic* by *Pfeiffer Vacuum* is flanged to the vacuum vessel and provides an insulating vacuum of about $p_V = 10^{-6}\,\mathrm{mbar}$. Besides this, the surfaces of the cryogenic vessel have been electro-polished. An additional radiation shield made of aluminium is cooled by thermal conduction through contact with the vent line as can be seen in Figure 3.2(a). The top and bottom of the radiation shield have holes of 60 mm diameter to enable the warm venting fluid to reach the cold surface. In order to minimize heat input to the cold cryogenic vessel by radiation, the holes are covered with baffles. Additionally, MLI can be applied at the assembly jig. An additional buffer vessel with the same geometry as the PICARD vacuum vessel can be flanged to the venting orifice as shown in Figure 3.2(b) [27]. The main dimensions and materials of the PICARD cryogenic vessel, vacuum vessel, buffer vessel, as well as of the piping and of the radiation shield are given in Table 3.1 [26, 27].

The cryogenic safety experiments presented in this work focus on the parameters

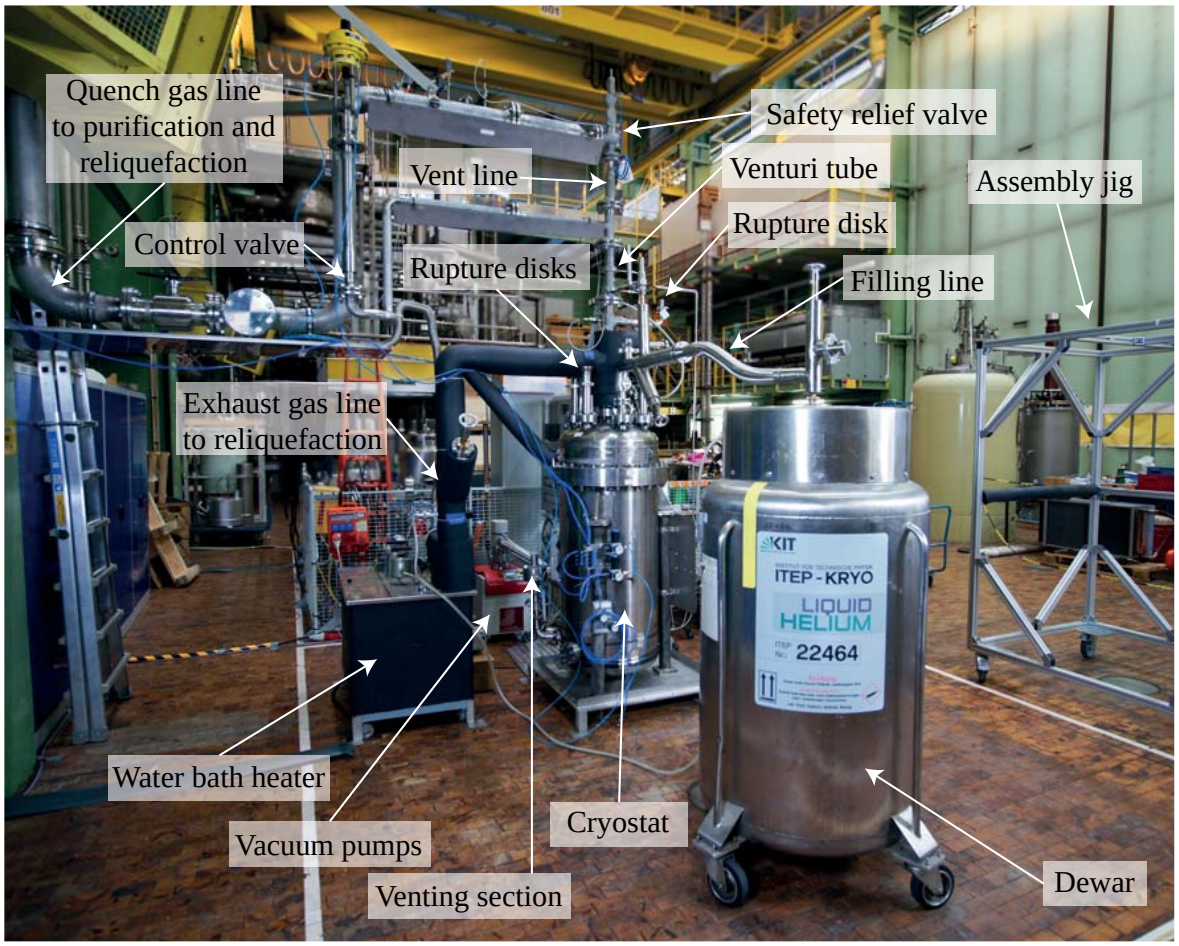

Figure 3.1: Overview of the PICARD test facility.

influencing the heat flux and hence the process dynamics during the venting of the insulating vacuum. The various conditions for flow rate and heat flux measurements at PICARD are given in Table 3.2. Presently, safety relief valves of type 4414.4644 by *Leser* set to pressures in the range of $1.3 \ldots 7.7\,\mathrm{bar(g)}$ are used as safety relief device [26]. A control valve by *Kämmer* that bypasses the safety relief valve is installed for future experiments. The maximum working pressure of $12\,\mathrm{bar(g)}$ is based on the maximum allowable working pressure of the cryostat $p_\mathrm{S} = 16\,\mathrm{bar(g)}$ minus the tolerances of the rupture disk and the safety relief valve [26, 48]. With its high maximum allowable working pressure and large cryogenic volume, the cryogenic test facility PICARD allows a broad range of experiments and more detailed studies of the processes following incidents in cryostats compared to existing test setups.

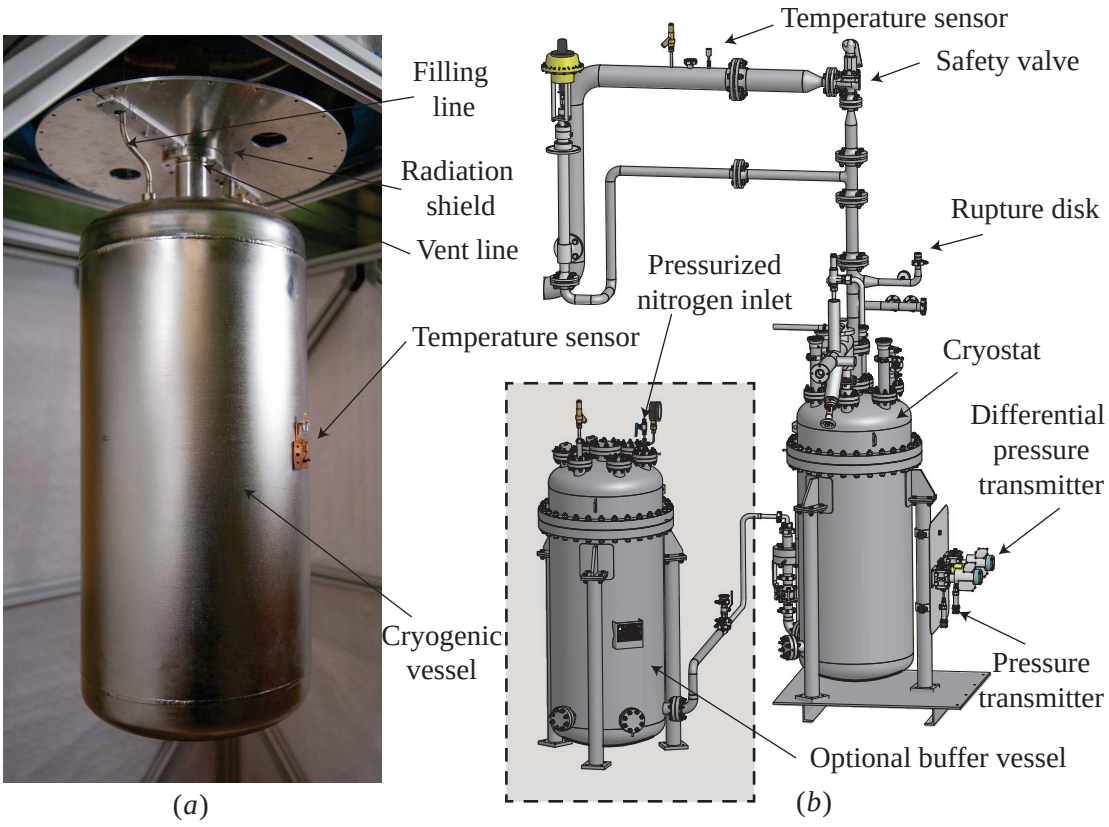

Figure 3.2: (a) Picture of the PICARD cryogenic vessel mounted on the assembly jig and connected to the radiation shield [26], and (b) simplified CAD-drawing of the PICARD test facility with the additional buffer vessel flanged to the venting section [27].

Table 3.1: Dimensions and materials of the main PICARD components [26].

Component	Parameter	Value
Cryogenic vessel	Height	900 mm
	Outer diameter	400 mm
	Wall thickness	5 mm
	Volume	107 L
	Maximum allowable working pressure	16 bar(g)
	Material	Stainless steel 1.4571
Vacuum vessel	Height	1500 mm
	Outer diameter	600 mm
	Wall thickness	4 . . . 5 mm
	Volume	400 L
	Maximum allowable working pressure	10 bar(g)
	Material	Stainless steel 1.4301 and 1.6903
Buffer vessel	Height	1500 mm
	Outer diameter	600 mm
	Wall thickness	4 . . . 5 mm
	Buffer volume	400 L
	Maximum allowable working pressure	10 bar(g)
	Material	Stainless steel 1.4301 and 1.6903
Radiation shield	Height	1050 mm
	Outer Diameter	500 mm
	Wall thickness	3 mm
	Material	$AlMg_3$
Vent line	Inner diameter	60 mm
Quench gas line	Inner diameter	100 . . . 150 mm

Table 3.2: Parameters influencing the heat flux and process dynamics during hazardous incidents in cryostats and their variation possibilities at PICARD [26].

Parameter	Range at PICARD
Venting diameter	Up to 40 mm
Insulation	Up to 30 layers of MLI with/without radiation shield
Liquid level	Up to 80 %
Set pressure of safety relief valve	Up to 12 bar(g)
Cryogenic fluid	E.g. helium, nitrogen
Venting fluid	E.g. air, nitrogen
Safety relief device	Safety relief valve, rupture disk, control valve
Discharge mass flow rate	Single-phase, two-phase up to about 4 kg/s in case of helium

3.2 Instrumentation

The Piping and Instrumentation Diagram (P&ID) with the temperature sensors (TI), pressure transducers (PI), differential pressure transducers (PDI), liquid level probes (LI) and humidity probe (MI) is shown in Figure 3.3. The instrument symbols in circles indicate a display on site, those in combs specify that the quantities are recorded by the data acquisition system. Data sheets of selected sensors and apparatus can be found in Appendix C.

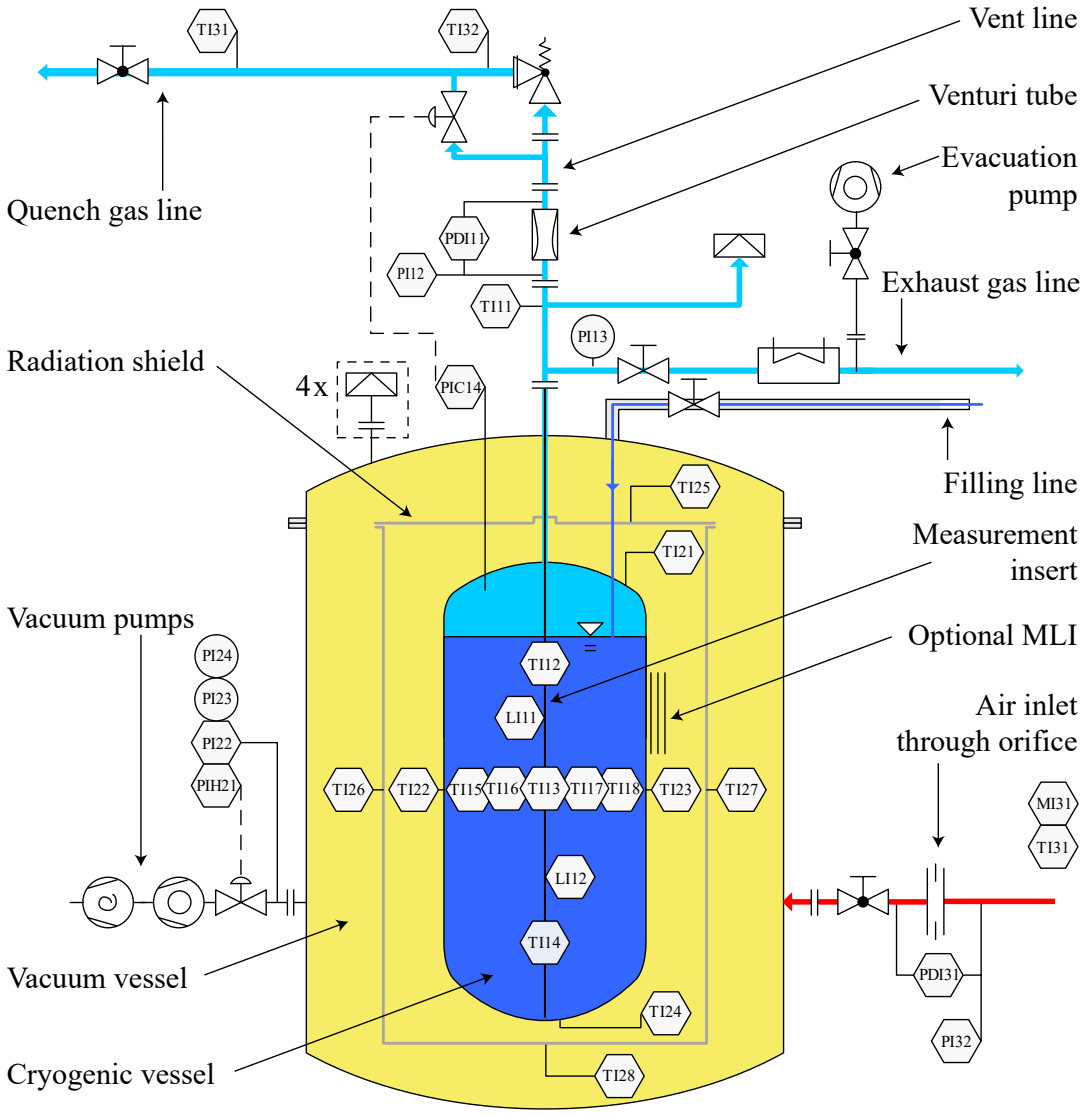

Figure 3.3: P&ID of the PICARD experiment [26, 27].

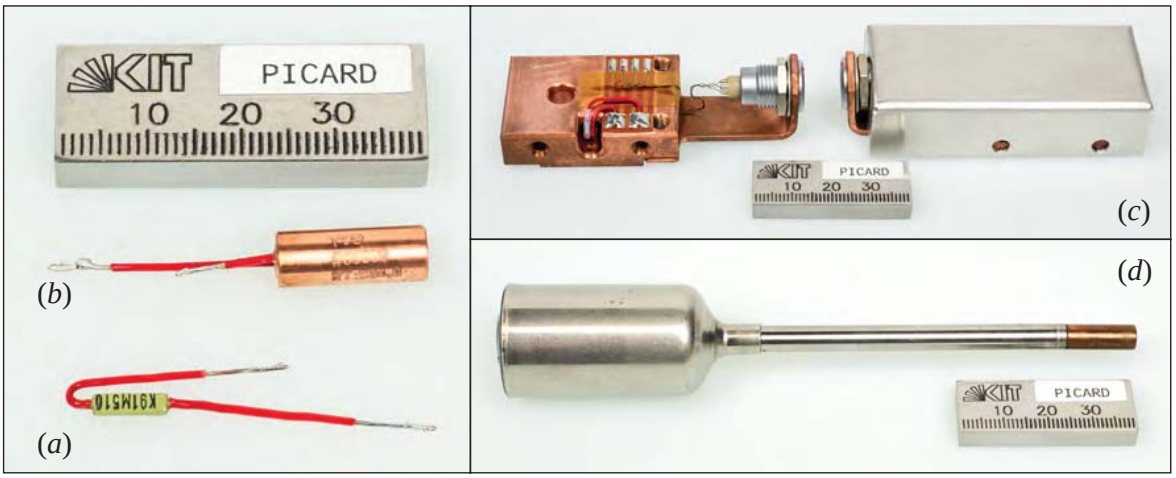

Figure 3.4: Pictures of TVO temperature sensors installed in PICARD: (*a*) plain TVO, (*b*) TVO cast in a copper cartridge, (*c*) cast TVO inserted into a copper block with aluminium radiation shield for surface temperature measurement, and (*d*) cast TVO at the tip of a thermally insulated stick for in-tube temperature measurement [26].

3.2.1 Pressure measurement

The pressure inside the PICARD cryogenic vessel is measured with the pressure transmitter PI12 of type *HE 1150* by *Hesch* with a pressure range of $0 \ldots 25\,\mathrm{bar(g)}$.

The differential pressures (PDI11 and PDI31) are measured with two transmitters of type *Jumo B 40.4302* with adjustable pressure ranges between $\pm 1000\,\mathrm{mbar(g)}$ with an output signal of $4 \ldots 20\,\mathrm{mA}$. For the vacuum pressure measurement, a cold cathode pressure transmitter type *PKR 251* of *Pfeiffer Vacuum* for the pressure range below $10^{-3}\,\mathrm{mbar(a)}$ and a compact Pirani capacitance pressure transmitter (PI22) type *PCR 280* of *Pfeiffer Vacuum* for the pressure range $10^{-3} \ldots 1000\,\mathrm{mbar(a)}$ are chosen. The signals are transferred to a DualGauge$^{\mathrm{TM}}$ measurement and control device *TPG 262* of *Pfeiffer Vacuum*, providing a $0 \ldots 10\,\mathrm{V}$ analogue output signal.

3.2.2 Temperature measurement

Because of the expected fast temperature changes and the necessity of measuring temperatures in the range of $4 \ldots 300\,\mathrm{K}$, typical low temperature sensors such as the CERNOX$^{\mathrm{TM}}$ sensors by *Lakeshore* cannot be used since they require the adjustment of the current supply for different temperature ranges. Due to their high sensitivity at low temperatures and sufficient sensitivity at ambient temperature at constant current, TVO sensors are chosen instead. More information on these Russian carbon resistance thermometers can be found in [49–51].

For the fast temperature measurement inside the cryogenic vessel, seven plain TVO temperature sensors (Figure 3.4(*a*)) are fixed at the measurement insert shown in Figure 3.5. Four of the plain TVO sensors are attached to horizontal wings of the

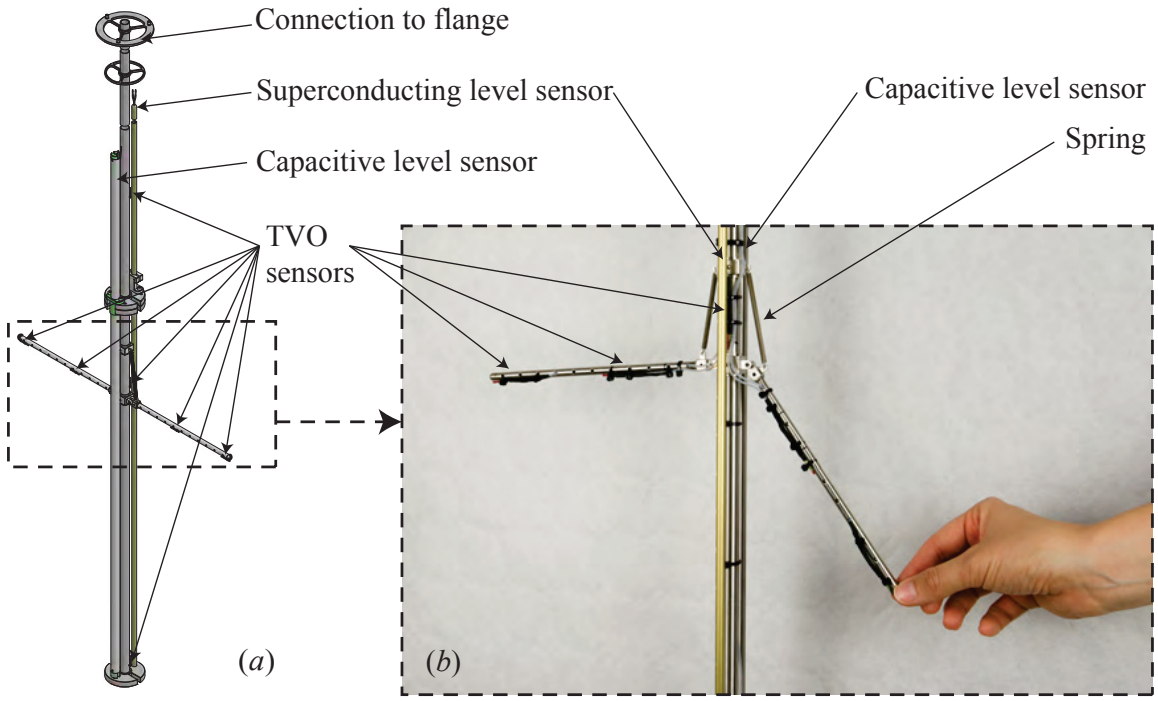

Figure 3.5: (*a*) CAD drawing of the measurement insert with TVO temperature sensors as well as capacitive and superconducting level sensors [26], and (*b*) close-up picture of the measurement insert.

measurement insert that unfold once having passed through the vent line [26]. They are complemented by three additional plain TVO sensors fixed at the top, middle and bottom of the measurement insert, respectively, to measure the temperature profile within the cryogenic fluid [26]. Further eight TVO sensors cast in copper cartridges as shown in Figure 3.4(*b*) are mounted to the top, bottom, left and right surfaces of both the cryogenic vessel and the radiation shield as shown in Figure 3.4(*c*) and Figure 3.2(*a*). Three more TVO sensors are mounted inside the vent line and quench gas line (Figure 3.4(*d*)). A constant current of 30 μA is supplied by a current source of *type 6221* by *Keithley* for the four-wire measurement method. The TVO sensors provide an analogue output signal of 0 . . . 200 mV.

3.2.3 Liquid level measurement

Besides experiments with different venting fluids, the use of different cryogenic fluids is also possible at PICARD. For nitrogen, a capacitive liquid level measurement is installed. The capacitor consists of two concentric tubes of $l_{\mathrm{Cyl}} = 75\,\mathrm{mm}$ length and $r_1 = 3.5\,\mathrm{mm}$ and $r_2 = 5.5\,\mathrm{mm}$ radius. This cylindrical capacitor is attached to the measurement insert shown in Figure 3.5. The signal is transmitted to a transducer of type *VEGACAL 62* by *Vega*. With the electric constant ϵ_0, the capacitance is determined by the gap between the two cylinders, by the surface and by the relative

Table 3.3: Relative permittivities ϵ_r at normal boiling point (nb) of selected cryogenic fluids in the gaseous (g) and liquid (l) phase [13].

	Argon	Nitrogen	Neon	Helium
$\epsilon_{r,g}$(nb)	1.0018	1.0022	1.0014	1.0066
$\epsilon_{r,l}$(nb)	1.5034	1.4327	1.1880	1.0569
$\epsilon_{r,g}$(nb)/$\epsilon_{r,l}$(nb)	1.50	1.43	1.19	1.05

permittivity $\bar{\epsilon}_r$ of the dielectric, in this case the cryogenic fluid. Since the geometry is kept constant in the test setup, the measured capacitance C_{Cyl} increases proportionally to $\bar{\epsilon}_r$ [52] with

$$C_{Cyl} = 2\pi \cdot \epsilon_0 \cdot \bar{\epsilon}_r \cdot \frac{l_{Cyl}}{r_2/r_1} \,. \tag{3.1}$$

Values for selected cryogenic fluids are listed in Table 3.3.

In the case of helium, the difference between $\epsilon_{r,g}$ and $\epsilon_{r,l}$ is insufficient for capacitive level measurements. Therefore, an additional superconducting level sensor by *AMI* with an active length of 1 m is attached to the measurement insert. The signal is transmitted to a liquid helium level monitor of type *AMI Model 135*, providing a 4 ... 20 mA analogue output signal.

3.2.4 Mass flow rate measurement

The venting mass flow is lead through a custom design orifice measuring section with an inlet and outlet diameter of $D_{Or} = 54.5$ mm flanged to the vacuum vessel. Exchangeable orifices manufactured by *TetraTec* of $d_{Or} = 12.5$ mm, 25 mm and 30 mm diameter are used for different venting mass flow rates.

For measuring the discharge mass flow rate, two exchangeable Venturi tubes manufactured by *Dosch Messapparate* with an inlet and outlet diameter $D_{Venturi} = 54.5$ mm and reduced diameters of $d_{Venturi} = 24.31$ mm and $d_{Venturi} = 33.64$ mm are used. The Venturi tube is installed upstream of the safety relief valve, since the expected two-phase flow downstream of the safety relief valve would make an accurate measurement impossible.

3.3 Data acquisition and processing

The data acquisition system (DAQ) comprises one *National Instruments* card of type *NI 9203* for signals in the range of 4 ... 20 mA and two *National Instruments* cards of type *NI 9205* for signals in the range of 0 ... 200 mV or 0 ... 10 V inserted in the *NI-CompactDAQ-USB-Chassis* of type *NI cDAQ-9178*. The analogue signals are converted with a resolution of 32 bit and transferred to a computer via USB. The DAQ is configured and the data are processed by an in-house software [53]. Sampling rates of the data acquisition system of up to 17 kHz are possible. For the experiments, sampling

rates up to 1 kHz using averaging of the data points are advised in order to reduce the noise to tolerable ranges without loosing important information. In comparison, existing experimental test facilities allow sampling rates in the range between 1 Hz [23, 24] and 12 Hz [37]. The chosen sampling rate for the cool-down, filling and warm-up is 5 Hz with a sampling clock rate of 500 samples per second and a sampling rate divider of 100. For the venting experiments, either sampling rates of 150 Hz (with a sampling clock rate of 750 samples per second and a sampling rate divider of 5), or 500 Hz (with a sampling clock rate of 2500 samples per second and a sampling rate divider of 5) are chosen. Both raw and processed data are recorded and stored in the ASCII-format.

3.4 Operation

In preparation of the experiments, the PICARD vacuum vessel is evacuated to a vacuum pressure below $p_V = 10^{-5}$ mbar, which requires vacuum pumping for at least three days prior to the start of cool-down. The safety relief valve is set to the required pressure by the manufacturer or at in-house facilities. Different adjustment methods for safety relief valves are discussed in Section 3.5. After mounting the safety relief valve at PICARD, a leak test is conducted. As such, the cryogenic vessel and piping are repeatedly evacuated and purged with helium gas. All valves connecting the PICARD cryogenic vessel with the helium recovery system are opened. The water bath heater is switched on, and the data acquisition for the cool-down is started.

The cryogenic fluid is supplied from a dewar through the filling line into the cryogenic vessel by applying an overpressure of $p = 100 \ldots 180$ mbar to the dewar using pressurized gaseous helium. During the filling process, the cryogenic fluid cools down the cryogenic vessel [26]. This also causes the vacuum pressure to decrease to below 10^{-6} mbar as the cold surface acts as a cryopump. The evaporated cryogenic fluid is lead through the exhaust gas line and hence heated up in the water bath in order to avoid air condensation at the surface of the pipes. When the required liquid level is reached, the filling line is disconnected manually and stored at the assembly jig [26]. The vacuum pumps are disconnected from the vacuum vessel to protect the turbopump from pressure shocks. Furthermore, the valves connecting the cryogenic vessel to the helium recovery system via the exhaust gas line are closed. The data acquisition for the cool-down is stopped.

The experiments presented in the following chapters have been conducted within the framework of an R&D collaboration between KIT and CERN on cryogenic pressure relief [54]. The settings of the different measurement points (MP) are listed in Table 3.4 and have been chosen in order to analyse the impact of the venting diameter (MP3, MP5, MP7) that will be discussed in Sections 4.2 to 4.5 and to investigate the influence of the venting fluid (MP1, MP2), of the Venturi tube (MP3, MP4) and of the set pressure (MP5, MP6), which will be discussed in Section 4.5. Just before opening the valve connecting the vacuum vessel with the venting section, the fast data acquisition for the experiment is started. The safety experiments are triggered by venting gas at ambient temperature through an orifice into the vacuum insulation space of the cryostat. In case of atmospheric air as venting fluid, the venting section is directly

Table 3.4: Settings of the measurement points (MP) for the venting of the insulating vacuum with the pressure of the safety relief valve set according to "initial audible discharge" (IAD) [14].

MP	Venting fluid	Orifice diameter mm	Initial filling level %	Set relief pressure IAD bar(g)	Sampling rate Hz
1	Nitrogen	12.5	25	2.6	150
2	Air	12.5	50	2.6	150
3	Air	25	60	7.6	500
4	Air	25	60	7.7	500
5	Air	12.5	80	2.0	500
6	Air	12.5	70	1.3	500
7	Air	30	60	6.0	500

opened to the surroundings. Because of the difficult removal of air humidity in the vacuum space after the experiments, it can be beneficial to use gaseous nitrogen supplied in the buffer vessel, especially for experiments where the cryogenic vessel is insulated with MLI.

The inflowing warm gas freezes out on the cold surface of the cryogenic vessel, causing a heat flux that is transferred to the cryogenic fluid. Both the temperature and the pressure of the cryogenic fluid increase until the opening pressure is reached and the cryogenic fluid is released through an opening safety relief device. The escaping cryogenic fluid is lead through a quench gas line to the helium recovery system of the institute.

After the experiment, the fast data acquisition is stopped and, if desired, the slower data acquisition for the warm-up is started. The venting section has to remain open to atmosphere in order to relieve the air and humidity evaporating from the surface of the cryogenic vessel. In order to enable the evaporation of water from the vacuum space, the vacuum vessel can be heated by a heating coil and purged with warm nitrogen gas. The test setup heats up during several days. The safety relief valve is demounted and the set pressure is again checked before the preparation for the next experiment can begin.

3.5 Adjustment methods for safety relief valves

In the applicable standards, the opening pressure is defined as the pressure when a safety relief valve commences to open under operating conditions [17], while the set pressure is the pressure at which a safety relief valve opens under predetermined conditions [17, 22]. However, these "predetermined conditions" are not strictly defined. For instance, DIN SPEC 4683 [14] lists four different procedures for the set pressure adjustment of safety relief valves: "initial audible discharge", "pop action" (for full-

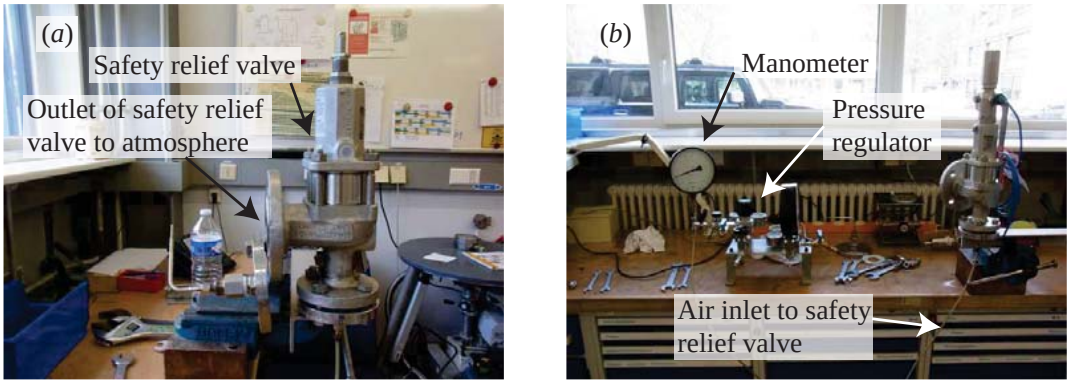

Figure 3.6: Setup for setting the pressure of the safety relief valves according to the method "initial audible discharge" at the Institute for Technical Physics (ITEP) at KIT.

lift safety relief valves), "start to leak pressure" and "bubble test". In the following, the methods "initial audible discharge" (IAD) and "bubble test" (BT) will be further discussed.

For adjusting the set pressure according to IAD at a test rig, the pressure at the inlet of the safety relief valve slowly increases until the first hissing of the released gas can be heard at the outlet of the safety relief valve [55]. According to the method BT, the safety relief valve inlet is also slowly pressurized, but the outlet is connected to a small tube instead of being open to atmosphere as in the case of IAD. The set pressure is reached when a predetermined amount of bubbles can be counted at the outlet of the tube immersed in a glass of water [56]. BT is also used for determining the leak tightness of safety relief valves [56]. For both methods, compressed air is used as test fluid.

The test rig assembled for setting the pressure of safety relief valves at the Institute of Technical Physics (ITEP) of KIT according to the methods IAD and BT is shown in Figure 3.6 and Figure 3.7, respectively. For setting the pressure, the valve is mounted on the test rig. The gas supply is connected to the inlet of the safety relief valve through a small tube with an inner diameter of 4 mm, intercepted by a pressure regulator and a manometer. In the setup for the method IAD, the valve outlet directly opens to atmosphere as can be seen in Figure 3.6. For determining the pressure according to BT, a small capillary is flanged to the outlet of the safety relief valve. This capillary is bend by 90 ° to have the tube opening well below the water surface of a glass of water perpendicular to the tube as shown in Figure 3.7. For both procedures, the spring of the safety relief valve is adjusted and all valves are closed. Hence, the pressure is increased very slowly and monitored with the manometer. The set pressure according to IAD is found once a hissing sound of discharging air can be heard at the outlet of the safety relief valve. In this work, the first bubble is used for setting the pressure of the safety relief valve according to the method BT. More information on leakage tests similar to the here described BT with detailed information on the test apparatus and test procedure can be found in [56].

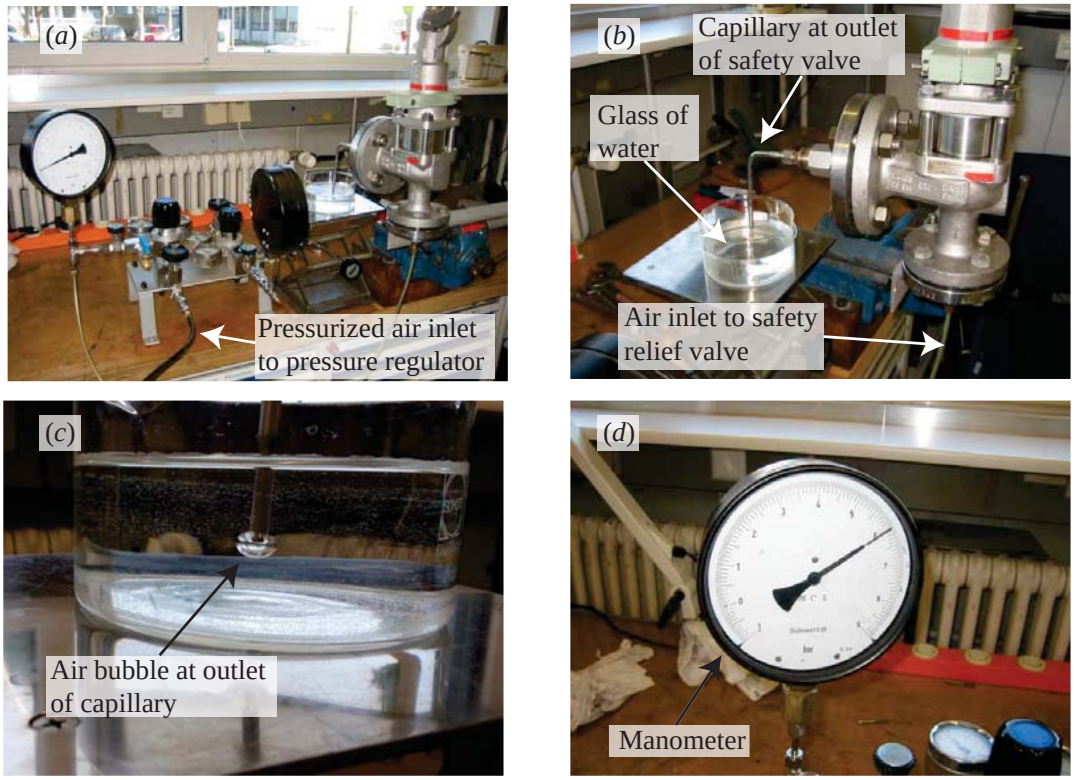

Figure 3.7: Setup for setting the pressure of the safety relief valves according to the method “bubble test” at ITEP, KIT.

As a consistency test, the first audible discharge of a new safety relief valve by *Leser* has been measured at ITEP and was found to correspond well with the set pressure adjusted by *Leser* using the same method, which gives confidence in the test procedure at ITEP. BT and IAD tests are conducted before and after each experiment to check for alterations in the set pressure and possible damage to the safety relief valve during the experiment. For instance, damage to the disk of the safety relief valve caused by unstable operation during discharge would manifest in a lower BT pressure and the disk would be replaced before the start of the next experiment. The procedure IAD is chosen to define p_{set} for the evaluation of the dataset in this work, as it is specified for the applied valves by the manufacturer.

3.6 Data analysis

3.6.1 Evaluation of the venting mass flow rate

For standardized orifice measurement sections, the venting mass flow rate is calculated according to [57] as

$$\dot{m}_{\mathrm{In,Or}} = \frac{C_{\mathrm{Or}}}{\sqrt{1-\beta_{\mathrm{Or}}^4}} \cdot \epsilon_{\mathrm{Or}} \cdot \frac{\pi}{4} \cdot d_{\mathrm{Or}}^2 \cdot \sqrt{2 \cdot (p_{\mathrm{A}} - p_{\mathrm{V}}) \cdot \rho_{\mathrm{A}}}\,, \tag{3.2}$$

with the flow coefficient C_{Or}, the diameter ratio $\beta_{\mathrm{Or}} = d_{\mathrm{Or}}/D_{\mathrm{Or}}$ and the expansion coefficient ϵ_{Or} as defined in [57]. Since no standardized orifice measurement section can be used in PICARD because of space and design limitations, a custom design measurement section by *TetraTec* is used with the provided calibration polynomial

$$\begin{aligned}\dot{m}_{\mathrm{In}} =& \frac{\pi}{4} \cdot d_{\mathrm{Or}}^2 \cdot \sqrt{2 \cdot \rho_{\mathrm{V,Strd}} \cdot \frac{\mathrm{PI22}}{p_{\mathrm{Strd}}} \cdot \frac{T_{\mathrm{Strd}}}{\mathrm{TI31}}} \cdot \\ & \left(C_{\mathrm{A}} \cdot \Delta p_{\mathrm{Or}}^{0.5} + C_{\mathrm{B}} \cdot \Delta p_{\mathrm{Or}} + C_{\mathrm{C}} \cdot \Delta p_{\mathrm{Or}}^{1.5} + C_{\mathrm{D}} \cdot \Delta p_{\mathrm{Or}}^2 + C_{\mathrm{E}} \cdot \Delta p_{\mathrm{Or}}^{2.5}\right)\,,\end{aligned} \tag{3.3}$$

with the density of the venting fluid $\rho_{\mathrm{V,Strd}}$ under standard conditions, i.e. at $p_{\mathrm{Strd}} = 1.0133\,\mathrm{bar(a)}$ and $T_{\mathrm{Strd}} = 293.15\,\mathrm{K}$, the calibration coefficients $C_{\mathrm{A}} \ldots C_{\mathrm{E}}$ and the pressure difference $\Delta p_{\mathrm{Or}} = \mathrm{PI32} - \mathrm{PI22}$. The data taken with the differential pressure transmitter PDI31 cannot be used in the dynamic venting process due to the nominal response time of 0.5 s.

3.6.2 Evaluation of the deposition mass flow rate

Following Eq. (2.12), the deposition mass flow rate $\dot{m}_{\mathrm{Dep}}$ caused by desublimation and condensation of the venting fluid on the cold surface of the cryogenic vessel is calculated from measurement data by applying the ideal gas law differentiated with respect to time as

$$\dot{m}_{\mathrm{Dep}} = \dot{m}_{\mathrm{In}}(\mathrm{PI32}, \mathrm{PI22}, \mathrm{TI31}) - \frac{\frac{\mathrm{d}p_{\mathrm{V}}}{\mathrm{d}\tau} \cdot (V_{\mathrm{V}} - V_{\mathrm{Cr}})}{R_{\mathrm{V}} \cdot \mathrm{TI31}}\,. \tag{3.4}$$

In order to obtain $\mathrm{d}p_{\mathrm{V}}(\tau)/\mathrm{d}\tau$, the data points taken during the experiment must be interpolated to a function $p_{\mathrm{V}}(\tau)$. Exemplary for MP7, the data points of the vacuum pressure during the first 15 s of the experiment are shown in Figure 3.8 with the measurement uncertainty displayed in grey. Although the pressure increase looks fairly smooth in Figure 3.8 (a), a zoom-in to the dataset shown in Figure 3.8 (b) reveals that the data are subject to noise. The interpolation of the original dataset would therefore not represent the general trend, but make an evaluation of especially $\mathrm{d}p_{\mathrm{V}}(\tau)/\mathrm{d}\tau$ impossible because of the large short-term fluctuations. Therefore, the simple moving average (SMA) method, which is an established method in signal processing, is used to smooth out the short-term fluctuations by calculating the arithmetic mean of n subsequent data points of the dataset $\{a_i\}_{i=1}^{N}$, thus creating the new dataset $\{s_i\}_{i=1}^{N-n+1}$

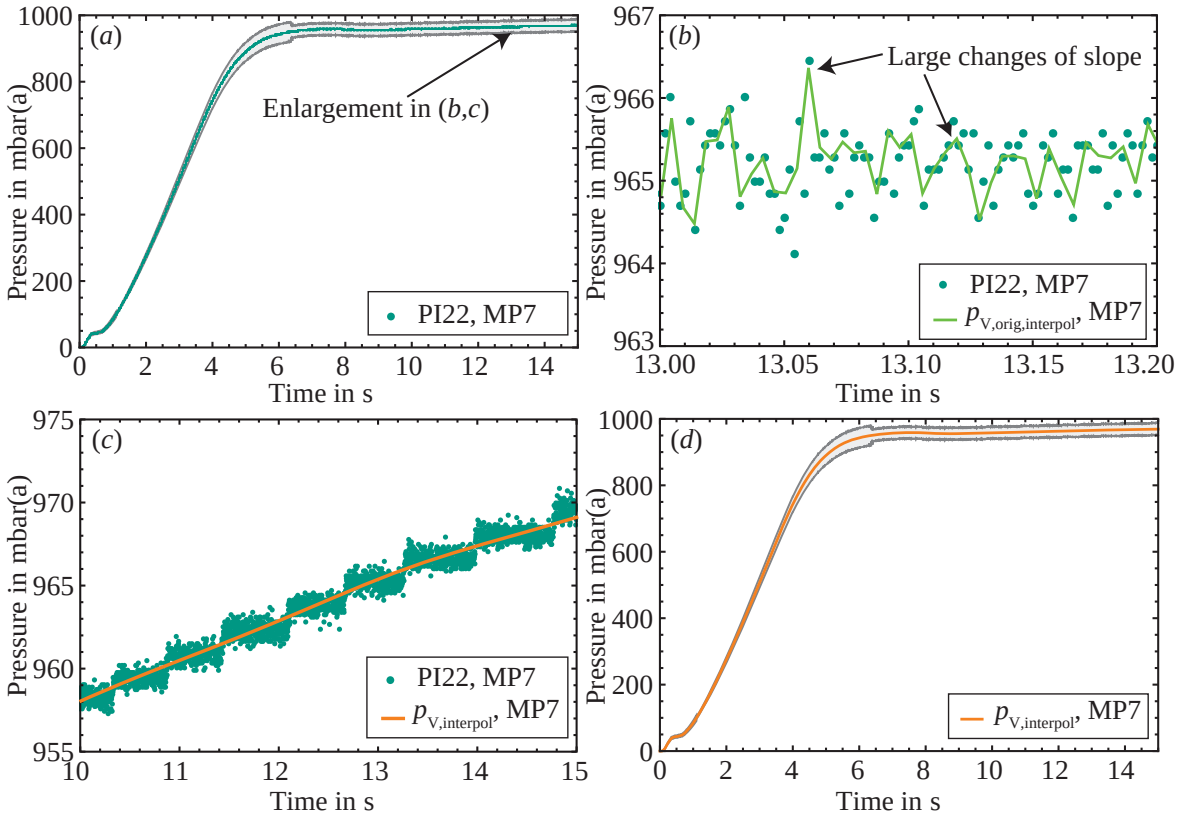

Figure 3.8: (*a*) Exemplary vacuum pressure measured with PI22 during the first 15 s of MP7, (*b*) zoom-in to the directly spline-fitted interpolation function of the dataset, (*c*) zoom-in to the interpolation function after smoothing the dataset with moving averages and (*d*) resulting smoothed interpolating function of the vacuum pressure during the first 15 s of MP7.

following

$$s_i = \frac{1}{n} \sum_{j=1}^{i+n-1} a_j \,, \tag{3.5}$$

"moving" data point by data point through the original dataset [58]. For the vacuum pressure increase, n is adjusted to

$$n = \begin{cases} 40 & , 0\,\mathrm{s} \leq \tau < 0.08\,\mathrm{s} \\ 100 & , 0.08\,\mathrm{s} \leq \tau < 7.2\,\mathrm{s} \\ 400 & , \tau \geq 7.2\,\mathrm{s}\,, \end{cases} \tag{3.6}$$

taking the fast changes of slope of the vacuum pressure within the first milliseconds and the decreasing change of slope after some seconds into account. More information on signal processing can be found in [59]. In the next step, the interpolated function $p_{\mathrm{V,interpol}}(\tau)$ is calculated by spline-fitting $\overline{\mathrm{PI22}}_{\mathrm{SMA}}$ using cubic splines shown as an orange line in Figure 3.8 (*c*) and (*d*). Hence, the derivative $\mathrm{d}p_{\mathrm{V}}/\mathrm{d}\tau$ needed for the

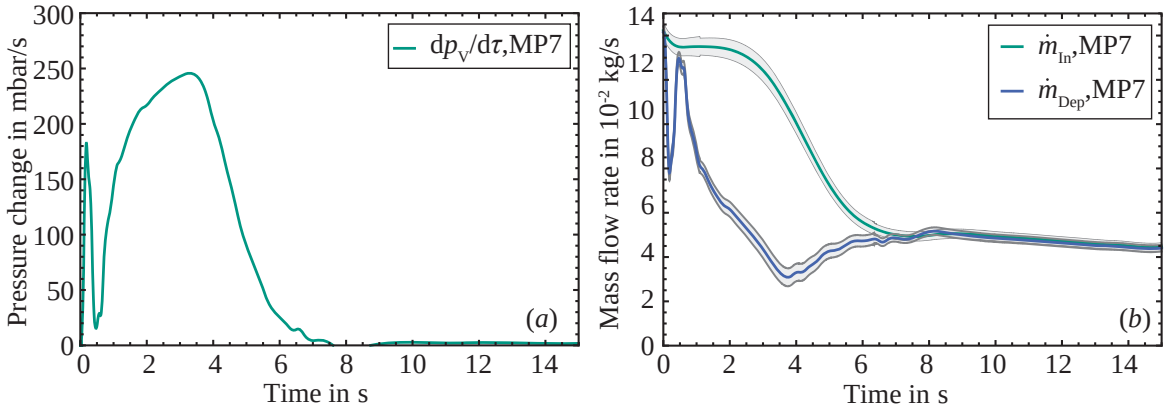

Figure 3.9: (a) Derivative of the vacuum pressure with respect to time and (b) smoothed venting and deposition mass flow rate exemplary for MP7 during the first 15 s after the start of the experiment.

calculation of $\dot{m}_{\mathrm{Dep}}$ is calculated by differentiating $p_{\mathrm{V,interpol}}(\tau)$ numerically with respect to time

$$\frac{\mathrm{d}p_{\mathrm{V}}(\tau)}{\mathrm{d}\tau} = \frac{\mathrm{d}p_{\mathrm{V,interpol}}(\tau)}{\mathrm{d}\tau} \tag{3.7}$$

as shown exemplary in Figure 3.9(a) for MP7.

The resulting deposition mass flow rate calculated according to Eq. (3.4) as well as a smoothed curve of the venting mass flow rate are shown in Figure 3.9(b). For the discussion of results in Section 4.4, the first 0.2 s of $\dot{m}_{\mathrm{In}}$ and $\dot{m}_{\mathrm{Dep}}$ are not taken into consideration due to the response time of the sensors and the delay caused by the piping between the vacuum vessel and the venting orifice.

3.6.3 Evaluation of the heat flux

The heat flux caused by deposition of the venting fluid, $\dot{q}_{\mathrm{Dep}}$, can hence be calculated following from Eq. (2.15) as

$$\dot{q}_{\mathrm{Dep}} = \frac{1}{A_{\mathrm{Cr}}} \cdot \dot{m}_{\mathrm{Dep}} \cdot \left[h_{\mathrm{V}}(\mathrm{PI22}, T_{\mathrm{V}}) - h_{\mathrm{W}}(\mathrm{PI22}, \bar{T}_{\mathrm{W}}) \right] , \tag{3.8}$$

with the enthalpy of the gaseous and the deposited venting fluid, h_{V} and h_{W}. The temperature of the aluminium radiation shield in PICARD is found only little below room temperature during the experiments, and cooling of the venting fluid through contact with the radiation shield is thus considered negligible. Furthermore, gas molecules have a high sticking probability to surfaces at cryogenic temperatures [60]. Consequently, the temperature of the gaseous venting fluid inside the vacuum space is considered as $T_{\mathrm{V}} = T_{\mathrm{A}} = \mathrm{TI31}$. For the evaluation of h_{W}, the average measured wall temperature $\bar{T}_{\mathrm{W}}$ is used, where each data point $\bar{T}_{\mathrm{W}_i}$ is the arithmetic mean

$$\bar{T}_{\mathrm{W},i} = \frac{\mathrm{TI21}_i + \mathrm{TI22}_i + \mathrm{TI23}_i + \mathrm{TI24}_i}{4} . \tag{3.9}$$

Humid air, which is used as venting fluid in MP2 to MP7, consists of about 74.9 ma% nitrogen, 22.9 ma% of oxygen, 1.3 ma% of argon and 0.9 ma% of water, exemplary calculated based on [13] and the relative humidity MI31 measured in MP7. However, no real-gas enthalpy data of humid air could be found in literature, which makes simplifying assumptions necessary. On the other hand, solid enthalpy data for nitrogen is given in [11] and is linearly spline-fitted and combined with the gaseous and liquid fluid property data from [13, 61] as

$$h_{\mathrm{N2}} = \begin{cases} h_{\mathrm{N2,Refprop}}(p,T) & T > T_{\mathrm{Trip,N2}} \\ h_{\mathrm{N2,Iwasa}}(T) - \Delta h_{\mathrm{N2,Reference}} & T \leq T_{\mathrm{Trip,N2}}\,, \end{cases} \tag{3.10}$$

normalizing the data from [11] to the same reference state as in [13,61] with the enthalpy difference $\Delta h_{\mathrm{N2,Reference}}$ between the liquid enthalpies $h_{\mathrm{N2,l}}$ from [11] and [13, 61] given at the triple point

$$\Delta h_{\mathrm{N2,Ref}} = h_{\mathrm{N2,Iwasa,l}}(T_{\mathrm{Trip,N2}}) - h_{\mathrm{N2,Refprop,l}}(T_{\mathrm{Trip,N2}}) \tag{3.11}$$

to calculate $(h_{\mathrm{V,N2}} - h_{\mathrm{W,N2}})$. For the temperature range of interest during the venting experiments, the difference between $\dot{q}_{\mathrm{Dep,N2}}$ for pure nitrogen and $\dot{q}_{\mathrm{Dep,ha}}$ for a simplified ideal mixture of humid air was found to be below 10 %. Therefore, the available enthalpy data of pure nitrogen is used as a simplification for the further evaluation of the dataset. The ideal mixture calculation of $\dot{q}_{\mathrm{Dep,ha}}$ can be found in Appendix A.2.

3.6.4 Evaluation of the discharge mass flow rate

Two different methods are applied for measuring the discharge mass flow rate. The first method is a flow measurement with a Venturi tube according to DIN EN ISO 5167-4 [62] with

$$\dot{m}_{\mathrm{Out}} = \frac{C_{\mathrm{Venturi}}}{\sqrt{1-\beta_{\mathrm{Venturi}}^4}} \cdot \epsilon_{\mathrm{Venturi}} \cdot \frac{\pi}{4} \cdot d_{\mathrm{Venturi}} \cdot \sqrt{2 \cdot \mathrm{PDI11} \cdot \rho_{\mathrm{Cr}}\left(\mathrm{PI12}, \mathrm{TI11}\right)}\,, \tag{3.12}$$

where one of the two differently sized Venturi tubes is used. Same as for the orifice mass flow measurement (Eq. (3.2)), the mass flow rate depends on the diameter ratio $\beta_{\mathrm{Venturi}} = d_{\mathrm{Venturi}}/D_{\mathrm{Venturi}}$ as well as on the flow coefficient $C_{\mathrm{Venturi}} = 0.995$ for classical Venturi tubes [62] and the expansion coefficient $\epsilon_{\mathrm{Venturi}}$ as defined in [62].

The second method is based on the measurement of the temperature T_{Cr} and the pressure p_{Cr} inside the cryogenic vessel. As T_{Cr} is measured at different locations in PICARD, an average temperature $\bar{T}_{\mathrm{Cr},i}$ for each time step with

$$\bar{T}_{\mathrm{Cr},i} = \frac{\mathrm{TI12}_i + \mathrm{TI13}_i + \mathrm{TI14}_i + \mathrm{TI15}_i + \mathrm{TI18}_i}{5} \tag{3.13}$$

is calculated. The temperature sensors TI16 and TI17 are not considered in order to avoid a data overweight in the middle of the cryogenic vessel. The changes in the stored mass m_{Cr} over time τ (and therefore also the discharge mass flow rate $\dot{m}_{\mathrm{Cr}}$) can be

calculated with a constant total volume V_{Cr} and the time-dependent average density of the cryogenic fluid $\bar{\rho}_{\mathrm{Cr}} = f(p_{\mathrm{Cr}}, \bar{T}_{\mathrm{Cr}})$ as

$$\dot{m}_{\mathrm{Cr}}(\tau) = \frac{\mathrm{d}m_{\mathrm{Cr}}(\tau)}{\mathrm{d}\tau} = \frac{\mathrm{d}(V_{\mathrm{Cr}} \cdot \bar{\rho}_{\mathrm{Cr}} \left[\mathrm{PI12}, \bar{\mathrm{T}}_{\mathrm{Cr}}\right])}{\mathrm{d}\tau}. \tag{3.14}$$

However, large temperature gradients within the cryogenic fluid can make an evaluation difficult. Therefore, measurement uncertainties in the range of up to 25 % must be expected [48].

3.6.5 Measurement uncertainties

The measurement uncertainties are calculated following the *Guide to the Expression of Uncertainty in Measurement* (GUM) [63], where the sources of uncertainties can be divided in Type A and B: While Type A uncertainties consider the statistics of repeated observations from a probability density function, Type B uncertainties are obtained from an assumed probability function, for instance manufacturer's specifications or calibration certificates. From the uncertainties u_{A} for Type A and u_{B} for Type B, the combined standard uncertainty u_{C} for the value X_{i} with its estimate x_{i} is calculated by

$$u_{\mathrm{C}}(x_i) = \sqrt{u_{\mathrm{A}}^2(x_i) + u_{\mathrm{B}}^2(x_i)} \tag{3.15}$$

for all measurements where several sensors have been used for measuring average values. Where only one sensor could be used, the Type A measurement uncertainties cannot be considered since no statistics of the highly dynamic measurements during venting of the insulating vacuum can be obtained, resulting in

$$u_{\mathrm{C}}(x_i) = u_{\mathrm{B}}(x_i)\,. \tag{3.16}$$

Where average values of data taken by different sensors are used, the maximum and minimum values are considered for calculating the measurement uncertainty.

If a measurand Y is not measured directly, but is determined from N other quantities $X_1, X_2, \ldots, X_{\mathrm{N}}$ through a function f with

$$Y = f\left(X_1, X_2, \ldots, X_N\right)\,, \tag{3.17}$$

the combined standard uncertainty $u_{\mathrm{C}}(y)$ is calculated from uncertainty propagation by

$$u_{\mathrm{C}}^2(y) = \sum_{i=1}^{N} \left(\frac{\partial f(x_1, x_2, \ldots, x_N)}{\partial x_i} \right)^2 \cdot u^2(x_i)\,. \tag{3.18}$$

A rectangular distribution of the Type B uncertainties is assumed. The uncertainties given by the manufacturers are based on a coverage factor $k = 2$, which corresponds to a level of confidence of approximately 95 % [63].

For the Type B uncertainties of the pressure measurement, the measurement chain including calibration, the supply isolators from *Wago* used for HART communication with the sensor and the analogue-to-digital converter (ADC) NI 9203 are considered.

The TVO sensors have been calibrated at the ITEP calibration facility to a measurement uncertainty of ±1 % of the measured value for a range of 3.9 . . . 299 K, which is taken into account combined with the uncertainties of the ADC NI 9205 and the current source *Keithley 6221*. Other uncertainties induced by the long-term stability, the overheating of the sensor and cabling and the approximation of the calibration polynomial are not considered for the TVO sensors because of their negligible influence with respect to the overall uncertainty [64]. The uncertainty for the helium liquid level measurement comprises the uncertainties of the liquid helium level monitor *AMI model 135*, of the ADC *NI 9203* and of the geometric assembly situation.

For the evaluation of the venting mass flow rate, the uncertainties of the vacuum pressure PI22, of the ambient pressure PI32 and of the ambient temperature TI31 are combined with the calibration uncertainty of the orifices given by the manufacturer. Furthermore, the uncertainty of the differential pressure measurement caused by the additional pressure drop in the piping between the orifice measurement section and the vacuum vessel is considered. The uncertainty of the deposition mass flow rate is calculated from the uncertainty of the ambient temperature TI33 and the estimated uncertainty of the volume of the vacuum space. The uncertainties of the vacuum pressure can be assumed as systematic and consequently disappear in the derivative. Therefore, the measurement uncertainty for the change in vacuum pressure is neglected for the further calculations. The uncertainty of $\dot{q}_{\mathrm{Dep}}$ is calculated from the uncertainty of $\dot{m}_{\mathrm{Dep}}$ combined with the uncertainty of the enthalpy difference between h_{V} and h_{W} caused by the simplification of using pure nitrogen as venting fluid instead of humid air. For the discharge mass flow measurement with the Venturi tubes, the Type B uncertainties of PDI11, PI12 and TI11 are combined with the uncertainty of the calibration of the Venturi tubes given by the manufacturer. The uncertainty of the discharge mass flow rate calculated from the change of state inside the cryogenic vessel is estimated from the uncertainty of the cryogenic volume and the temperature and pressure measurement inside the cryogenic vessel as explained in [48]. Exemplary calculations of the measurement uncertainties for selected measurement chains can be found in Appendix A.3.

3.7 Performance during cool-down and filling

In this section, the processes during the cool-down and filling of the cryogenic vessel are described in detail exemplary for the preparation of experiment MP2 [27]. Figure 3.10(a) shows the helium temperature over time at different levels inside the cryogenic vessel from the start of the cool-down process to the time when the filling line is disconnected. At first, the temperature inside the helium cryostat decreases slowly until the filling line has cooled down and liquid can be transferred to the cryogenic vessel. The temperature at the top of the vessel decreases slower than at the bottom since the liquid helium enters the vessel at the bottom. The cryogenic vessel cools down through the evaporation of the inflowing liquid helium.

The stagnation of the temperature decrease after about 25 min is caused by the decreasing enthalpy difference between the inflowing and released helium at constant

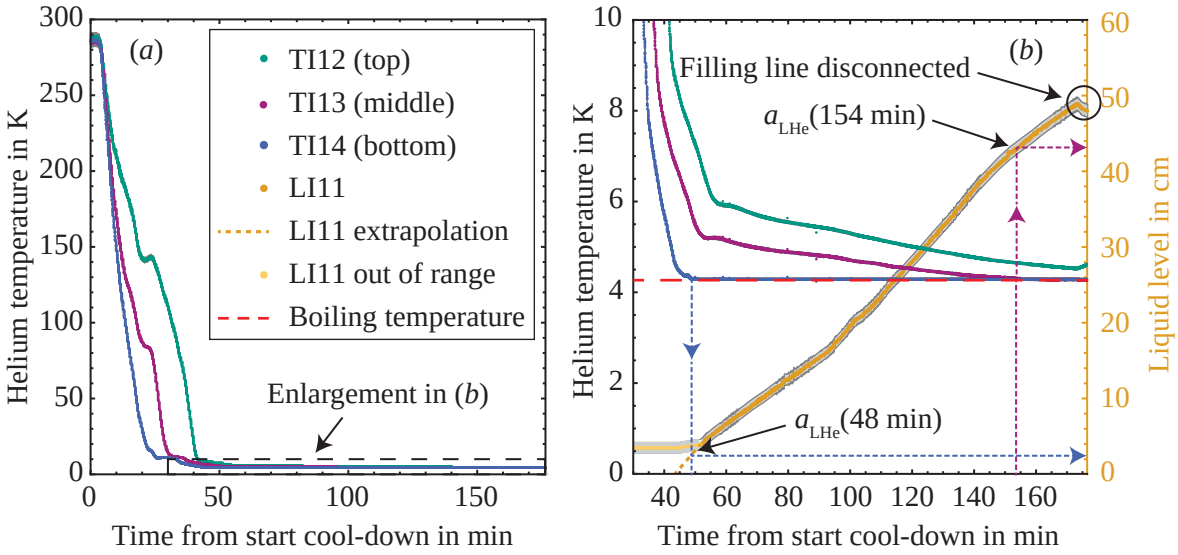

Figure 3.10: (*a*) Temperature profile and (*b*) enlarged temperature profile and helium liquid level during the cool-down and filling process of the PICARD cryogenic vessel [27]. The position of the sensors is shown in Figure 3.3.

supply mass flow rate. Manually, the overpressure applied to the dewar vessel is then increased, resulting in an increase in the liquid helium supply mass flow rate. Consequently, the cryogenic vessel cools down further until the boiling temperature of helium is reached and the first liquid remains in the cryostat.

The temperature measurement during the liquid filling process is used to validate the liquid level measurement, which is explained in the following [27]. Starting 45 min after the start of cool-down, an enlarged temperature profile complemented with the liquid level measured with the sc. level sensor LI11 is shown in Figure 3.10(*b*). Because of the design, the helium liquid level a_{LHe} can only be measured from a height of about $a_{\mathrm{LHe,0}} = 3.5\,\mathrm{cm}$ above the bottom, resulting in

$$a_{\mathrm{LHe}} = a_{\mathrm{LHe,measured}} + a_{\mathrm{LHe,0}}\,. \tag{3.19}$$

For $a_{\mathrm{LHe}} \leq 3.5\,\mathrm{cm}$, the liquid level is linearly extrapolated shown as a dashed orange line, while the data points for this invalid range are printed in lighter orange.

During the cool-down and filling process, the helium pressure is measured with the pressure sensor PI12 to about 0.1 bar(g). Once the temperature sensors are covered with liquid, the corresponding boiling temperature of $T_{\mathrm{b,He}} = 4.3\,\mathrm{K}$ can be measured with the temperature sensors at known position. As shown in Figure 3.10(*b*), the temperature sensor TI14 fixed to the measurement insert at a height of 2.2 cm from the bottom reaches $T_{\mathrm{b,He}}$ after 48 min, which is in good agreement with the extrapolated liquid level curve. The same consistency is found for TI13, which is fixed in the middle of the cryogenic vessel and reaches $T_{\mathrm{b,He}}$ after 154 min, which corresponds well with $a_{\mathrm{LHe}}(154\,\mathrm{min}) = 43.5\,\mathrm{cm}$.

In this example, the combined cool-down and filling process to a liquid level of

49 cm (which corresponds to about 60 L of liquid helium) takes about 175 min. During this time, 183 l of liquid helium are transferred from the dewar vessel to the PICARD cryostat. The cryogenic vessel temperature decreases at a rate of up to 12 K/min. The cold surface of the cryogenic vessel acts as a more and more effective cryopump with decreasing temperature. Thus, the measured vacuum pressure decreases from $3.8 \cdot 10^{-6}$ mbar in the beginning to $5.7 \cdot 10^{-7}$ mbar at the end of the filling process in this example. In the last three minutes of the filling process shown in Figure 3.10(b), the filling line is disconnected, resulting in a small liquid level decrease and temperature increase.

During idle time, the liquid level decreases with a rate of about 3.2 mm/min due to a heat input of about $\dot{Q} = 17$ W estimated from

$$\dot{Q} = \dot{m}_\mathrm{v} \cdot \Delta h_\mathrm{v} = \frac{\Delta V_\mathrm{LHe}}{\Delta \tau} \cdot \rho_\mathrm{l}(p_\mathrm{Cr}, T_\mathrm{b,Cr}) \cdot \Delta h_\mathrm{v} \tag{3.20}$$

with the helium enthalpy of evaporation Δh_v and evaporating helium mass flow rate $\dot{m}_\mathrm{v}$ calculated from the measured change in liquid volume ΔV_LHe over the time period $\Delta\tau$ and the liquid helium density ρ_l at $T_\mathrm{b,He} = 4.3$ K calculated using fluid property data [13, 65]. Considering that the PICARD cryostat has not been insulated with MLI, but is only vacuum insulated with an aluminium radiation shield during this measurement, this is rated a sufficiently good performance with a liquid level stable enough to conduct the experiments.

CHAPTER 4

Results of first venting experiments

4.1 Vacuum pressure increase

In the following sections, exemplary experimental results of venting experiments conducted in the course of this work in the framework of the R&D collaboration between KIT and CERN on cryogenic pressure relief [54] are discussed with focus on the vacuum pressure increase, the helium pressure and temperature increase as well as on the heat flux and discharge mass flow rate. The vacuum pressure measured with the pressure transducer PI22 is shown in Figure 4.1 exemplary for the experiments MP7 using a large orifice of $d_{\mathrm{Or}} = 30\,\mathrm{mm}$ (in the following referred to as major LIV) and MP5 using a small orifice of $d_{\mathrm{Or}} = 12.5\,\mathrm{mm}$ (in the following referred to as minor LIV). For both experiments, the data were taken with a sampling rate of 500 Hz.

With the exception of the first milliseconds after the start of the venting process, the vacuum pressure during major LIV rises almost linearly with time in the first 7 s until about 950 mbar(a) are reached as can be seen in Figure 4.1(a). Afterwards, the vacuum pressure increases very slowly to ambient pressure that is reached after about 1.5 min. An enlargement of the first 3 s is shown in Figure 4.1(b). In these first moments, the vacuum pressure in MP7 rises with a changing slope between 0.3 and 0.7 s after the start of the venting. During this period, the surface of the cold cryogenic vessel acts as an almost ideal cryopump and most of the air flowing into the vacuum space is "trapped" on the cold surface. As can be seen in Figure 4.1, the uncertainty of the vacuum pressure measurement chain displayed in grey increases with increasing pressure with a step in the uncertainty curves at 950 mbar, when the specified accuracy of the pressure transmitter in % of the measured value changes its range.

On the other hand, the vacuum pressure during minor LIV does not increase rapidly to ambient pressure, but remains below 10 mbar for the first 25 s since the venting mass flow rate does not exceed the cryopumping capacity of the cold surface. After 25 s, the vacuum pressure in MP5 slowly starts to increase and reaches ambient pressure after about 80 s.

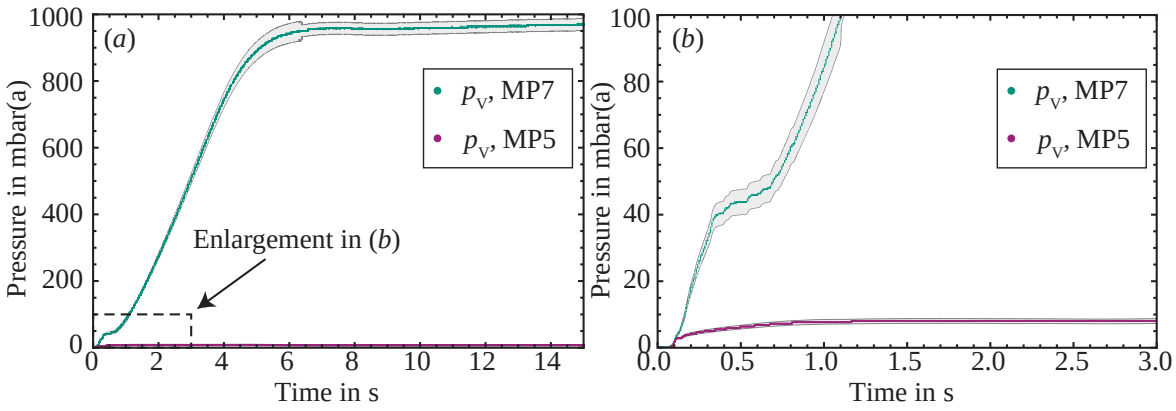

Figure 4.1: Vacuum pressure increase measured with PI22 during major LIV (MP7) and minor LIV (MP5) (*a*) for the first 15 s and (*b*) zoom-in to the first 3 s of the venting experiments.

4.2 Helium temperature and pressure increase

Figure 4.2 shows the helium temperature and pressure increase over time with the corresponding measurement uncertainties for the first 15 s from the start of the venting process during major LIV for MP7 and minor LIV for MP5. The processes inside the cryogenic vessel that follow the venting of the insulating vacuum can be divided into three phases I, II and III [27]: In phase I, the helium temperature and pressure increase in the closed cryogenic vessel. Before the safety relief device opens, the average change of state is isochoric since volume and mass of the helium in the cryogenic vessel remain constant. The unstable operation of the safety relief valve can be seen in phase II: During the repeated and fast opening and closing of the safety relief valve (chattering, pumping), both the helium temperature and pressure are subject to strong fluctuations. In phase III, helium is stably released through the safety relief valve.

Pumping or chattering occurs when the inlet pressure drops quickly below the reseating pressure of the safety relief valve during discharge and is typically caused by large pressure drops in the inlet piping and over-sizing of the safety relief valve [14, 27, 29]. AD 2000 [19] names a reseating pressure of $\geq 5\,\%$ of the relieving pressure p_0, while DIN EN ISO 4126-1 [17] states $5 \ldots 15\,\%{\cdot}p_0$ for compressible media. Therefore, the pressure drop in the inlet piping is limited to 3 % of the difference between the set pressure and the back pressure p_b in common design codes [19, 66]. However, larger pressure losses can be necessary and tolerable for cryogenic applications in order to reduce heat input to the system [14, 27, 29]. In MP7 and MP5, the pressure losses are estimated to 1.9 % and 5.2 % of $(p_0 - p_\mathrm{b})$, respectively. Chattering in MP7 and MP5 could not be prevented by the use of a damper, an O-ring placed on the spindle of the safety relief valve.

For the sizing of the safety relief valve in MP7, a typical constant heat flux of $4\,\mathrm{W/cm^2}$ [24] was assumed, while a constant heat flux of $1.25\,\mathrm{W/cm^2}$ estimated based on model calculations [16] was used for minor LIV. For these conditions, the safety relief

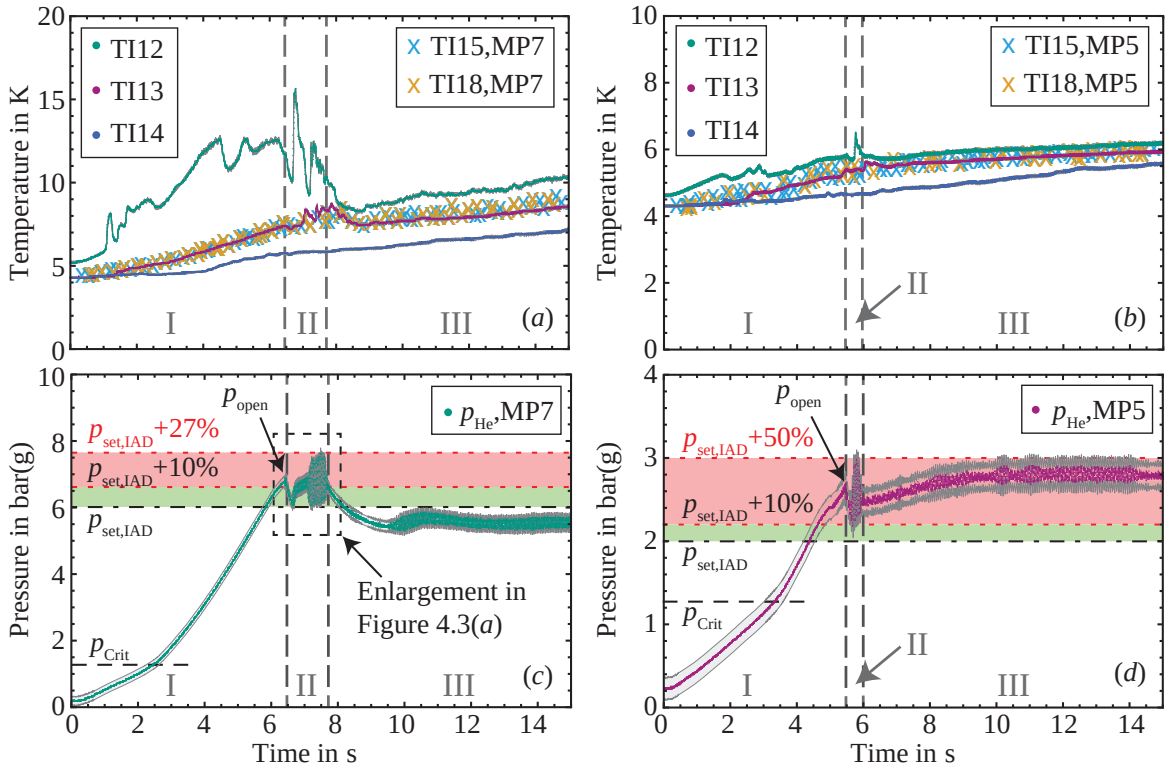

Figure 4.2: (a,b) Helium temperature and (c,d) helium pressure increase in the PICARD cryogenic vessel over time after start of the venting process for the first 15 s during (a,c) major LIV (MP7) and (b,d) minor LIV (MP5). In phase I, the cryogenic vessel is closed. Phase II shows the unstable operation of the safety relief valve, before helium is stably released in phase III.

valves of size DN25 are slightly over-sized by about 3.5 % in MP7 and about 10.5 % in MP5, considering the common design rules explained in Section 2.3. However, safety relief valves are only available in certain nominal sizes such as DN20, DN25, DN32 etc. with diameter increments of about 27 % [27, 67]. Besides, incidents with heat fluxes below the maximum design case and consequently smaller discharge mass flow rates are always possible and the safety relief system must be able to cope with such situations [27].

4.2.1 Helium temperature increase

The helium temperature inside the PICARD cryogenic vessel during the first 15 s of MP7 and MP5 is shown in Figure 4.2(a) and (b). For both experiments, a temperature stratification between the helium at the bottom (measured at a height of 30 mm from the bottom of the vessel with TI14), the middle (measured at a height of 470 mm with TI13) and the top (measured at a height of 770 mm with TI12) occurs, while the horizontal temperature gradient between TI15, TI13 and TI18 is small [27]. A

considerable temperature stratification is observed during all experiments conducted in the course of this work and can be explained by the larger height of the cryogenic vessel compared to the radius as well as by the existence of the two phases (liquid and gas) at the beginning of the experiment. The helium temperatures inside the PICARD cryogenic vessel during MP7 displayed in Figure 4.2(a) show a larger stratification over the height than during MP5 shown in Figure 4.2(b). Especially in phase I of MP7, when the safety relief valve is closed, the temperature difference between the helium at the bottom (TI14) and the top (TI12) increases and reaches up to 8 K for a short time.

The different temperature gradients between MP7 and MP5 can be explained by the design of PICARD, where the safety relief valve is mounted at 1.3 m above the cryostat at ambient temperature, i.e. the vent line is filled with warm helium gas. Due to molecular gas movement, the helium gas inside the cryogenic vessel warms up once the cryogenic vessel is closed after the filling process. A stratification between ambient temperature in the vent line and saturation temperature close to the gas-liquid interface builds up. MP7 is conducted with an initial liquid level of about 60 % (which corresponds to about 66 l of liquid helium) at the start of the experiment with a large gaseous volume around the upper temperature sensor TI12. On the other hand, the initial liquid level during MP5 is about 80 %, i.e. just below TI12, resulting in almost saturation temperature measured in the sub-critical helium at the location of the sensor.

During the unstable operation of the safety relief valve in phase II, especially the temperature measured in the upper part of the cryogenic vessel is subject to considerable fluctuations [27]. The temperature gradient between the helium at the top and bottom of the cryogenic vessel decreases, which can be explained by the internal mixing of the helium during discharge. In phase III, the temperature at the different locations inside the cryogenic vessel increases continuously for both experiments MP7 and MP5. However, a thermal stratification of about 4 K between the top and the bottom remains.

4.2.2 Helium pressure increase

The helium pressure increase inside the cryogenic vessel is shown in Figure 4.2(c) for MP7 and in Figure 4.2(d) for MP5. After about 2.5 s for MP7 and 3.5 s for MP5 in phase I, the boundary of the two-phase region close to the critical pressure p_{Crit} of helium is reached, resulting in changing slopes of both pressure curves. When the safety relief valve starts to open, a first peak in the helium pressure increase is observed after about 6.4 s for MP7 and 5.4 s for MP5. For MP7, the safety relief valve has been set to $p_{\mathrm{set}} = 6\,\mathrm{bar(g)}$ at ITEP and for MP5 to $p_{\mathrm{set}} = 2\,\mathrm{bar(g)}$ by the manufacturer, in both cases using the method IAD. According to the applicable standards [17, 19, 22], the safety relief valve must open completely within $p_{\mathrm{set}} + 10\,\%$, i.e. at $p \leq 6.6\,\mathrm{bar(g)}$ for MP7 and $p \leq 2.2\,\mathrm{bar(g)}$ for MP5 and even within $p_{\mathrm{set}} + 5\,\%$ according to the manufacturer. During MP7, the safety relief valve first opens at $p_{\mathrm{open}} = 6.8\,\mathrm{bar(g)}$, which is slightly above the tolerance as can also be seen in the zoom into the dataset shown in Figure 4.3(a). However, the safety relief valve in MP5 first opens at $p_{\mathrm{set}}+20\,\%$, which is considerably higher than required by the standards [17, 19, 22]. Although the

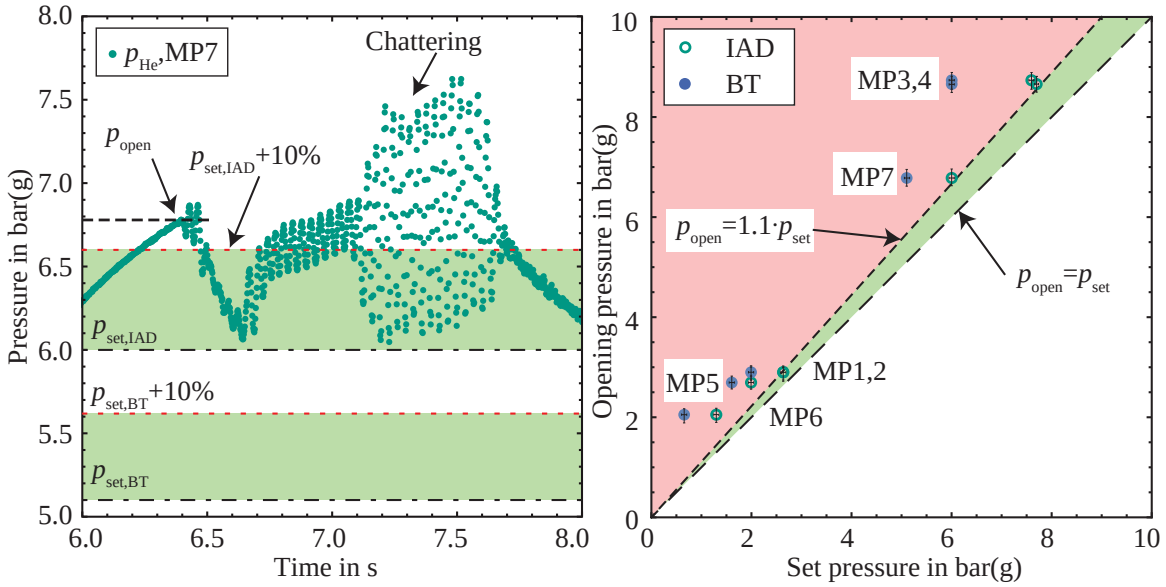

Figure 4.3: (a) Zoom into helium pressure increase of MP7, and (b) comparison between the opening pressure measured under experimental conditions and the set pressure measured at first bubble (BT) and first audible discharge (IAD) at a test rag.

absolute overpressures with regard to the set pressure do not differ much, the percentage of the pressure difference in MP5 conducted with a lower set pressure is higher than in MP7 with a higher set pressure.

In phase II, the safety relief valve opens and closes unstably after the first opening, resulting in very fast pressure changes in all conducted experiments. During this chattering of the safety relief valve, the pressure increases up to $p_{set} + 27\,\%$ in MP7 as shown in Figure 4.2(c) and Figure 4.3(a) and even up to $p_{set} + 50\,\%$ in MP5 as shown in Figure 4.2(d). Since the bursting pressure of the rupture disk as ultimate pressure protection level is set to $p_S = 16\,\text{bar(g)}$, this overpressure is without consequence for the PICARD test facility. However, such overpressures may trigger the bursting of a rupture disk in a staged cryostat pressure protection system, if the margin between the set pressures is too small [27]. Consequences could be large helium losses and the possible contamination of the open cryostat with humidity from the ambient air entering the system [27]. Therefore, a recommended margin value is 30 % to fulfil the tolerances of $\{+10\,\%, -15\,\%\}$ for the safety relief valve and $\pm 10\,\%$ for the rupture disk [14, 29]. For systems without an additional pressure protection level, such overpressures could lead to plastic deformation or even mechanical failure of the cryostat [27]. Because of the likelihood of chattering due to over-sized safety relief valves, special attention needs to be given not only to worst-case incidents, but also to incidents with lower heat fluxes than those assumed for the sizing of the safety relief valve [27].

While the helium pressure decreases during stable discharge in phase III of MP7, the helium pressure in MP5 increases with time until it decreases again after about 13 s.

Table 4.1: Average helium pressure increase during venting experiments at PICARD in comparison to literature data.

Type of event	Reference	$\mathrm{d}p/\mathrm{d}\tau$ bar/s
Minor LIV	This work, MP1	≈ 0.34
	This work, MP2	≈ 0.42
	This work, MP5	≈ 0.48
	This work, MP6	≈ 0.40
	Cavallari et al. [24] test 3	$\approx 0.8 \ldots 2.5$
Medium LIV	This work, MP3	≈ 1.1
	This work, MP4	≈ 1.1
	Harrison [25]	≈ 0.7
Major LIV	This work, MP7	≈ 1.1
	Cavallari et al. [24] test 4	≈ 8

An explanation for this could again be the design of the test facility: Because the safety relief valve in PICARD is mounted high above the cryostat at ambient temperature, it is not in contact with cold helium before the initial opening [27]. During helium discharge, the safety relief valve cools down, resulting in an increased stiffness of the spring, which may explain the further pressure increase during discharge in MP5 [27]. Another explanation is the occurrence of two-phase flow, which reduces the discharge capacity of safety relief devices [14,29] and occurs more likely at lower opening pressures close to the critical point of helium. For another two measuring points MP1 and MP2, the discussion of the temperature and pressure increase can be found in [27].

The comparison between p_{open} measured during the experiments MP1 to MP7 and p_{set} according to BT and IAD measured at the test rig is shown in Figure 4.3(b). For $p_{\mathrm{open}} = p_{\mathrm{set}}$, all data points would be on the diagonal line. The tolerated pressure range according to [17,19,22] for full lift safety relief valves of $p_{\mathrm{set}} \leq p_{\mathrm{open}} < 1.1 \cdot p_{\mathrm{set}}$ is indicated by the green area in Figure 4.3(b). However, the opening pressure exceeds the set pressure by up to 26 % in case of IAD, corresponding to the manufacturer method of this particular valve. In case of BT, the deviations would be as large as 209 % with larger deviations at lower set pressures. The reasons for the higher opening pressures could not be fully investigated in the course of this work, but might be associated with the pressure increase rate. For instance, ISO 4126-10 [31] restricts the maximum rate of pressure rise to $\mathrm{d}p/\mathrm{d}\tau = 12\,\mathrm{bar/min} = 0.2\,\mathrm{bar/s}$, while the pressure increases much faster during the experiments with $\mathrm{d}p/\mathrm{d}\tau \approx 0.3 \ldots 1.1\,\mathrm{bar/s}$ as listed in Table 4.1. As expected, the pressure increases faster during major LIV than during minor LIV, which is also confirmed by literature data [24, 25]. Possible other causes such as the influence of the fluid on the opening characteristics of the safety relief valve should also be further investigated. The larger differences in case of BT at lower set pressures can be explained by the smaller spring force pressing the disk on the seat of the safety

relief valve, causing detectable leaks long before the actual valve lift.

4.3 Wall temperature increase

The temperature increase at the cryogenic vessel wall over time with the corresponding measurement uncertainties for the first 15 s from the start of the venting process during major LIV (MP7) and minor LIV (MP5) is shown in Figure 4.4 (*a*) and (*b*). For both experiments, the temperatures at the top and the bottom of the cryogenic vessel (measured with TI21 and TI24) are higher than those measured at the sides (TI22 and TI23). This can be explained by the design of the radiation shield with large openings only at the top and the bottom: During venting, the warm gas first comes into contact with the cold surface at the top and bottom of the cryogenic vessel where the heat is transferred to the cryogenic vessel wall upon desublimation.

During major LIV, the temperature at all locations at the surface of the cryogenic vessel increases at first fast, later more slowly to about 70 . . . 80 K within the first 15 s from the start of the experiment after a short delay of about 0.5 s as shown in Figure 4.4 (*a*). The temperature at the top measured with TI21 first reaches the triple point of nitrogen at 63 K after 3.5 s. About 6 s later, the temperature measured at the middle (TI22) reaches 63 K and it can thus be assumed that from this moment the whole surface of the cryogenic vessel is covered with liquid and condensation instead of desublimation takes place. After about 14 s, the temperature at the top of the cryogenic vessel exceeds the saturation temperature of nitrogen and the venting fluid starts to evaporate again.

During minor LIV, the wall temperature increases more slowly than during major LIV as shown in Figure 4.4 (*b*), and the triple point of nitrogen is not reached during the first 15 s of the experiment.

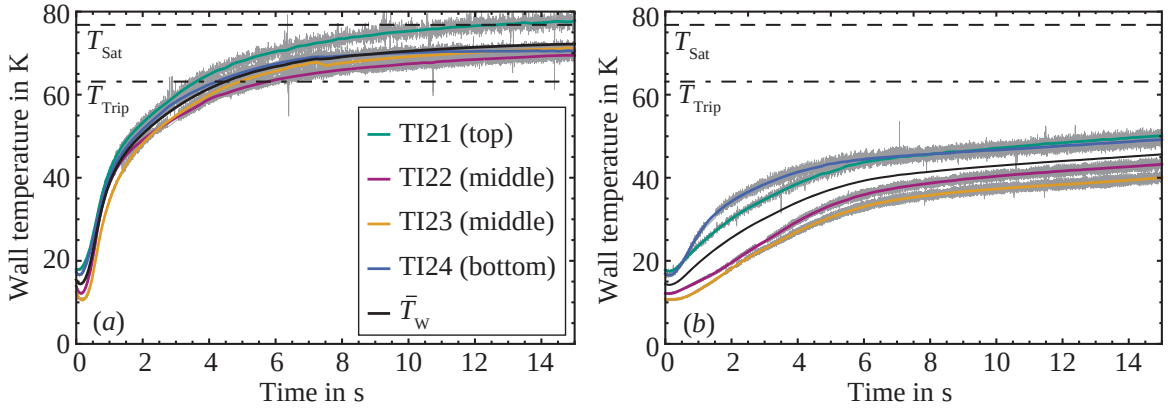

Figure 4.4: Wall temperatures TI21, TI22, TI23, TI24 and the resulting average wall temperature at the surface of the cryogenic vessel during the first 15 s of (a) major LIV (MP7) and (b) minor LIV (MP5).

4.4 Heat flux and discharge mass flow rate

Figure 4.5(a,b) shows the heat flux $\dot{q}_{\mathrm{Dep}}$ caused by deposition of the venting fluid again exemplary for major (MP7) and minor LIV (MP5). The deposition process starts once the first gas molecules come into contact with the surface of the cryogenic vessel. Therefore, $\dot{q}_{\mathrm{Dep}}$ would physically start from zero at $\tau = 0\,\mathrm{s}$, but is calculated to higher values from measurement data. This deviation can be explained by the response time of the sensors, especially of the pressure transmitters used for calculating the venting mass flow rate. Therefore, the calculated heat flux for $\tau \leq 0.2\,\mathrm{s}$ is not taken into consideration for the discussion of the results.

For major LIV shown in Figure 4.5(a), the heat flux reaches its maximum of about $5.7\,\mathrm{W/cm^2}$ after 0.5 s from the start of the experiment, which is considerably higher than the maximum heat flux of $3.1 \ldots 4.0\,\mathrm{W/cm^2}$ [23–25] commonly used for the sizing of safety relief devices. However, in more recent publications [37, 39], $\dot{q}_{\mathrm{Dep,max}} = 6\,\mathrm{W/cm^2}$ has been observed, which corresponds well with the peak heat flux measured in MP7. From $0.5 \ldots 4\,\mathrm{s}$, the heat flux decreases to a minimum of about $1.1\,\mathrm{W/cm^2}$. From $4\,\mathrm{s} \ldots 6\,\mathrm{s}$, $\dot{q}_{\mathrm{Dep}}$ increases again. During this time, the temperatures measured at the surface of the cryogenic vessel reach $T_{\mathrm{Trip,N2}} = 63\,\mathrm{K}$ as shown in Figure 4.5(a). At wall temperatures $T_{\mathrm{Trip}} < T_{\mathrm{W}} < T_{\mathrm{Crit}}$, the venting fluid condenses instead of freezes at the cold surface of the cryogenic vessel, resulting in a heat flux of about constantly $1.75\,\mathrm{W/cm^2}$, before the heat flux slowly starts to decrease after 10 s from the start of the venting process.

The discharge mass flow rate $\dot{m}_{\mathrm{Out}}$ during MP7 is shown in Figure 4.5(c). The first value above zero is measured after 6.6 s, which corresponds well with the opening pressure shown in Figure 4.2(c) and Figure 4.3(a). Consequently, the peak heat flux occurs long before the first opening of the safety relief valve and is therefore *irrelevant* for the sizing of safety relief valves. For instance in MP7, the helium pressure at the time when the maximum heat flux occurs is 0.2 bar(g), which is far from set pressures

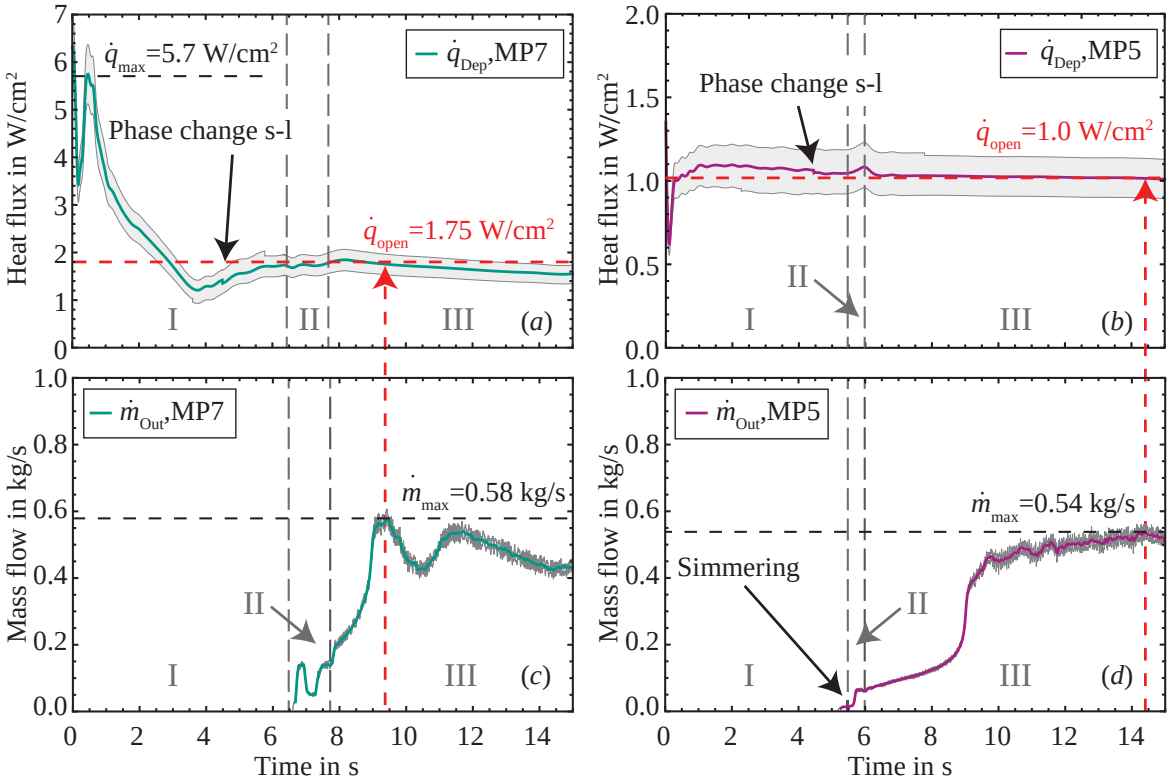

Figure 4.5: (a,b) Heat flux and (c,d) helium discharge mass flow rate after start of the venting process for the first 15 s during major LIV (MP7) and minor LIV (MP5).

in typical liquid helium applications.

During unstable operation of the safety relief valve in phase II, the measured discharge mass flow rate is small, which confirms the expected reduced discharge capacity due to chattering and pumping. In phase III, the measured helium discharge mass flow rate increases to a maximum of 0.58 kg/s after 9.5 s. At this time, the heat flux shown in Figure 4.5(a) has already decreased to 1.75 W/cm^2, which is considerably lower than the peak heat flux of 5.7 W/cm^2 and the constant design heat flux of 4 W/cm^2 used for the valve sizing. Consequently, the time-dependence of the processes is more important than the peak heat flux. The only impact of the maximum heat flux for high set pressures seems to be on the rate of the helium pressure increase as shown in Figure 4.2.

The expected discharge mass flow rate and resulting required discharge diameter of a safety relief valve following the established design steps from [17, 21] explained in Section 2.3 for three exemplary heat fluxes is shown in Table 4.2: With a typical heat flux of 4.0 W/cm^2 [24], the discharge mass flow rate is calculated to 1.6 kg/s following ISO 21013-3 [21], which results in a required discharge diameter of 22.2 mm with the settings of MP7. Based on this calculation, a safety relief valve diameter of $d_0 = 23$ mm (DN25) has been chosen for MP7. However, with the much smaller heat flux at the time when the maximum discharge mass flow rate is measured in MP7,

Table 4.2: Exemplary calculation of the discharge mass flow rate $\dot{m}_{\mathrm{Out}}$ according to ISO 21013-3 [21] and discharge diameter d_0 of a safety relief valve according to ISO 4126-1 [17] for the set conditions in MP7 based on different heat fluxes.

Input	$\dot{m}_{\mathrm{Out}}$ in kg/s	d_0 in mm
$\dot{q}_{\mathrm{Cavallari}} = 4\,\mathrm{W/cm^2}$ [24]	1.6	22.2
$\dot{q}_{\mathrm{Dep,MP7,max}} = 5.7\,\mathrm{W/cm^2}$	2.3	26.5
$\dot{q}_{\mathrm{Dep,MP7,open}} = 1.75\,\mathrm{W/cm^2}$	0.7	14.7

the predicted discharge mass flow rate is only 0.7 kg/s. This corresponds well with the measured maximum discharge mass flow rate of 0.58 kg/s. This smaller calculated discharge mass flow rate would require a smaller safety relief valve diameter of only 14.7 mm. Compared to the established method using a constant heat flux from [24], this corresponds to less than half the required discharge area when the time-dependence is taken into account! Thus, it can be concluded that the process dynamics has a large impact on the sizing of the safety relief valves for liquid helium application.

The heat flux measured during minor LIV is shown in Figure 4.5(b). Compared to an event of major LIV, the heat flux increases to a much lower peak value of 1.1 W/cm^2 in phase I and remains almost constant at 1 W/cm^2 before it very slowly decreases further. The measured heat flux corresponds well with the heat flux of 1 W/cm^2 measured by Cavallari et al. [24] for a minor LIV in their test 3. This stagnation of the heat flux has been observed during all minor LIV experiments at PICARD.

The discharge mass flow rate during the first 15 s of MP5 is shown in Figure 4.5(d). Unlike during major LIV, a small discharge mass flow rate of about 0.03 kg/s is detected already in phase I, i.e. before the first peak in the helium pressure (Figure 4.2(d)). This leakage of a small mass flow rate from the safety relief valve is called simmering. In phase II, the discharge mass flow rate increases to about 0.06 kg/s. Between 6 ... 9 s from the start of the venting experiment in phase III, the discharge mass flow rate increases to about 0.2 kg/s almost proportionally with time, which corresponds to the opening characteristic of proportional rather than full-lift safety relief valves [14]. Full-lift valves, however, also have a small proportional range, which might indicate that the valve did not fully open. The associated discharge mass flow rate could also explain the further helium pressure increase inside the cryogenic vessel in phase III displayed in Figure 4.2(d). Only after 9 s, the discharge mass flow rate strongly increases to about 0.5 kg/s, which indicates the typical *pop-up* to the full lift [14]. The peak discharge mass flow rate of 0.54 kg/s is measured after 14 s, before it decreases again. Besides the reduced discharge capacity before *pop-up*, the cool-down of the safety relief valve during simmering with a resulting increase in the stiffness of the spring could explain the considerable overpressure inside the cryogenic vessel observed for low opening pressures as exemplary shown in Figure 4.2(d). Following ISO 21013-3 [21] and ISO 4126 [17] with the heat flux of 1.0 W/cm^2 and the pressure of $p = 2.8$ bar(g) both measured at

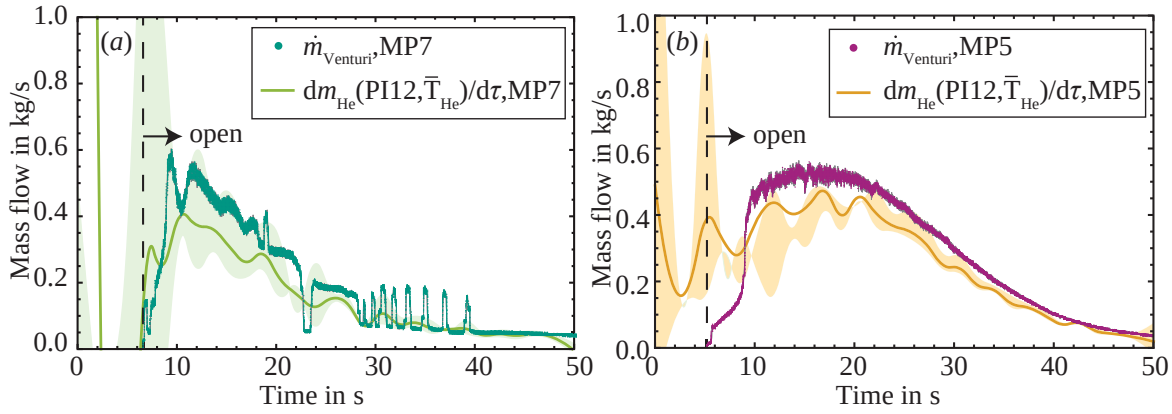

Figure 4.6: Discharge mass flow rate measured with the Venturi tube and calculated from the change of mass inside the cryogenic vessel during the first 50 s of (*a*) major LIV (MP7) and (*b*) minor LIV (MP5). The combined measurement uncertainties for the change of mass are displayed in lighter colour and for the Venturi tube measurement in grey.

the time when the maximum discharge mass flow rate occurs, the predicted discharge mass flow rate is calculated to 0.6 kg/s, which again corresponds well with the measured maximum discharge mass flow rate of 0.54 kg/s.

In Figure 4.6, the venting mass flow rate measured with the Venturi tube (displayed in darker green for MP7 and in purple for MP5) is compared to the venting mass flow rate calculated from the change in helium mass inside the cryogenic vessel (shown in light green for MP7 and in orange for MP5) as explained in Section 3.6 for the first 50 s from the start of the venting process. As can be seen in Figure 4.2, both the helium temperature and pressure data are subject to considerable fluctuations and inhomogeneity. In order to facilitate an evaluation of the change in helium mass over time, calculating a moving average of as many as 850 data points was found necessary, which results in only a rough estimation of the discharge mass flow rate following this method. Therefore, this method is considered less reliable than the Venturi tube measurement and only serves as a plausibility check. Both for MP7 and MP5, the curves of the change of helium mass with respect to time before the opening of the safety relief valve should be zero and are falsified by the *Runge Phenomenon*, i.e. the oscillation at the edges of equidistant polynomial interpolation functions of high degree when the number of interpolation points is large [68]. The oscillations towards $\tau = 50$ s have been reduced by interpolating the dataset for a longer period and displaying only the first 50 s of interest. As can be seen in Figure 4.6, the results of the mass flow rate calculated with the highly smoothed change of mass inside the cryogenic vessel and of the Venturi tube measurement correspond well concerning the general shape. The change of mass, however, yields smaller discharge mass flow rates for MP7 and MP5, which could be caused by using average helium temperature values. For both methods, the peak discharge mass flow rates are reached within the first 15 s of the experiments.

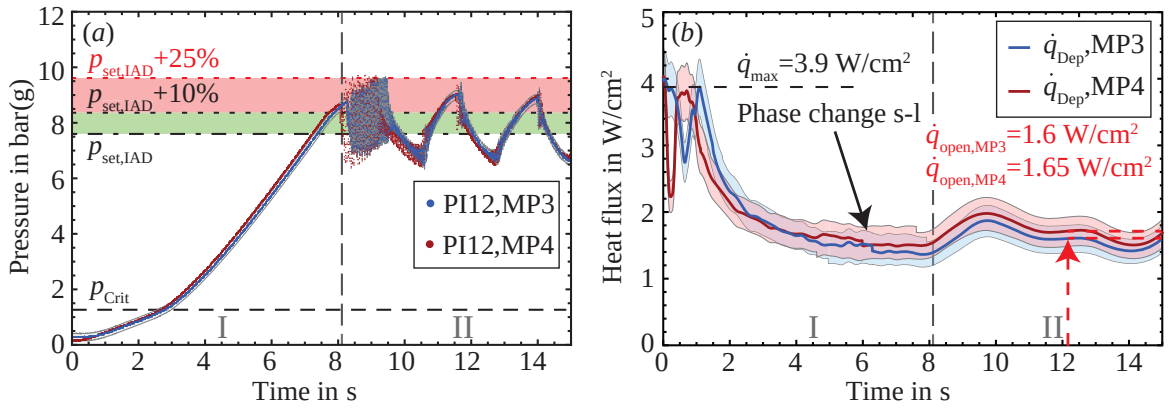

Figure 4.7: (a) Helium pressure increase in the PICARD cryogenic vessel over time after start of the venting process for a medium LIV (MP3 and MP4), (b) heat flux calculated for MP3 and MP4 from the datasets.

4.5 Reproducibility

In order to investigate the reproducibility of the venting experiments, the experiment MP3, where a medium sized orifice with $d_{Or} = 25\,\text{mm}$ is used, is repeated in MP4 with the same high set pressure of $p_{set} = 7.6\,\text{bar(g)}$ and a sampling rate of 500 Hz. As the only difference in the setup of these medium LIV events, the Venturi tube upstream of the safety relief valve is replaced in MP4 by a regular tube to investigate the influence of the pressure losses on the operation of the safety relief valve. The first 15 s of the pressure increase during MP3 and MP4 are shown in Figure 4.7(a). Same as discussed for minor and major LIV, the safety relief valve is closed in phase I. Directly after the first opening, chattering is observed and the safety relief valve opens and closes more than 40 times during less than 1.5 s in phase II of both MP3 and MP4. A reason for the more violent chattering with overpressures of up to $p_{set} + 26\,\%$ during MP3 and MP4 compared to MP7 and MP5 could be the large over-sizing of the safety relief valve by about 20 %, if common design rules [17, 19, 22, 23] are considered.

The heat flux during the first 15 s of MP3 and MP4 with the corresponding measurement uncertainties in lighter colours is shown in Figure 4.7(b). The slope of the heat flux is very similar to MP7 shown in Figure 4.5(a), except for the lower peak in the beginning: During both medium LIV experiments, the heat flux rises to about $3.9\,\text{W/cm}^2$ before it decreases to below $2\,\text{W/cm}^2$ by the time when the safety relief valve first opens. As the Venturi tube has been replaced by a normal tube in MP4, no discharge mass flow rate could be measured. After about 12.2 s when a maximum discharge mass flow rate is measured during MP3, the heat flux has sunk to $1.6\,\text{W/cm}^2$ in MP3 and $1.65\,\text{W/cm}^2$ in MP4. The almost identical curves of the pressure increase shown in Figure 4.7(a) and the very similar curves for the heat flux shown in Figure 4.7(b) prove the reproducibility of the experiments at PICARD. Furthermore, the congruence of the curves excludes the Venturi tube pressure drop as possible cause for the chattering of the safety relief valve.

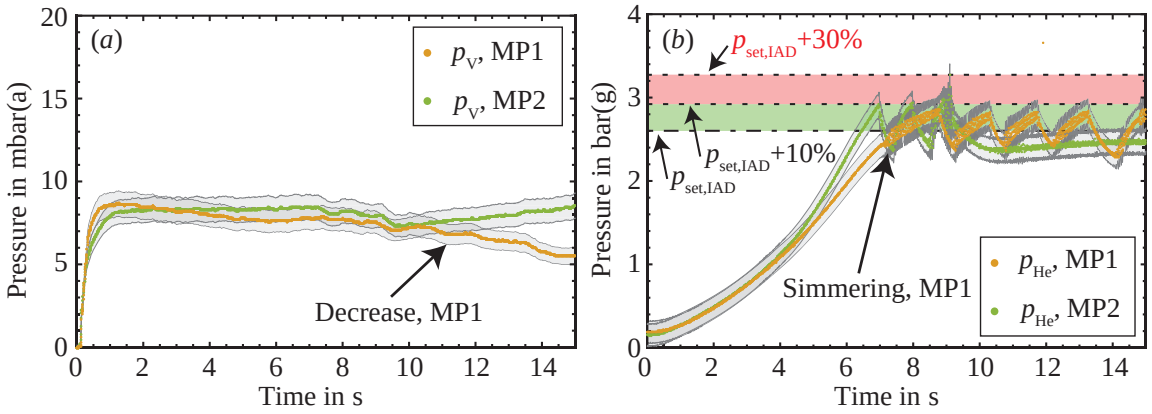

Figure 4.8: (a) Vacuum pressure increase and (b) helium pressure increase over time after start of the venting process for minor LIV (MP1 and MP2). In MP1, the insulating vacuum was vented with gaseous nitrogen from the buffer vessel and in MP2 with atmospheric air.

For the investigation of the venting fluid's influence on the process dynamics, the vacuum and helium pressure increase of the two minor LIV experiments MP1 and MP2 are shown in Figure 4.8. In MP1, the insulating vacuum is vented with gaseous nitrogen from the buffer vessel, while atmospheric air is directly used in MP2. For the experimental conditions listed in Table 3.4, the safety relief valve of size DN25 is also over-sized by about 27 %, if common design rules [17, 19, 22] and a heat flux of 1.25 W/cm^2 based on model calculations are considered [27]. The inlet pressure drop is conservatively estimated to 4.7 % [27].

As can be seen in Figure 4.8(a), the vacuum pressure in both experiments increases almost instantly to about 8 mbar(a). While the vacuum pressure in MP1 starts to slowly decrease after 10 s, the vacuum pressure in MP2 remains constant, same as in MP5 shown in Figure 4.1. The decreasing vacuum pressure in MP1 is caused by the limited capacity of the buffer vessel: In order to protect the rupture disks of the vacuum vessel set to only 0.5 bar(g), gaseous nitrogen is supplied in the buffer vessel with an overpressure of 1 bar(g). Although gaseous nitrogen is refilled to the buffer vessel through a small tube during venting, the cryopumping capacity of the cryogenic vessel is more effective than expected, and not enough gaseous nitrogen is refilled to the buffer vessel, where the pressure stagnates at about 300 mbar(a) [27]. As a result, the venting mass flow rate in MP1 decreases with decreasing buffer pressure. With $\dot{m}_{In} < \dot{m}_{Dep}$, the vacuum pressure in MP1 decreases.

The resulting helium pressure increase during MP1 and MP2 is shown in Figure 4.8(b). For the first 5 s of the experiment, the helium pressure increases almost identically in MP1 and MP2, before the pressure increase in MP1 slows down compared to MP2, which is a direct consequence of the smaller heat flux caused by less venting fluid desublimating at the cold surface of the cryogenic vessel. Same as in MP5, the safety relief valve in MP1 starts to simmer, while the safety relief valve in MP2 remains closed until the first peak in helium pressure after 7 s from the start

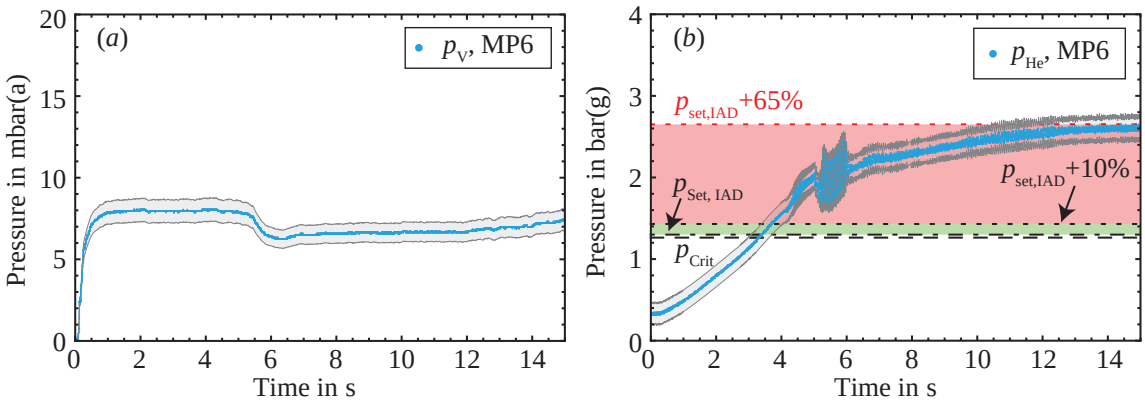

Figure 4.9: (a) Vacuum pressure and (b) helium pressure over time during minor LIV with the set pressure of the safety relief valve close to the critical point (MP6).

of the experiment. An explanation for this could be the smaller rate of pressure rise in MP1 compared to MP2 and MP5 as can be seen in Table 4.1 in Subsection 4.2.2. Because of the smaller deposition rate, the safety relief valve pumps for a longer period during unstable operation in MP1 than in MP2 and overpressures of up to 30 % of p_{set} are reached in MP1 after about 20 s [27]. However, the almost identical vacuum and helium pressure increase during the first seconds of MP1 and MP2 give confidence in the usage of nitrogen as venting fluid for future experiments with MLI, if the nitrogen refill to the buffer vessel can be optimized. The advantage would be to avoid humidity entering the vacuum space, which is especially difficult when several layers of MLI are wrapped around the cryogenic vessel.

In order to investigate the influence of low set pressures on the evolution of the processes during minor LIV, the experiment MP6 has been conducted with $p_{set,IAD} = 1.3\,\text{barg(g)}$, which is close to the critical point of helium. Unlike during MP1, MP2 and MP5 discussed before, the vacuum pressure during MP6 shown in Figure 4.9(a) decreases after about 6 s before it slowly increases again, which indicates a very high cryopumping capacity of the cold surface. However, the difference to the vacuum pressure increase during the other minor LIV events shown in Figure 4.1 and Figure 4.8 is small. The helium pressure during the first 15 s of the venting experiment in MP6 is shown in Figure 4.9(b). Despite the low set pressure, the first peak of the helium pressure is reached at $p_{open} = 2\,\text{bar(g)}$, which is considerably higher than the set pressure. After the first peak, chattering of the safety relief valve is observed for about 2 s. Same as for MP5 (shown in Figure 4.2(d)), the helium pressure continues to increase, reaching an overpressure of even $p_{set,IAD} + 65\,\%$. Again, this could be caused by the reduced discharge capacity because of two-phase flow and by the increased stiffness of the spring inside the safety relief valve at cryogenic temperatures.

The heat flux and discharge mass flow rate during MP5 and MP6 are shown in Figure 4.10. The almost identical heat flux curves displayed in Figure 4.10(a) underline again the reproducibility of the experiments. Same as the heat fluxes, the discharge

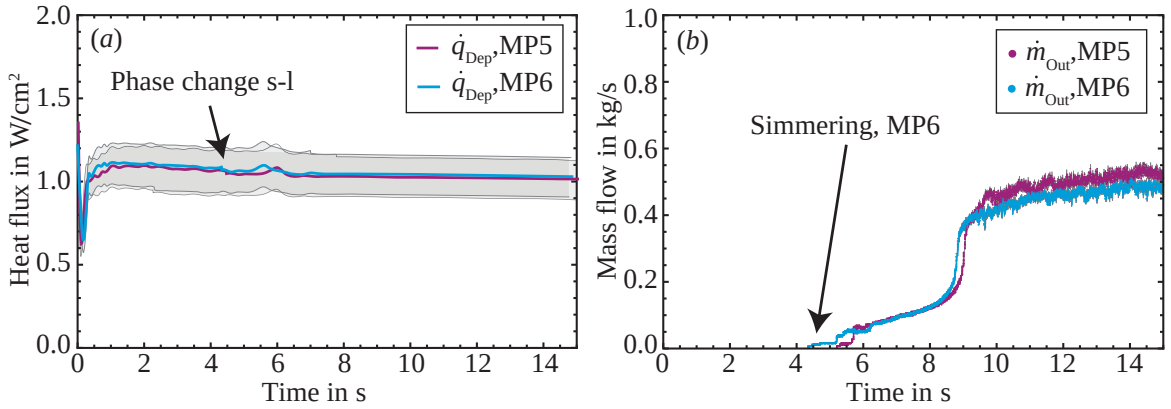

Figure 4.10: Comparison between (*a*) the heat fluxes and (*b*) the discharge mass flow rates measured during minor LIV exemplary for MP5 with $p_{set} = 2\,\text{bar(g)}$ and MP6 with $p_{set} = 1.3\,\text{bar(g)}$.

mass flow rates measured during MP5 and MP6 shown in Figure 4.10(*b*) have very similar shapes, although the simmering in MP6 starts earlier as a consequence of the lower set pressure. In MP6, the safety relief valve operates for almost 5 s with reduced discharge capacity, which could also explain the large overpressure with regard to the set pressure shown in Figure 4.9(*b*). This first comparison between the experimental results of MP6 and MP5 indicates that the set pressure has no strong influence on the heat flux and discharge during minor LIV. However, more experiments are required for definite conclusions.

4.6 Conclusions

The applicable standards [17,19,22] do not explicitly define the conditions for adjusting the set pressure of safety relief valves. A comparison between the set pressure according to the methods "initial audible discharge" (IAD) and "bubble test" (BT) with the opening pressure under experimental conditions showed large differences especially for BT. During all experiments conducted in the frame of this work, the opening pressure of the safety relief valve exceeded the allowed $p_{set,IAD} + 10\,\%$ especially for low set pressures, which could be caused by the much faster pressure increase compared to the setting procedure. Further investigation of the setting procedure will be required in order to guarantee the opening of the safety relief valve within the tolerance.

Especially during experiments with a low initial filling level, large stratification of the helium temperature inside the cryogenic vessel was observed, while the horizontal gradients seem negligible. Chattering of the safety relief valve occurred during all experiments, independently of the pressure increase rate and the set pressure. During this unstable operation, overpressures of $25 \ldots 50\,\%$ with regard to $p_{set,IAD}$ were observed. Similar observations were made during experiments at CERN [69]. Causes for the unstable operation of the safety relief valve could be over-sizing, especially for experiments with larger venting orifices and higher set pressures. For experiments with lower

set pressures, pressure losses upstream can be the reason for chattering and pumping of the safety relief valve. However, unstable operation can occur whenever an incident happens that is smaller than the worst-case scenario for which the safety relief valve was sized. Therefore, measures to avoid chattering or alternatives to spring-loaded safety relief valves need to be investigated in future. Possibilities could be the additional use of control valves or to mechanically keep the safety relief valve open for some seconds after the first opening, e.g. with a magnet holding the spindle of the safety relief valve. Another measure against chattering could be lower reseating pressures of safety relief valves. This would allow the inlet pressure to decrease without the safety relief valve closing too early. A reduction of the pressure losses at the inlet of the safety relief valve would be beneficial. However, this is not always possible in cryogenic applications due to the necessity of reducing the heat input to the cryostat.

The results of medium LIV could be reproduced well. The use of the Venturi tube upstream of the safety relief valve has no influence on the valve behaviour for higher set pressures, but should also be verified for lower set pressures. The comparison between different venting fluids showed that gaseous nitrogen from a buffer vessel can be used to replace atmospheric air in experiments with MLI, if enough nitrogen can be supplied in the buffer throughout the experiment.

In order to accommodate larger tolerances in the opening pressures, it is advantageous to operate safety relief valves at higher pressures. A prudent safety relief valve concept involves set pressures well below the design pressure of the cryostat. Besides, a margin of $\geq 30\,\%$ between the set pressure of the safety relief valve and the bursting pressure of a rupture disk as ultimate safety relief level is recommended to cope with overpressures during discharge. However, this might not always be possible due to other design constraints.

For minor LIV, the heat flux did not exceed $1.2\,\mathrm{W/cm^2}$ and remained nearly constant until it decreased long after the first opening of the safety relief valve, thus showing little time-dependence. For major LIV, a peak heat flux of up to almost $6\,\mathrm{W/cm^2}$ was measured, which is higher than the established values of $3.1 \ldots 4\,\mathrm{W/cm^2}$ measured in [23–25] but lower than the maximum heat flux of $40\,\mathrm{W/cm^2}$ calculated in [38] and comparable to values of $4.5 \ldots 6\,\mathrm{W/cm^2}$measured in [37,39]. During major and medium LIV, the heat flux quickly decreased after the first peak to considerably lower values in the range of $1.6 \ldots 1.75\,\mathrm{W/cm^2}$. This corresponds well with both the shape and the absolute values of the heat flux derived from the change of helium properties in [37]. The shape of the heat flux corresponds also well with [35, 38]. Consequently, the results of the venting experiments conducted in the course of this work indicate that the necessary discharge area of safety relief valves set to higher pressures during major and medium LIV can considerably be reduced if the process dynamics is considered. Benefits are reduced acquisition costs, space requirements and helium leakage as well as a more reliable operation of safety relief devices. The results of the first set of venting experiments showed the significance of the cryogenic safety research possible at PICARD. However, more experiments are needed to confirm these findings.

CHAPTER 5

Refined modelling of the processes during loss of insulating vacuum

A simplified dynamic model linking all sub-processes occurring during the loss of insulating vacuum (LIV) in a liquid helium cryostat has been presented in Section 2.4. In this chapter, the refinement of the existing model, especially concerning the heat and mass transfer during desublimation and condensation of the venting fluid at the cold surface of the cryogenic vessel, is presented. Hence, the results of model calculations are compared to experimental and literature data.

5.1 Refinement of the dynamic model

5.1.1 Modelling the heat transfer resistance

For modelling the processes during LIV, the heat transfer between the air leaking in the vacuum space and the fluid in the cryogenic vessel plays an important role, which has not yet been completely analysed. A schematic temperature profile at a certain time during LIV in a liquid helium cryostat is shown in black in Figure 5.1. For the deposition of the venting fluid, the temperature T_{VDep} at the interface between the vacuum space and the layer of deposited venting fluid is of great importance. From heat transfer kinetics, T_{VDep} can be calculated as

$$\dot{Q} = \frac{1}{R_{\mathrm{tot}}} \cdot (T_{\mathrm{VDep}} - T_{\mathrm{Cr}}) \tag{5.1}$$

with the total thermal resistance R_{tot}

$$R_{\mathrm{tot}} = R_{\lambda\mathrm{Dep}} + R_{\lambda\mathrm{W}} + R_{\alpha\mathrm{WCr}}\,, \tag{5.2}$$

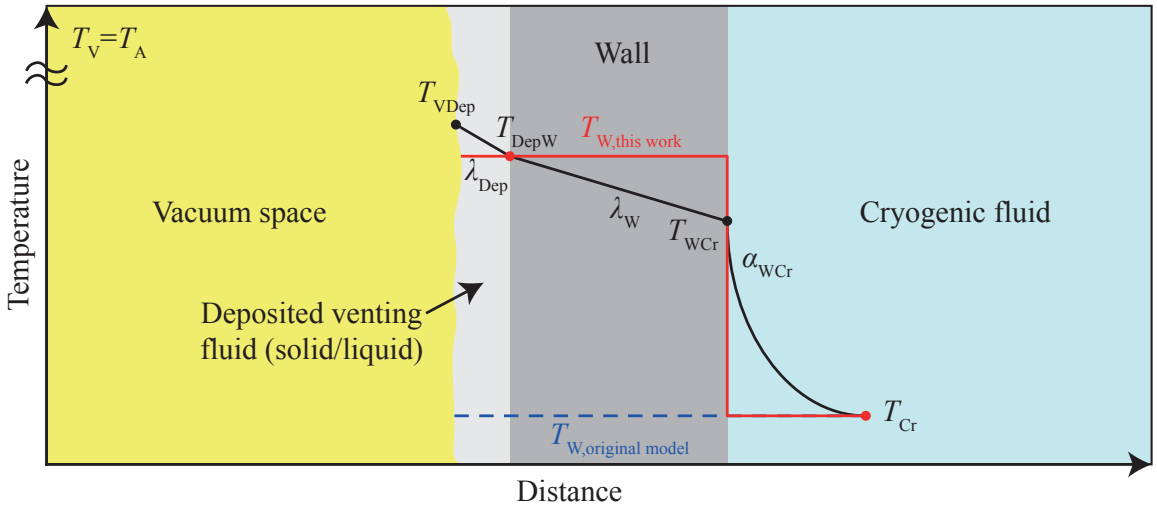

Figure 5.1: Schematic temperature profile between the vacuum space and the cryogenic fluid inside the cryogenic vessel with the heat transfer coefficient α and the thermal conductivity λ. In black, the theoretical temperature profile is shown, while the simplified temperature profiles for the original dynamic model and the refined dynamic model are highlighted in blue and red, respectively.

including the thermal resistances of the deposited venting fluid $R_{\lambda\mathrm{Dep}}$ and of the cryogenic vessel wall $R_{\lambda\mathrm{W}}$ as well as the convective resistance between the wall and the cryogenic fluid $R_{\alpha\mathrm{WCr}}$. Same as in [37], the convective heat transfer between the vacuum space and the deposited venting fluid is not considered, as the phase change of the venting fluid (gaseous-solid or gaseous-liquid) dominates the process. The thermal resistances can be calculated with the respective area A, layer thickness s, heat transfer coefficient α and thermal conductivity λ as

$$R_{\lambda\mathrm{Dep}} = \frac{s_{\mathrm{Dep}}}{\lambda_{\mathrm{Dep}} \cdot \bar{A}_{\mathrm{Dep}}}\,, \tag{5.3}$$

$$R_{\lambda\mathrm{W}} = \frac{s_{\mathrm{W}}}{\lambda_{\mathrm{W}} \cdot \bar{A}_{\mathrm{W}}}\,, \tag{5.4}$$

$$R_{\alpha\mathrm{WCr}} = \frac{1}{\alpha_{\mathrm{WCr}} \cdot A_{\mathrm{WCr}}}\,. \tag{5.5}$$

Literature data on the thermal conductivity of stainless steel and solid and liquid nitrogen can be found in Figure 5.2(a). For solid nitrogen, the thermal conductivity is much lower than for stainless steel, and even another magnitude lower for liquid nitrogen [13, 70, 71]. As shown in Chapter 4, however, large gradients in time occur during LIV, especially pressure gradients in the vacuum space and temperature gradients at the cryogenic vessel surface. These gradients imply:

- simultaneous processes such as diffusion, adsorption/desorption and vapour-

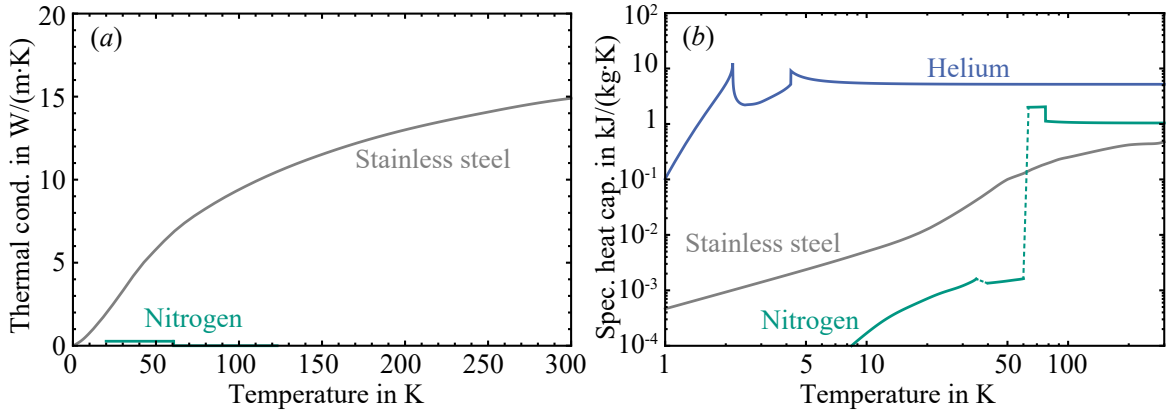

Figure 5.2: (a) Thermal conductivity λ of stainless steel [72] and solid and liquid nitrogen [13, 70, 71] and (b) specific heat capacity c_p of stainless steel [72], nitrogen [13, 71] and helium at 1 bar(a) [73].

liquid-solid phase change of the venting fluid,

- changing sticking coefficients of air molecules on the cold surface,
- changing density, heat conductivity and layer thickness of the deposited venting fluid,
- changing composition in case of deposited air,
- changing states of helium inside the cryogenic vessel from two-phase (including changing liquid level) to supercritical,
- temperature gradients in the helium.

In combination with partly lacking literature data on the fluid properties, these factors do not allow a purely analytical integration of the heat transfer during LIV in the model.

Due to the lack of temperature data for the dynamic processes, all thermal resistances between the vacuum space and the helium inside the cryogenic vessel have been neglected in the original dynamic model presented in Section 2.4. This first approach assumed $R_{\mathrm{tot,original\ model}} = 0\,\mathrm{K/W}$ and yielded a uniform temperature throughout all layers $T_{\mathrm{W,original\ model}} = T_{\mathrm{Cr}}$, which is shown in blue in Figure 5.1. This simple model actually considers equilibrium, i.e. a quasi-static energy transport, rather than a strongly dynamic process. Contrary to this assumption, the first experimental results show a considerable difference between the average temperature measured in the cryogenic fluid $\bar{T}_{\mathrm{Cr}}$ and the average wall temperature $\bar{T}_{\mathrm{W}}$ measured at the outer surface of the cryogenic vessel wall. This can be seen in Figure 5.3(a) exemplary for MP7: The temperature difference between $\bar{T}_{\mathrm{Cr}}$ and $\bar{T}_{\mathrm{W}}$ increases from 10 K to about 70 K within the first 15 s of the experiment. The thickness of the layer of solid venting fluid s_{Dep} can be estimated from the experimental results of the deposition mass flow rate $\dot{m}_{\mathrm{Dep}}$ with

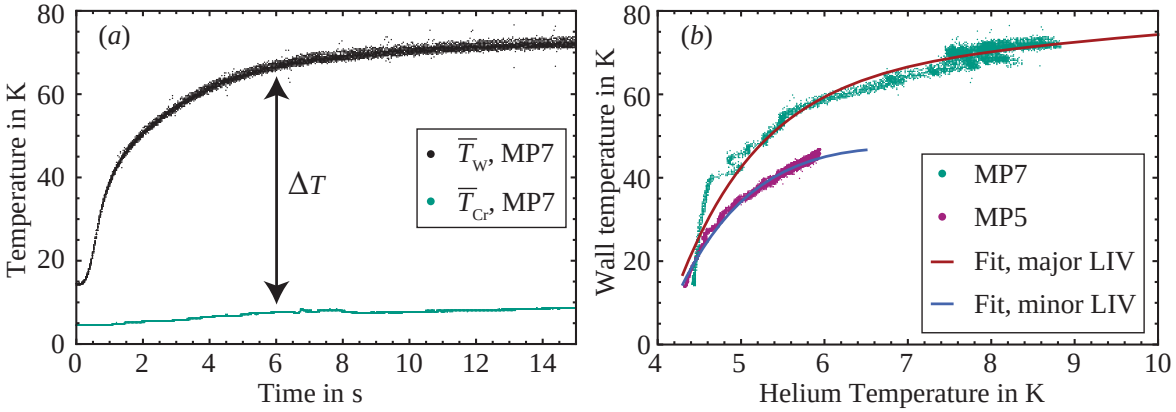

Figure 5.3: (a) Average measured wall temperature and helium temperature during the first 15 s of MP7 and (b) average measured wall temperature as a function of the average measured helium temperature for the first 15 s of MP7 and MP5 with the respective fit functions.

the density of solid nitrogen from [11] as approximation for the density of the venting fluid ρ_V as

$$s_{Dep}(\tau) = \frac{\int_0^\tau \dot{m}_{Dep}(\tau)\,\mathrm{d}\tau}{\rho_V} \cdot \frac{1}{A_{Cr}} \tag{5.6}$$

to a maximum thickness of well below 1 mm, which is small compared to the thickness of the cryogenic vessel wall of PICARD that varies between $s_W = 4\,\mathrm{mm}$ at the sides and $s_W = 5\,\mathrm{mm}$ at the top and bottom. Therefore, the temperature at the surface of the deposited venting fluid T_{VDep} is assumed to equal $\bar{T}_W$ as a first approach. The difference between $T_{VDep} = \bar{T}_W$ and $\bar{T}_{Cr}$ is a direct consequence of the total thermal resistance and is thus used for a refinement of the original model, as will be explained in the following: In order to eliminate the time dependence of the thermal resistance, the average wall temperature $\bar{T}_W$ is plotted over $\bar{T}_{Cr}$ for major (MP7) and minor LIV (MP5) in Figure 5.3(b). For both experiments, $\bar{T}_W$ increases continuously but non-linearly with $\bar{T}_{Cr}$. The two experiments, however, do not show the same behaviour because the difference between the wall temperature and the helium temperature increases more strongly during major LIV than during minor LIV. With the heat flux being calculated from measurement data including the wall temperature (cf. Eq. (2.15)) and considering the noise in the wall temperature data, a different approach for implementing the wall temperature in the model has been chosen in this work: Using a least-squares fit to the data in Figure 5.3 yields an empirical fit function for T_W for major LIV of

$$T_{W,\text{major LIV}}(T_{Cr}) = 59\,\mathrm{K} - 3603\,\mathrm{K} \cdot e^{-\frac{T_{Cr}}{\mathrm{K}}} + 1.55 \cdot T_{Cr}\,, \tag{5.7}$$

and for minor LIV of

$$T_{W,\text{minor LIV}}(T_{Cr}) = 70\,\mathrm{K} - 3192\,\mathrm{K} \cdot e^{-\frac{T_{Cr}}{\mathrm{K}}} - 2.85 \cdot T_{Cr} \tag{5.8}$$

plotted in red and blue in Figure 5.3(b). For medium LIV, the respective fit function will be discussed in Subsection 5.2.4. These empirical fit functions are hence implemented in Eq. (2.15) to refine the calculation of the heat load $\dot{Q}_{\mathrm{Dep}}$ caused by the deposition of the venting fluid as

$$\dot{Q}_{\mathrm{Dep}}(p_{\mathrm{V}}, T_{\mathrm{Cr}}) = \dot{m}_{\mathrm{Dep}}(p_{\mathrm{V}}, T_{\mathrm{W}}\,[T_{\mathrm{Cr}}]) \cdot [h_{\mathrm{V}}(p_{\mathrm{V}}) - h_{\mathrm{W}}(T_{\mathrm{W}}\,[T_{\mathrm{Cr}}])]\ , \tag{5.9}$$

thus including a simplified total thermal resistance. The resulting schematic temperature profile for the refined model is shown in red in Figure 5.1.

As a first step towards a future generalization of the model, having a single fit function for all venting diameters and cryostat designs would be beneficial. This could be achieved by normalizing the fit functions for $T_{\mathrm{W,minor\ LIV}}$, $T_{\mathrm{W,medium\ LIV}}$ and $T_{\mathrm{W,major\ LIV}}$ with a design factor that could be a function of the the cryogenic surface area, the venting diameter and/or the venting mass flow rate. Furthermore, the only difference in the thermal resistances at PICARD according to Eq. (5.2) that can cause the difference in the temperature profiles displayed in Figure 5.3 is the thermal resistance of the layer of deposited venting fluid, $R_{\lambda\mathrm{Dep}}$, if equal conditions in the helium (e.g. equal initial filling level) are assumed. This could indicate that the thermal resistance of the deposited venting fluid cannot be neglected despite the estimated maximum thickness of below 1 mm. Assuming equal composition, density etc. of the deposited venting fluid and thus equal thermal conductivity, the only difference in $R_{\lambda\mathrm{Dep}}$ between minor, medium and major LIV according to Eq. (5.3) is the layer thickness of the deposited venting fluid s_{Dep} calculated according to Eq. (5.6). Thus, a comparison between the experimental results for minor, medium and major LIV could make the determination of the thermal resistance of the deposited venting fluid possible. As a further refinement, the temperature gradients both over the surface and the thickness of the cryogenic vessel wall and within the layer of deposited venting fluid could be included in the model and investigated experimentally.

Based on the experimental results, the original dynamic model explained in Section 2.4 has been refined as shown schematically in the block diagram in Figure 5.4 in comparison to Figure 2.6. Besides the refinement concerning the heat transfer resistance (highlighted in orange in Figure 5.4), the changing temperature difference between T_{W} and T_{Cr} observed in Figure 5.3 is also included in the refined model (indicated in dark green in Figure 5.4) as will be explained in the following Subsection 5.1.2. Further refinements concerning the deposition of the venting fluid (highlighted in red in Figure 5.4) and the real flow conditions during venting (marked in light green in Figure 5.4) will be presented in Subsection 5.1.3 and in Subsection 5.1.4, respectively.

5.1.2 Modelling the temperature increase in the cryogenic vessel wall

In addition to the total thermal resistance, the heat capacity of the cryogenic vessel wall has been neglected in the original dynamic model presented in Section 2.4 by assuming the heat load caused by the deposition of the venting fluid on the cold cryogenic vessel wall, $\dot{Q}_{\mathrm{Dep}}$, is equal to the heat load transferred to the cryogenic fluid, $\dot{Q}_{\mathrm{Cr}}$.

Contrarily, the temperature difference between T_W and T_{Cr} changes during the experiments as can be seen in Figure 5.3, which indicates that $\dot{Q}_{Dep}$ calculated according to Eq. (5.9) at a wall temperature T_W is not in equilibrium with $\dot{Q}_{Cr}$. By applying the first law of thermodynamics, the temperature raise in the cryogenic vessel wall is included in the refined model as

$$\dot{Q}_{Cr}(p_V, T_W) = \dot{Q}_{Dep}(p_V, T_W) - c_W \cdot m_W \cdot \frac{dT_W(\tau)}{d\tau} \tag{5.10}$$

with the cryogenic vessel mass, m_W, the specific heat capacity of the cryogenic vessel wall, c_W, and the assumption of a homogeneous wall temperature, T_W as shown in dark green in Figure 5.4. The specific heat capacity of nitrogen in comparison to helium and stainless steel is shown in Figure 5.2(b) in Subsection 5.1.1. Due to the small mass of solid venting fluid and the low heat capacity compared to the cryogenic vessel wall made of stainless steel, the warming of the layer of frozen venting fluid is neglected in the refined model.

5.1.3 Modelling the mass transfer at the cryogenic vessel wall

In the original dynamic model presented in Section 2.4, the mass transfer at the cryogenic vessel wall is greatly simplified with one constant mass transfer coefficient for the desublimation with the density difference as driving force. However, the physical process mechanisms are much more complicated, since a combination of diffusion, adsorption/desorption, condensation/evaporation, desublimation/sublimation and freezing/melting takes place at the same time.

A more detailed approach based on kinetic theory that is often used in vacuum technology to describe cryopumping is chosen to refine the modelling of the mass transfer [74]: In the corresponding *Hertz-Knudsen equation*, both the influence of particles sticking to the cryogenic surface (in this context summarized as the condensation mass flux, I_C), and of the particles emitted from the deposited layer (in this context summarized as evaporation mass flux, I_E) are considered. Thus, the effective deposition mass flow rate $\dot{m}_{Dep}$ is calculated as

$$\dot{m}_{Dep} = A_{Cr} \cdot (I_C - I_E) \ . \tag{5.11}$$

The condensation mass flux directly depends on the pressure p_V and the temperature T_V of the gaseous venting fluid in the vacuum space, and on the condensation coefficient α_C as

$$I_C = \alpha_C \cdot \frac{p_V}{\sqrt{T_V}} \cdot \frac{1}{\sqrt{2\pi R_V}} \, . \tag{5.12}$$

The evaporation mass flux, on the other hand, depends on the conditions at the surface of the condensed layer as

$$I_E = \alpha_E \cdot \frac{p_{Sat}(T_W)}{\sqrt{T_W}} \cdot \frac{1}{\sqrt{2\pi R_V}} \, , \tag{5.13}$$

including the evaporation coefficient α_E and the saturation vapour pressure p_{Sat} of

the condensate, which is assumed to correspond to T_W as a result of the estimated maximum condensate layer thickness of below 1 mm as explained in Subsection 5.1.1.

The dimensionless condensation coefficient α_C is defined as the number of condensed particles to the number of incidents upon the cold surface [74]. It depends on the type of gas, the temperature of both the gas and the cold surface and on the supersaturation [74]. The evaporation coefficient α_E is a measure of how many particles escape from the cold surface into the gaseous phase and is, same as α_C, a function of different physical variables [74]. Both dimensionless coefficients α_C and α_E are defined in the range of $0 \leq \{\alpha_C, \alpha_E\} \leq 1$ [74, 75].

As a simplification, homogeneous conditions around the cryogenic vessel are assumed in this work. However, the transmission of the gas molecules through obstacles such as typically baffles or tubes cannot be neglected [74]. For instance, the transmission probability for molecules through tubes with circular cross-section is listed between $1 \ldots 11 \cdot 10^{-2}$, while the transmission probability for baffles is listed between $0 \ldots 50 \cdot 10^{-2}$ [74]. The gas molecules in the PICARD test facility need to pass from the venting orifice through the baffles at the radiation shield before reaching the cold surface of the cryogenic vessel. Therefore, the transmission coefficient α_T is additionally considered in the refined model, resulting in

$$\dot{m}_{\text{Dep,this work}} = A_{Cr} \cdot \alpha_T \cdot \left(\alpha_C \cdot \frac{p_V}{\sqrt{T_V}} - \alpha_E \cdot \frac{p_{Sat}(T_W)}{\sqrt{T_W}} \right) . \tag{5.14}$$

For the experimental setup at PICARD, the transmission coefficient is defined as

$$\alpha_T = 3 \cdot 10^{-2} \tag{5.15}$$

through comparison with literature values [74] and a parameter study as explained in Appendix B.1.

At equilibrium with $T_V = T_W$ and $p_V = p_{Sat}(T_W)$, the net evaporation/condensation rate is zero and consequently α_C equals α_E [74, 75]. For non-equilibrium, as is the case for the time of interest during LIV, $\alpha_C > \alpha_E$ is evident, which makes an experimental determination of α_C and α_E difficult [74, 75]. For instance, experimental results are often given only for an effective condensation coefficient $\alpha_{C,eff}$ [74, 75]. For simplicity, only the temperature-dependence of α_C and α_E is considered in this work, independently of the different experimental conditions such as minor/major LIV. The condensation coefficient α_C is also called the *sticking coefficient*. For low temperatures, $\alpha_C(T_W \approx 12\,\text{K}) = 0.99$ was measured in [60] for nitrogen sticking on solid nitrogen, while the effective condensation coefficient $\alpha_{C,eff,N2}(T_W \approx 20\,\text{K}) \approx 1$ was measured with the molecular beam method in [74, 76]. With the very high sticking probability of nitrogen molecules at wall temperatures of $T_W < 20\,\text{K}$, $\alpha_E = 0$ is assumed for $T_W < 20\,\text{K}$. Between $T_W = 20 \ldots 63\,\text{K}$, $\alpha_C(T_W)$ and $\alpha_E(T_W)$ are linearly interpolated between the constant values of the higher and lower temperature ranges. At temperatures above the triple point of the venting fluid, condensation instead of desublimation takes place at the cold surface. Due to a lack of literature data, α_C and α_E are set to constant values for $T_W \geq T_{Trip,N2} = 63\,\text{K}$. Typical condensation coefficients (l-g) for water measured in the range of $\alpha_C = 1 \cdot 10^{-2} \ldots 1$ and evaporation coefficients (g-l) of water in the range

of $\alpha_\mathrm{E} = 1 \cdot 10^{-3} \ldots 1$ can be found in [77]. This results in a piecewise definition of the condensation coefficient as

$$\alpha_\mathrm{C}(T_\mathrm{W}) = \begin{cases} 1 & T_\mathrm{W} \leq 20\,\mathrm{K} \\ -2.29 \cdot 10^{-2} \cdot T_\mathrm{W} + 1.46 & 20\,\mathrm{K} < T_\mathrm{W} \leq T_\mathrm{Trip,N2} \\ 1 \cdot 10^{-2} & T_\mathrm{W} > T_\mathrm{Trip,N2} \end{cases} \tag{5.16}$$

and the evaporation coefficient as

$$\alpha_\mathrm{E}(T_\mathrm{W}) = \begin{cases} 0 & T_\mathrm{W} \leq 20\,\mathrm{K} \\ 2.32 \cdot 10^{-5} \cdot T_\mathrm{W} - 4.63 \cdot 10^{-4} & 20\,\mathrm{K} < T_\mathrm{W} \leq T_\mathrm{Trip,N2} \\ 1 \cdot 10^{-3} & T_\mathrm{W} > T_\mathrm{Trip,N2}\,. \end{cases} \tag{5.17}$$

5.1.4 Modelling the venting section

Another simplification in the dynamic model presented in Section 2.4 is the assumption of an ideal nozzle through which the insulating vacuum is vented. However, friction and contraction also have to be considered for compressible flow [78, 79], especially for a non-standard orifice measurement section as used at the PICARD facility. Therefore, an additional flow rate coefficient K_Vent defined in analogy with the safety relief valve discharge coefficient (cf. Eq. (2.5)) as

$$K_\mathrm{Vent} = \frac{\dot{m}_\mathrm{In,measured}}{\dot{m}_\mathrm{In,ideal}} \tag{5.18}$$

is introduced with the measured venting mass flow rate $\dot{m}_\mathrm{In,measured}$ based on Eq. (3.3) and the ideal mass flow rate $\dot{m}_\mathrm{In,ideal}$ based on Eq. (2.13). Typical orifice flow rate coefficients are between $K_\mathrm{Vent} \approx 0.65 \ldots 0.95$, depending among others on the kind of orifice, the Reynolds number and the ratio between the tube and the orifice [78, 79]. In this work, K_Vent was calculated with the temperature and pressures from the experiments at $\tau = 0$ as input parameters to $K_\mathrm{Vent} = 0.85 \pm 10\,\%$, which is added for all orifices and pressure ranges to Eq. (2.13), resulting in the venting mass flow rate

$$\begin{aligned} \dot{m}_\mathrm{In}(p_\mathrm{V}) =& K_\mathrm{Vent} \cdot A_\mathrm{Vent} \cdot \sqrt{2 \cdot p_\mathrm{A} \cdot \rho_\mathrm{A}} \\ & \cdot \begin{cases} \sqrt{\frac{\kappa_\mathrm{V}}{\kappa_\mathrm{V}-1} \cdot \left[\left(\frac{p_\mathrm{V}}{p_\mathrm{A}}\right)^{\frac{2}{\kappa_\mathrm{V}}} - \left(\frac{p_\mathrm{V}}{p_\mathrm{A}}\right)^{\frac{\kappa_\mathrm{V}+1}{\kappa_\mathrm{V}}} \right]} & \text{, subcritical flow} \\ \left(\frac{2}{\kappa_\mathrm{V}+1}\right)^{\frac{1}{\kappa_\mathrm{V}-1}} \cdot \sqrt{\frac{\kappa_\mathrm{V}}{\kappa_\mathrm{V}+1}} & \text{, critical flow}\,. \end{cases} \end{aligned} \tag{5.19}$$

More information on the determination of K_Vent can be found in Appendix B.2. Targeted flow experiments at room temperature using different venting sections and initial vacuum pressures could help to generalize the definition of the flow rate coefficient and to improve the accuracy of the predicted venting mass flow rate and thus of the whole dynamic model.

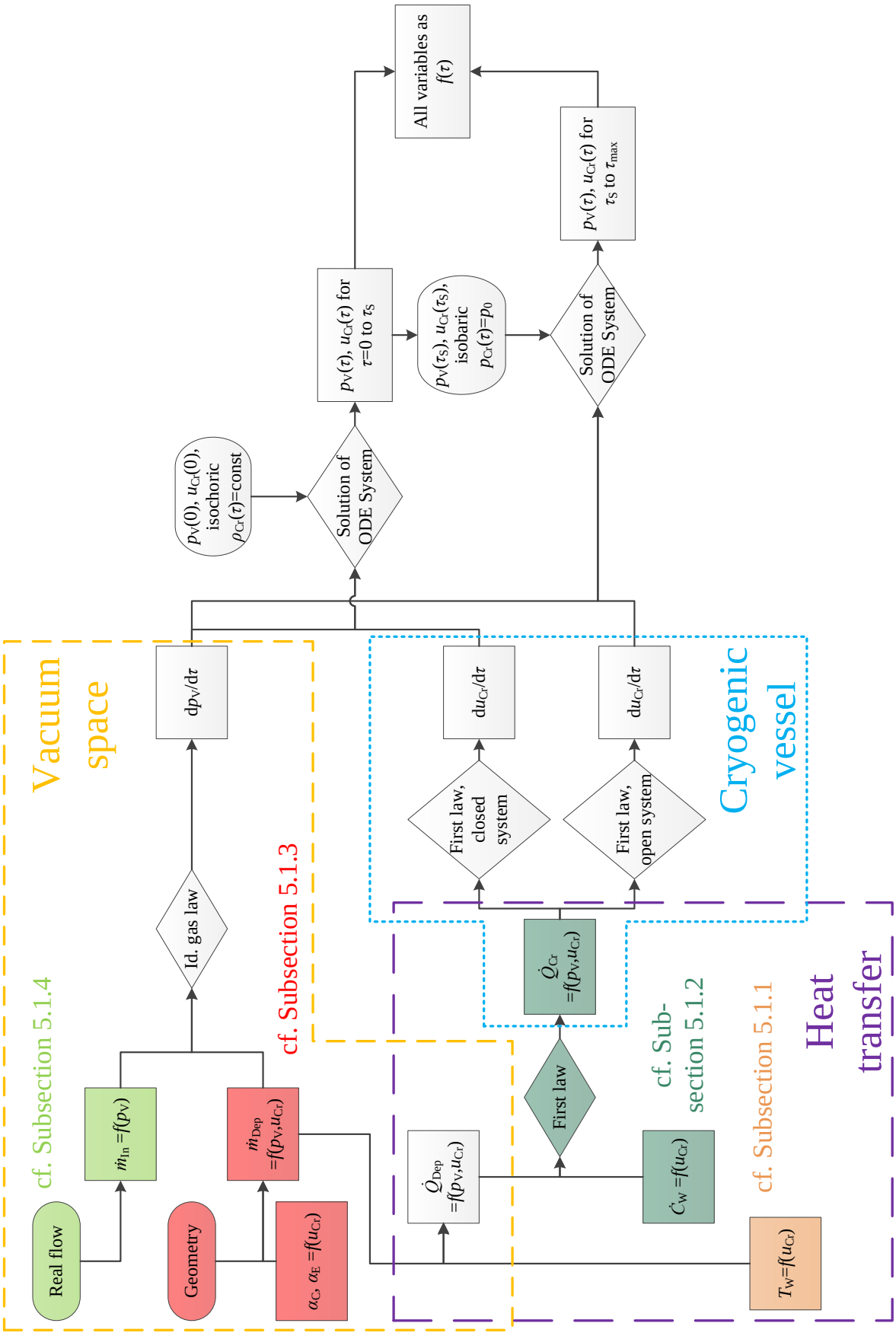

Figure 5.4: Block diagram of the refined model.

5.2 Validation of the refined dynamic model

In order to validate the refined model presented in the previous section, the results of exemplary calculations are compared to the processes during LIV measured at PICARD. The modelled results of major LIV are compared to MP7, while the modelled results of minor LIV are compared to MP5. The model input parameters listed in Table 5.1 are chosen as close as possible to the experimental conditions. Besides this, the results of the calculations based on the refined model are compared to the original dynamic model presented in Section 2.4 and to literature data. An additional comparison between the experimental results of medium LIV (exemplary for MP3) and the original and refined model can be found in Subsection 5.2.4.

5.2.1 Vacuum pressure and wall temperature increase

For major LIV, the comparison between the measured and the calculated vacuum pressure is shown in Figure 5.5(a). The discussion of the vacuum pressure increase measured during MP7 can be found in Section 4.1. The vacuum pressure calculated with the original model directly increases to about 950 mbar(a) without the delay observed during MP7, which results in an overestimation of the vacuum pressure for the first 5 s of the experiment. For the time between $6 \ldots 15$ s, the vacuum pressure calculated with the original model is slightly smaller than the measured vacuum pressure. On the other hand, the general shape of the vacuum pressure increase calculated with the refined model corresponds well with the experimental results for the time of interest after the start of the venting process: Both in the experiment and in the refined model, the vacuum pressure increases to a first plateau at about 50 mbar(a) within less than 1 s where it remains almost constant for a short time, before it further increases to almost 1000 mbar(a) after 6 s from the start of the venting process. Especially for the first second and for the time between $6 \ldots 15$ s, both the shape and the absolute values of the refined model calculation are in good agreement with the experimental results. Between $1 \ldots 6$ s, the measured vacuum pressure exceeds the modelled vacuum pressure. This larger deviation may be explained by the simplified linear interpolation of the condensation coefficient α_C and the evaporation coefficient α_E in the range of $T_W = 20 \ldots 63$ K. This approach apparently overestimates the cryopumping of the cryogenic vessel surface. In general, however, the comparison shows that the refined model is more suitable to describe the trend and the absolute values of the vacuum pressure during major LIV than the original model.

The comparison between the measured and modelled wall temperature for major LIV is shown in Figure 5.5(c). The evolution of the average measured wall temperature is discussed in Section 4.3. In the original model, the wall temperature is defined to equal the helium temperature as a first approximation and is displayed as a dashed grey line. $T_{W,\text{original model}}$ remains below 20 K for 11 s, before it increases to about 40 K within 4 s, which is clearly below the measured wall temperature. Contrarily, both the measured average wall temperature and the wall temperature calculated with the refined model are in good agreement due to the empirical function implemented in form of Eq. (5.7) and shown in Figure 5.3(b).

Table 5.1: Settings of the refined and the original model for the comparison with the experimental results of MP7 (major LIV) and MP5 (minor LIV).

Parameter	Model settings for major LIV	Model settings for minor LIV
Cryogenic Fluid	Helium	Helium
Venting Fluid	Nitrogen	Nitrogen
Valve opening pressure	6.8 bar(g)	2.7 bar(g)
Initial filling level	59.9 cm	79.0 cm
Initial vacuum pressure	10^{-3} mbar(a)	10^{-3} mbar(a)
Initial helium pressure	0.2 bar(g)	0.2 bar(g)
Ambient temperature	296.9 K	296.3 K
Ambient pressure	1.013 bar(a)	1.013 bar(a)
Venting diameter	30.0 mm	12.5 mm
Vacuum vessel volume	400 L	400 L
Cryogenic vessel volume	107 L	107 L
Surface area, cryogenic vessel	1.25 m^2	1.25 m^2

For minor LIV, the comparison between the modelled and measured vacuum pressure increase is shown in Figure 5.5(b). Again, the discussion of the measured vacuum pressure increase can be found in Section 4.1. The vacuum pressure calculated with the original model shows a strong increase to $p_V = 100$ mbar(a) within 1.5 s, thus highly overestimating the vacuum pressure compared to the measured values. Both the measured vacuum pressure and the vacuum pressure calculated with the refined model increase to about $p_V = 5$ mbar(a) within the first milliseconds. Unlike during major LIV, the vacuum pressure during MP5 and in the refined model for minor LIV remain at low pressures in the range of $p_V = 10$ mbar(a). During MP5, the vacuum pressure slightly decreases again after about 6 s, while the vacuum pressure calculated with the refined model continuously increases slightly. Considering the great difference between the range and dynamics of the vacuum pressure for minor and major LIV, the refined model reproduces the experimental results of both extremes very well and clearly represents an improvement to the original model.

The modelled and the measured average wall temperature during minor LIV is displayed in Figure 5.5(d). Both results of the refined modelling are in good agreement again due to the empirical Eq. (5.8) and its representation in Figure 5.3(b).

5.2.2 Helium temperature and pressure increase

The measured and modelled helium temperature and pressure increase during major and minor LIV is shown in Figure 5.6. The measured results are discussed in Section 4.2. The average helium temperatures are calculated from TI12, TI13, TI14, TI15 and TI18 shown in Figure 4.2. During major LIV, the helium temperature predicted by the original model shown in Figure 5.6(a) equals the wall temperature shown in

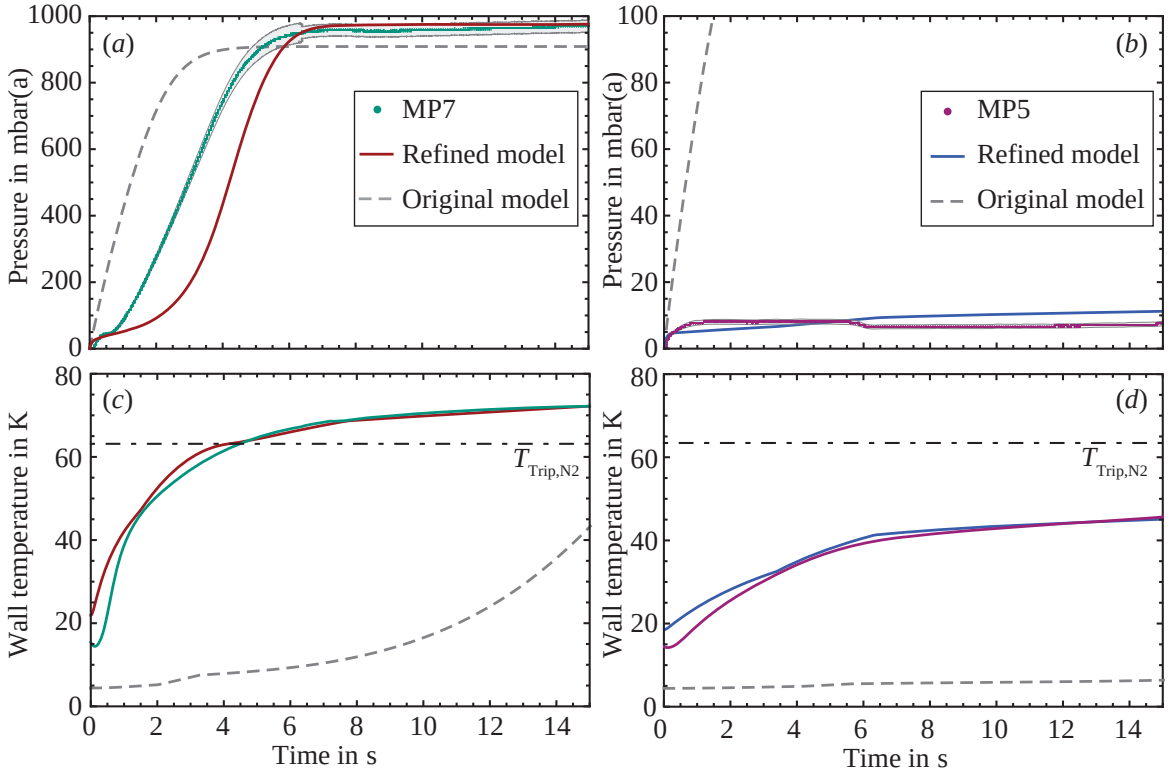

Figure 5.5: Modelled and measured (a,b) vacuum pressure and (c,d) average wall temperature during (a,c) major LIV (MP7) and (b,d) minor LIV (MP5). The measurement uncertainties are again displayed in light grey.

Figure 5.5(c). The measured helium temperature and the one calculated with the refined model only slowly increase with a flatter slope during the first 15 s from the start of major LIV. During the unstable operation of the safety relief valve explained in Section 4.2, the fluctuation of the measured helium temperature slightly exceeds the helium temperature predicted by the refined model. In general, the measured helium temperature increase can be reproduced very well with the refined model.

The comparison between the calculated and the measured helium pressure during major LIV is shown in Figure 5.6(c). Both the measured and the calculated helium pressure curves change their slope at the phase change of helium close to the critical point, and further increase until the opening pressure of the safety relief valve is reached. For the validation of the model, the opening pressure has been set to the measured opening pressure under experimental conditions. Since isobaric conditions inside the cryogenic vessel are assumed for both the original and the refined model, the modelled helium pressure remains constant at $p_{\mathrm{open}} = 6.8\,\mathrm{bar(g)}$ during discharge. Same as the helium temperature, also the helium pressure predicted by the original model increases faster than measured during MP7 and reaches the opening pressure of the safety relief valve already after 3 s instead of after 6 s during MP7. The result of the helium pressure predicted by the refined model is displayed in red in Figure 5.6(c). For the first 4 s from the start of the venting process, it increases faster than the measured helium

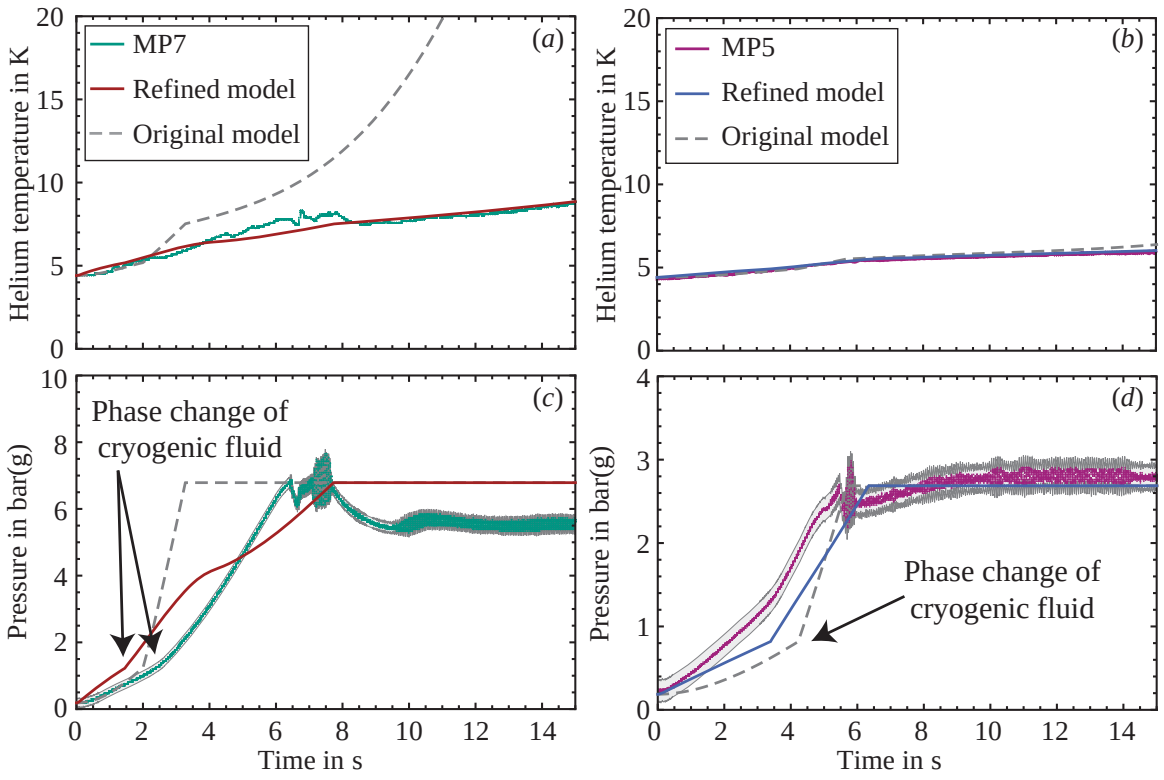

Figure 5.6: Modelled and measured (a,b) average helium temperature and (c,d) helium pressure during (a,c) major LIV (MP7) and (b,d) minor LIV (MP5).

pressure. The steeper slope in the beginning may be associated to the over-prediction of the cryopumping (and thus the deposited mass flow rate) shown in Figure 5.5(a). A second change of slope in the helium pressure occurs after 4 s at the time of the phase change of the venting fluid deposited at the cold surface shown in Figure 5.5(c). Due to the shallower pressure increase after 4 s, the predicted helium pressure reaches the opening pressure of the safety relief valve about 1.5 s later than measured during MP7.

For minor LIV, the comparison between the modelled and the average measured helium temperature is displayed in Figure 5.6(b). As can be seen, the results of the refined and the original model are almost congruent with the experimental results of MP5.

The helium pressure in the cryogenic vessel during minor LIV calculated with the original and refined model is compared to the experimental results of MP5 in Figure 5.6(d). In both model calculations, the helium pressure increases slower than measured during MP5 in the two-phase region, but faster in the supercritical pressure range with the refined model results being closer to the measured values. Same as for the helium temperature, the curves of the helium pressure calculated with the refined and the original model do not differ much. The helium pressure predicted by the refined model reaches the opening pressure of the safety relief valve about 1 s after actually measured at PICARD.

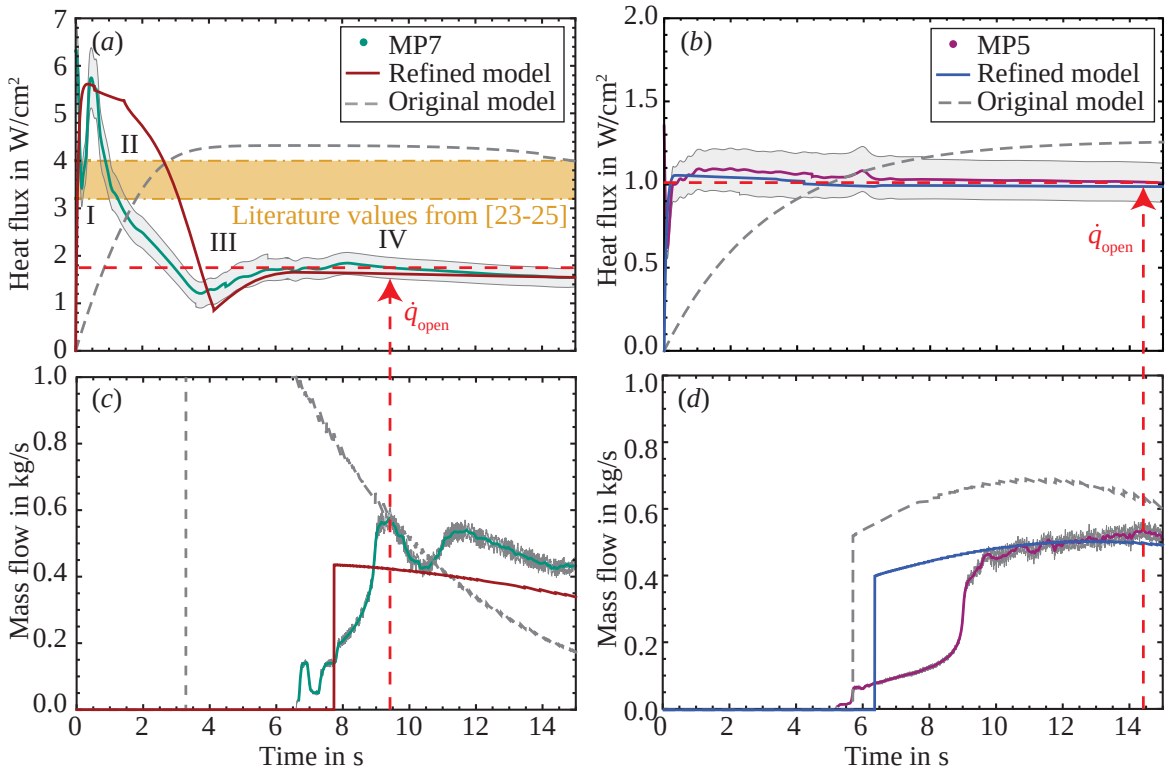

Figure 5.7: Modelled and measured (a,b) heat flux caused by the deposition of the venting fluid and (c,d) helium discharge mass flow rate during major LIV (MP7) and minor LIV (MP5). The four phases of the heat flux evolution for major LIV are indicated with I, II, III and IV.

5.2.3 Heat flux and discharge mass flow rate

The comparison between the modelled and the measured heat flux and mass flow rate during major and minor LIV is shown in Figure 5.7, representing the most relevant results for the design of pressure relief systems. The discussion of the measurement data can be found in Section 4.4. The result of the heat flux calculation based on the original dynamic model is shown as a dashed grey line in Figure 5.7(a). Compared to the experimental data of MP7 displayed in green, the heat flux predicted by the original model increases more slowly within the first 4 s of the venting process to a maximum of about $\dot{q}_{\mathrm{max,original\ model}} = 4.3\,\mathrm{W/cm^2}$. While the curve of the experimental heat flux in MP7 strongly and quickly decreases after an initial maximum, the heat flux calculated with the original model remains about constant between $4 \ldots 15$ s and thus strongly exceeds the measured heat flux.

The general trend of the measured and refined predicted heat flux evolution for major LIV shown in Figure 5.7(a) can be divided in four phases I, II, III and IV: In phase I, both the measured heat flux and the one calculated with the refined model increase within less than one second to a very similar maximum of $\dot{q}_{\mathrm{Dep,max,MP7}} = 5.7\,\mathrm{W/cm^2}$ and $\dot{q}_{\mathrm{Dep,max,refined\ model}} = 5.6\,\mathrm{W/cm^2}$, respectively. These peak values are above the

literature maximum values from [23–25] between $\dot{q}_{\mathrm{Literature}} = 3.1 \ldots 4.0\,\mathrm{W/cm^2}$. In the second phase, the decrease of the heat flux to about $\dot{q}_{\mathrm{Dep,MP7}} = 1.2\,\mathrm{W/cm^2}$ between $1 \ldots 4\,\mathrm{s}$ observed in MP7 is also predicted by the refined model, decreasing to about $\dot{q}_{\mathrm{Dep,refined\ model}} = 0.9\,\mathrm{W/cm^2}$. In the third phase around the triple point of the venting fluid, the measured and refined calculated heat flux first increases again, before the curves remain almost constant between $7 \ldots 15\,\mathrm{s}$ in the fourth phase.

Since the results based on the refined model calculations are in good agreement with the trend of the experimental results, the theoretical considerations of the mass transfer presented in Section 5.1 can be used to explain the trend of both the modelled and measured heat flux over time. Following from Eq. (5.1) as well as Eq. (5.11) to (5.13), the heat flux caused by deposition of the venting fluid, $\dot{q}_{\mathrm{Dep}}$, can be expressed as

$$\dot{q}_{\mathrm{Dep}} \propto \dot{m}_{\mathrm{Dep}} \propto \left(\alpha_{\mathrm{C}} \cdot \frac{p_{\mathrm{V}}}{\sqrt{T_{\mathrm{V}}}} - \alpha_{\mathrm{E}} \cdot \frac{p_{\mathrm{Sat}}(T_{\mathrm{W}})}{\sqrt{T_{\mathrm{W}}}} \right) . \tag{5.20}$$

In phase I, the rapid increase in the heat flux within a very short time after the start of the venting process is a consequence of the increasing vacuum pressure at constant temperature of the gaseous venting fluid in the vacuum space, and the very high sticking probability that results in $\alpha_{\mathrm{C}} = 1$ and $\alpha_{\mathrm{E}} = 0$ assumed for low wall temperatures with

$$p_{\mathrm{V}} \uparrow \Rightarrow \dot{q}_{\mathrm{Dep,I}} \uparrow \ . \tag{5.21}$$

In phase II, the heat flux decreases again due to the decreasing sticking probability and hence decreasing condensation coefficient in combination with increasing evaporation coefficient at $T_{\mathrm{W}} > 20\,\mathrm{K}$ with

$$\alpha_{\mathrm{C}} \downarrow,\ \alpha_{\mathrm{E}} \uparrow \Rightarrow \dot{q}_{\mathrm{Dep,II}} \downarrow \ . \tag{5.22}$$

The peculiar trend of the heat flux with the intermediate increase between $4 \ldots 7\,\mathrm{s}$ shown in phase III can also be explained by the theory of mass transfer: With the phase change of the deposited venting fluid above the triple point, many changes occur simultaneously: On the one hand, the condensation coefficient decreases, while the evaporation coefficient and $p_{\mathrm{Sat}}(T_{\mathrm{W}})/\sqrt{T_{\mathrm{W}}}$ increase. As can be seen in Eq. (5.20), this leads to a decreasing deposition mass flow rate and hence a decreasing heat flux as

$$\alpha_{\mathrm{C}} \downarrow,\ \alpha_{\mathrm{E}} \uparrow,\ \frac{p_{\mathrm{Sat}}(T_{\mathrm{W}})}{\sqrt{T_{\mathrm{W}}}} \downarrow \Rightarrow \dot{q}_{\mathrm{Dep,IIIa}} \downarrow \ . \tag{5.23}$$

On the other hand, the vacuum pressure strongly increases between $4 \ldots 7\,\mathrm{s}$ as can be seen in Figure 5.5(a), which results in an increasing deposition mass flow rate, yielding an increasing heat flux as

$$p_{\mathrm{V}} \uparrow \Rightarrow \dot{q}_{\mathrm{Dep,IIIb}} \uparrow \ . \tag{5.24}$$

Thus, the changing impact of the two opposite influences around the triple point of the venting fluid gives an explanation for the slope inversion of the heat flux during major LIV. At $T_{\mathrm{W}} > T_{\mathrm{Trip,N2}}$ in phase IV, the vacuum pressure shown in Figure 5.5(a) hardly changes any more and α_{C} and α_{E} are assumed to be constant. At the same time, the wall temperature shown in Figure 5.5(c) still slowly increases. Since $p_{\mathrm{Sat}}(T_{\mathrm{W}})/\sqrt{T_{\mathrm{W}}}$

increases with increasing wall temperature, the deposition mass flow rate and hence also the heat flux slowly decrease as

$$\frac{p_{\mathrm{Sat}}(T_{\mathrm{W}})}{\sqrt{T_{\mathrm{W}}}} \downarrow \Rightarrow \dot{q}_{\mathrm{Dep,IIIa}} \downarrow \ . \tag{5.25}$$

Similar as for the vacuum pressure, the heat flux calculated with the refined model is in very good agreement with the heat flux data measured during MP7, except for the time between about $1 \ldots 4\,\mathrm{s}$ where the heat flux calculated with the refined model decreases more slowly than measured during MP7. This larger deviation of the heat flux calculated with the refined model from the measured heat flux can again be explained by the simplified linear interpolation of α_{C} and α_{E} at temperatures between $20\,\mathrm{K} \leq T_{\mathrm{W}} < T_{\mathrm{Trip,N2}}$ in the calculation of the deposition mass flow rate and hence in the heat flux. In addition, the conductive resistance of the frost layer, which is not contained in the model, may explain the remaining difference between the model and the experimental data. A more detailed modelling of the deposition process based on a broader experimental basis could further improve the prediction.

The discharge mass flow rate calculated with the models for major LIV in comparison to the experimental results of MP7 is shown in Figure 5.7(c). The discharge process calculated with the original dynamic model starts about 3.5 s earlier than measured in MP7 as a direct consequence of the faster helium pressure increase shown in Figure 5.6(c) and highly overestimates the measured discharge mass flow rate as a direct consequence of the larger heat flux shown in Figure 5.7(a). The first discharge mass flow rate is measured in MP7 after about 6.5 s, while the calculated discharge process according to the refined model starts about 1 s later. This is a consequence of the helium pressure reaching the opening pressure later in the refined model than measured during the experiment as shown in Figure 5.6(c). The discharge mass flow rate in the refined model is calculated directly from the change in helium temperature at constant helium pressure and thus assumes an ideal safety relief valve, while the valve operated unstably during the experiment: While the safety relief valve chatters after the first opening in MP7 with reduced discharge capacity, the modelled discharge mass flow rate directly increases to the peak value of about $\dot{m}_{\mathrm{max,refined\ model}} = 0.42\,\mathrm{kg/s}$, which is smaller than the maximum measured discharge mass flow rate of $\dot{m}_{\mathrm{max,MP7}} = 0.58\,\mathrm{kg/s}$.

For the dimensioning of safety relief devices, only the heat flux $\dot{q}_{\mathrm{open}}$, when the maximum discharge mass flow rate occurs, is relevant. Although there is still some deviation between the measured and the modelled heat flux for major LIV, the modelled heat flux of $\dot{q}_{\mathrm{Dep,refined\ model,open}} = 1.6\,\mathrm{W/cm^2}$ is much closer to the measured $\dot{q}_{\mathrm{Dep,MP7,open}} = 1.75\,\mathrm{W/cm^2}$ than the constant literature values of $\dot{q}_{\mathrm{Literature}} = 3.1 \ldots 4.0\,\mathrm{W/cm^2}$ [23–25] as shown in Figure 5.7(a). This smaller difference in the heat flux has direct implications on the sizing of safety relief devices: In analogy to Section 4.4, the discharge mass flow rate and the resulting required discharge diameter of a safety relief valve calculated following the established design steps from [17, 21] explained in Section 2.3 is shown in Table 5.2. The discharge diameter of $d_{0,\mathrm{Dep,refined\ model}} = 14.1\,\mathrm{mm}$ based on the heat flux caused by deposition predicted with the refined model is much closer to the actually required discharge diameter of

Table 5.2: Exemplary calculation of the discharge mass flow rate $\dot{m}_{\mathrm{Out}}$ according to ISO 21013-3 [21] and discharge diameter d_0 of a safety relief valve according to ISO 4126-1 [17] for the set conditions in MP7 based on measured and modelled heat fluxes.

Input	$\dot{m}_{\mathrm{Out}}$ in kg/s	d_0 in mm
$\dot{q}_{\mathrm{Cavallari}} = 4\,\mathrm{W/cm^2}$ [24]	1.6	22.2
$\dot{q}_{\mathrm{Dep,MP7,open}} = 1.75\,\mathrm{W/cm^2}$	0.7	14.7
$\dot{q}_{\mathrm{Dep,refined\ model,open}} = 1.6\,\mathrm{W/cm^2}$	0.65	14.1
$\dot{q}_{\mathrm{Cr,refined\ model,open}} = 1.3\,\mathrm{W/cm^2}$	0.53	12.7

$d_{0,\mathrm{Dep,MP7}} = 14.7\,\mathrm{mm}$ than calculated with the literature values. Thus, the first modelling results indicate that the consideration of the process dynamics leads to a major improvement in the sizing of safety relief devices for liquid helium applications.

The comparison between the modelled and the measured heat flux for minor LIV is shown in Figure 5.7(b). Same as for major LIV, the heat flux calculated with the original model increases much slower and to a higher value than measured during MP5. On the other hand, the refined model calculations result in an almost identical shape to the experimental results for the whole displayed 15 s from the start of the venting process with an almost direct increase to about $\dot{q}_{\mathrm{refined\ model}} = 1.0\,\mathrm{W/cm^2}$. Again, the small leap in the heat flux curves at the triple point of the venting fluid after about 4 s is caused by the change of state and the resulting leap in the fluid property data used for the calculation of the heat flux both in the refined model and in the experimental results.

For minor LIV, the discharge mass flow rates calculated with the refined and the original model as well as measured during MP5 are shown in Figure 5.7(d). The discharge mass flow rate calculated with the original model directly increases to a value above the measured maximum mass flow rate, before it further increases to about $\dot{m}_{\mathrm{original\ model}} = 0.7\,\mathrm{kg/s}$. The helium discharge calculated with the refined model starts about 1 s after the first discharge mass flow rate is measured during MP5 as a consequence of the slightly slower helium pressure increase shown in Figure 5.6(d). Same as for major LIV, the discharge mass flow rate calculated with the refined model for minor LIV directly increases in a step to about $\dot{m}_{\mathrm{refined\ model}} = 0.4\,\mathrm{kg/s}$. Again, the non-ideal behaviour of the safety relief valve during operation, in this case the simmering during MP5, is not modelled. With the measured pressure during MP5 approximately remaining at the opening pressure (Figure 5.6(d)), both the trend and the absolute value of the refined modelled discharge mass flow rate correspond well with the measurement data after about 10 s, when the safety relief valve operates stably during the experiment. This gives confidence in the overall approach.

Under consideration of the temperature increase in the cryogenic vessel wall explained in Subsection 5.1.2, the heat flux $\dot{q}_{\mathrm{Cr}} < \dot{q}_{\mathrm{Dep}}$ that is transferred to the cryogenic fluid has been calculated. A comparison between these modelled heat fluxes for major

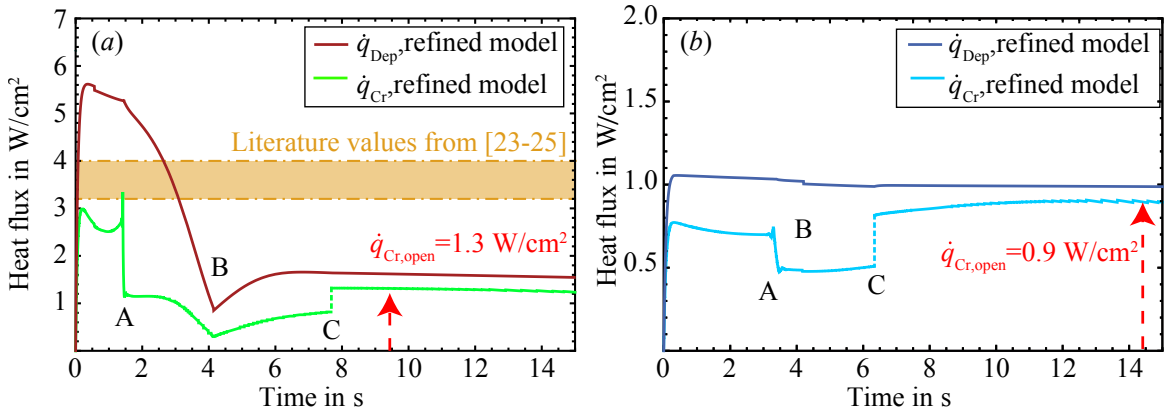

Figure 5.8: Modelled heat flux caused by the deposition of the venting fluid $\dot{q}_{\mathrm{Dep}}$ and heat flux transferred to the cryogenic fluid $\dot{q}_{\mathrm{Cr}}$ during (a) major LIV and (b) minor LIV. The discontinuities in the curve of $\dot{q}_{\mathrm{Cr}}$ are caused by A: phase change of the cryogenic fluid, B: phase change of the venting fluid, C: transition isochoric-isobaric.

and minor LIV calculated with the settings listed in Table 5.1 is shown in Figure 5.8. Both curves of $\dot{q}_{\mathrm{Cr}}$ show three discontinuities marked A, B and C that are a consequence of the determination of $\dot{q}_{\mathrm{Cr}}$ according to Eq. (5.10): After 1.5 s during major LIV and after 3.5 s during minor LIV, the cryogenic fluid inside the closed vessel becomes supercritical, which results in a change of slope of T_{Cr} as shown in Figure 5.6(a,b) and therefore also in a change of slope of $T_{\mathrm{W}} = f(T_{\mathrm{Cr}})$ (cf. Eq.(5.7) and Eq.(5.8)) shown in Figure 5.5(c,d). As $\dot{q}_{\mathrm{Cr}}$ is a function of $\mathrm{d}T_{\mathrm{W}}/\mathrm{d}\tau$, a sharp peak can be observed in the curves at point A in Figure 5.8. The change of slope after 4 s during major and minor LIV (marked B) is a result of the phase change of the venting fluid from solid to liquid, which results in a change of the fluid property data and can also be observed for $\dot{q}_{\mathrm{Dep}}$. The step in the curves of $\dot{q}_{\mathrm{Cr}}$ after about 7.5 s during major LIV and after about 6.5 s during minor LIV (marked C) is again a consequence of the change of slope of $T_{\mathrm{W}} = f(T_{\mathrm{Cr}})$ caused by the transition from isochoric to isobaric conditions inside the cryogenic fluid.

Within a few milliseconds after the start of the venting process during major LIV shown in Figure 5.8(a), the predicted heat flux that is transferred to the cryogenic fluid increases to a maximum of $\dot{q}_{\mathrm{Cr,max}} = 3\,\mathrm{W/cm^2}$, which is considerably lower than $\dot{q}_{\mathrm{Dep,max}} = 5.6\,\mathrm{W/cm^2}$, but corresponds well with $\dot{q}_{\mathrm{Harrison}} = 3.1\,\mathrm{W/cm^2}$ measured in [25] based on the change of state of helium inside the cryogenic vessel and with $\dot{q}_{\mathrm{Cr,Dhuley}} = 3.0\,\mathrm{W/cm^2}$ calculated in [38] based on the restrictions by film boiling of liquid helium. At the time of interest when the maximum discharge mass flow rate occurs, the predicted heat flux transferred to the cryogenic fluid has already decreased to $\dot{q}_{\mathrm{Cr,refined\ model,open}} = 1.3\,\mathrm{W/cm^2}$. According to ISO 21013-3 [21], this corresponds to a discharge mass flow rate of $\dot{m}_{\mathrm{Out}} = 0.53\,\mathrm{kg/s}$ and according to ISO 4126-1 [17] to a discharge diameter $d_{0,\mathrm{Cr,refined\ model}} = 12.7\,\mathrm{mm}$ of a safety relief valve, which is smaller than $d_{0,\mathrm{Dep,refined\ model}} = 14.1\,\mathrm{mm}$ as can be seen in Table 5.2.

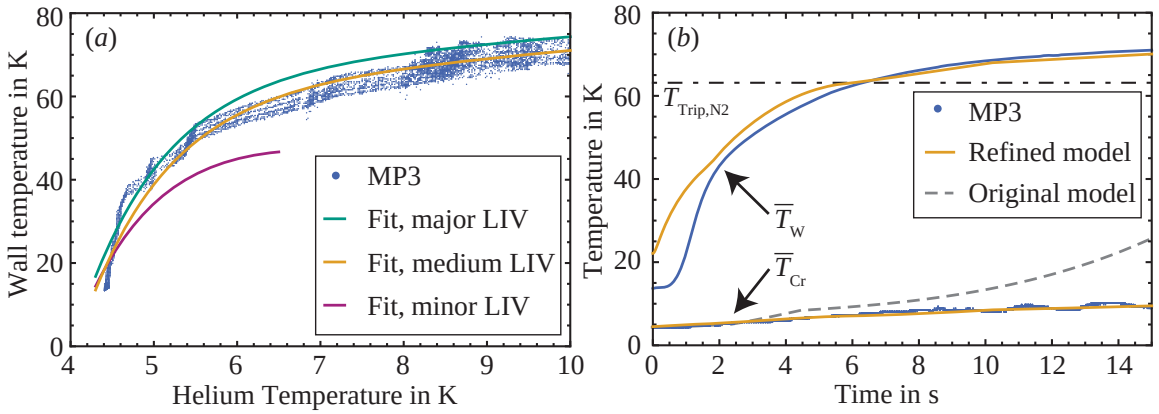

Figure 5.9: (a) Average measured wall temperature as a function of the average measured helium temperature for the first 15 s of medium LIV (MP3) with the fit functions of major, medium and minor LIV, and (b) modelled and measured average helium and wall temperatures during medium LIV (MP3) over time.

For minor LIV shown in Figure 5.8(b), the heat flux transferred to the cryogenic fluid is about 30 % smaller than the deposited heat flux at the start of the venting process. This difference further increases between 1.5 and 6.5 s from the start of the venting process to about 50 % smaller values. After the opening of the safety relief valve, $\dot{q}_{\mathrm{Cr}}$ increases again to values higher than in the beginning of the experiment. When the maximum discharge mass flow rate occurs, the predicted heat flux transferred to the cryogenic fluid reaches $\dot{q}_{\mathrm{Cr,refined\ model,open}} = 0.9\,\mathrm{W/cm^2}$, which is only 10 % below $\dot{q}_{\mathrm{Dep,refined\ model,open}}$.

5.2.4 Validation for medium loss of insulating vacuum

Same as for minor and major LIV (explained in Subsection 5.1.1), a least-squares fit to the measurement data yields the empirical fit function for $\bar{T}_{\mathrm{W}} = f(T_{\mathrm{Cr}})$ for medium LIV of

$$T_{\mathrm{W,MP3}}(T_{\mathrm{Cr}}) = 54\,\mathrm{K} - 3528\,\mathrm{K} \cdot e^{-\frac{T_{\mathrm{Cr}}}{\mathrm{K}}} + 1.72 \cdot T_{\mathrm{Cr}} \tag{5.26}$$

plotted in orange in Figure 5.9(a) with the original measured data for MP3 and the fit functions for minor and medium LIV. With a venting diameter of $d_{\mathrm{Or}} = 25\,\mathrm{mm}$ used for MP3, the fit clearly differs from the fit function of minor LIV ($d_{\mathrm{Or}} = 12.5\,\mathrm{mm}$) but is close to the fit function of major LIV ($d_{\mathrm{Or}} = 30\,\mathrm{mm}$).

For the comparison between the experimental data of MP3 and the results of model calculations for medium LIV, the settings listed in Table 5.3 have been used as input parameters. For medium LIV, the experimental results of MP3 are shown in blue with the measurement uncertainty again inserted in light grey, while the results of calculations based on the refined model are displayed in orange. The model calculations based on the original model are again inserted in dashed grey.

The comparison between the measured and modelled helium and wall temperature

Table 5.3: Settings of the refined and the original model of medium LIV for the comparison with the experimental results of MP3.

Parameter	Setting for medium LIV
Cryogenic Fluid	Helium
Venting Fluid	Nitrogen
Valve opening pressure	8.75 bar(g)
Initial filling level	56 cm
Initial helium pressure	0.29 bar(g)
Ambient temperature	297.6 K
Ambient pressure	1.013 bar(a)
Venting diameter	25 mm
Vacuum vessel volume	400 L
Cryogenic vessel volume	107 L
Surface area, cryogenic vessel	1.25 m^2

for medium LIV is shown in Figure 5.9(b). Same as for major and minor LIV discussed in Section 5.2, both the shape and the absolute values of the refined model calculation is in good agreement with the experimental results of MP3 again due to the fit function in Eq. (5.26). In comparison, the temperature $T_W = T_{Cr}$ calculated with the original model highly underestimates the measured wall temperature.

The comparison between the measured and modelled vacuum pressure, helium pressure, heat flux and discharge mass flow rate during medium LIV is shown in Figure 5.10. As has been expected from the similar size of the venting orifice, both the experimental results and the results of the refined and original model resemble the results of major LIV presented in Section 5.2. Same as for major LIV shown in Figure 5.5(a), the vacuum pressure calculated with the refined model increases slower than measured during MP3 as can be seen in Figure 5.10(a). The modelled and the measured helium pressure increase for medium LIV is shown in Figure 5.10(c). Again, the phase change of the cryogenic fluid is visible as a bend in all helium pressure curves and is predicted to occur slightly earlier with the refined model, while the first opening of the safety relief valve is predicted later than measured during MP3. Same as for MP7, the unstable operation of the safety relief valve is not included in the model.

The result of the heat flux calculation for medium LIV based on the original model is shown as a dashed grey line in Figure 5.10(b). Same as for major LIV, the heat flux predicted with the original model increases more slowly than measured during MP3, while the results predicted with the refined model are in good agreement for the first 1.5 s and for the time after the first opening of the safety relief valve at about 8 s after the start of the experiment. Again, the larger deviation of the results between $T_W = 20 \ldots 63$ K especially of the vacuum pressure and heat flux can be explained by the simplified modelling of the desublimation process with linearly interpolated condensation and evaporation coefficients. The comparison between the measured and modelled discharge mass flow rate during medium LIV is shown in Figure 5.10(d).

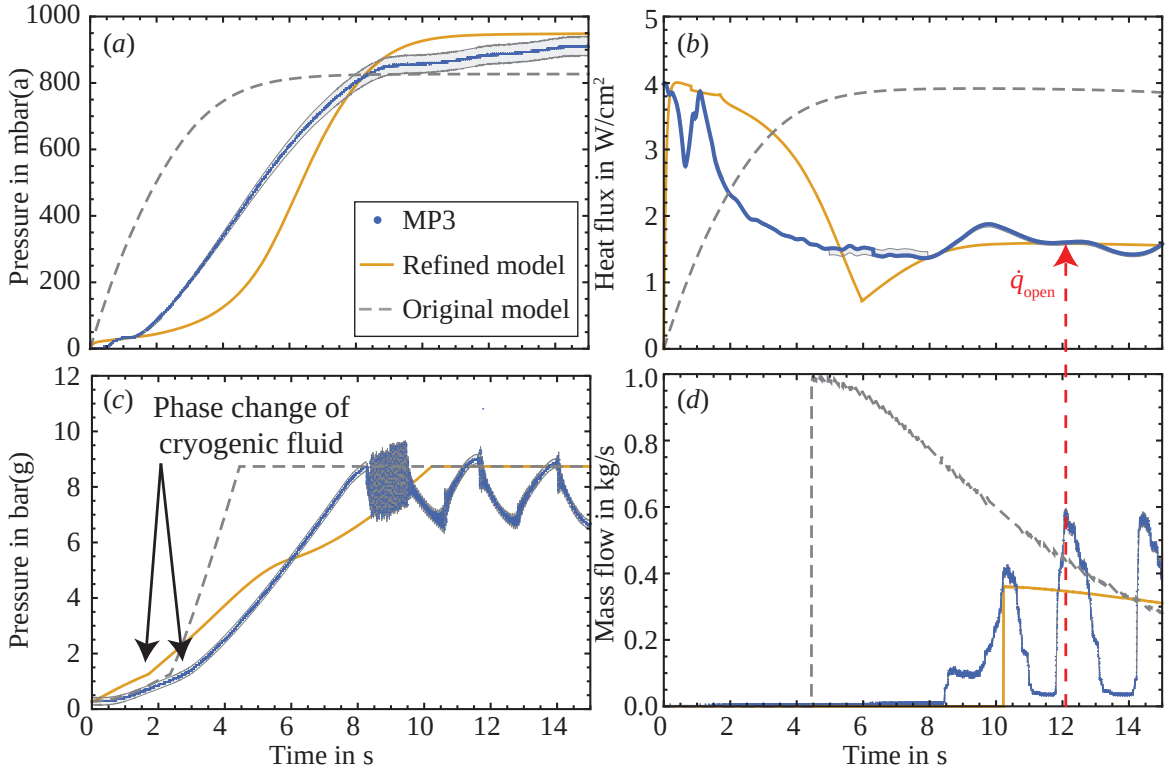

Figure 5.10: Modelled and measured (a) vacuum pressure, (c) helium pressure, (b) heat flux and (d) discharge mass flow rate during medium LIV (MP3).

Because of the long duration of the unstable operation of the safety relief valve, the measured discharge mass flow rate during MP3 is subject to large changes. As both the original and the refined model assume an ideal valve operation, the fluctuations in the discharge mass flow rate are not predicted. Nevertheless, the general agreement between model and experiment is much better for the results calculated with the refined model than those calculated with the original model. Same as for major and minor LIV, the comparison between the modelled and measured heat flux at the time when the maximum discharge mass flow rate occurs shows a very good correspondence between MP3 and the refined model.

5.3 Conclusions

The original dynamic model of the physical processes during LIV presented in Section 2.4 has been refined concerning the heat and mass transfer at the cryogenic vessel wall. Through fitting of the average wall temperature as a function of the helium temperature, the overall heat transfer resistance is included in the model for minor, medium and major LIV, respectively. By including the temperature increase of the cryogenic vessel wall and a flow rate coefficient for the non-ideal venting section, the model has further been improved. The modelling of the mass transfer at the cryogenic vessel wall

is considerably refined by including the deposition based on the *Hertz-Knudsen equation*. With values of the sticking coefficient for very low and high temperatures from literature and linear interpolation, the influence of both desublimation/condensation and sublimation/evaporation on the mass transfer is included. Besides this, the influence of obstacles preventing the venting fluid from directly reaching the cold surface inside the vacuum space is taken into account in the *Hertz-Knudsen equation*.

With this refined model, the process dynamics of the vacuum pressure increase, helium temperature and pressure rise as well as the wall temperature increase and the evolution of the heat flux and discharge mass flow rate at PICARD can be predicted well. The comparison between the original and the refined model shows great improvement in predicting both the trend and the absolute values of the experimental results. Based on the kinetic theory used for the modelling of the mass transfer, the particular shape of the measured heat flux evolution could be well explained. This gives confidence in the refined model and the method for calculating the heat flux from experimental data.

Nevertheless, the presented refined dynamic model only represents an intermediate step towards a generally valid model: Because the wall temperature is fitted to experimental values, the refined model is not independent of experimental data. For the further development of the model, the wall temperature could be described based on the observed inequality between the heat flux caused by the deposition of the venting fluid and the heat flux transmitted to the cryogenic fluid. First experimental data suggest that the heat transfer for major LIV is limited by the heat transfer to the helium, while it is limited during minor LIV by the desublimation and condensation of the venting fluid at the cold surface. Therefore, the modelling of the heat flux transmitted to the cryogenic fluid will be an important task for the further development of the model.

Not only the wall temperature, but also the venting coefficient (taking into account the non-ideal venting section) and the transmission coefficient (describing the transfer of the gas molecules through the obstacles between the orifice venting section and the cold surface) have been determined experimentally and are thus only valid for specific experimental conditions. To generalize and validate a reliable dynamic model, a broader experimental basis is therefore yet required. This includes more LIV experiments as well as a detailed study of the venting and the desublimation processes and of the operating characteristics of safety relief valves.

CHAPTER 6

Summary

Liquid helium is the coolant of choice for many superconducting applications such as superconducting magnets. Due to the low operating temperature in combination with helium's low enthalpy of evaporation, great care must be taken in the design of cryogenic pressure relief systems [16]. In hazard analyses, the venting of the insulating vacuum with atmospheric air is often considered as the worst-case scenario [16]. The dimensioning of cryogenic safety relief devices requires detailed knowledge on the processes and process dynamics following such incidents [26]. However, the established standards and design codes such as [15, 17–22] do not fully consider the particular conditions in liquid helium cryostats. For instance, relief flow rates are usually calculated under the simplifying assumption of a constant maximum heat flux into the cryogenic vessel based on few experimental data as explained in Chapter 2. Thus, the process dynamics is often neglected, leading to potentially over-sized dimensions for safety relief devices. Besides higher acquisition costs and space requirements, over-sizing can also lead to chattering, i.e. unstable operation of safety relief valves with reduced discharge capacity [27]. The physical mechanisms of failure scenarios have not yet been fully analysed [16]. An existing dynamic model [16] explained in this chapter contains simplifications especially concerning the heat and mass transfer that cannot be described purely analytically but must be parametrized and validated by experiments.

In order to better understand the processes during loss of insulating vacuum, the cryogenic safety test facility PICARD has been successfully designed, constructed and commissioned in the course of this work as presented in Chapter 3. PICARD consists of an inner cryogenic vessel designed for a cryogenic liquid volume of 100 L surrounded by an insulating vacuum. The cryogenic volume is protected with a rupture disk at $p_S = 16\,\mathrm{bar(g)}$, allowing cryogenic safety experiments at pressures up to $p_0 = 12\,\mathrm{bar(g)}$ and discharge mass flow rates of up to 4 kg/s. The data is taken with 31 sensors with sufficiently low measurement uncertainties at very high sampling rates of up to 1 kHz. The description of the experimental method for measuring and evaluating the data of all relevant process parameters is a key focus of this chapter. Thus, a broad range

of safety experiments and a detailed study of the processes following incidents can be conducted at PICARD [27]. The investigation of different established adjustment methods of safety relief valves [14] showed large differences between the set pressure according to the methods "bubble test" and "initial audible discharge". The actual opening pressure under experimental conditions exceeded the set pressures by up to 26 % in case of "initial audible discharge" and even more in case of "bubble test". This deviation from the allowed maximum 10 % overpressure for full-lift safety relief valves [17] may be explained by the much faster pressure increase during operation compared to the adjustment procedure. During the experiments, the insulating vacuum of the liquid helium cryostat was vented with gaseous nitrogen or atmospheric air. Parts of the inflowing warm gas froze out on the cold surface of the cryogenic vessel, causing a heat flux that was transferred to the helium inside the cryogenic vessel. Both the temperature and the pressure of the helium increased until the opening pressure of the safety relief valve was reached and the helium was released into a quench gas line [26, 27].

The results of first venting experiments conducted within the framework of an R&D collaboration between KIT and CERN on cryogenic pressure relief [54] were presented in Chapter 4. Especially during venting experiments with a low initial filling level, large stratification of the helium temperature inside the cryogenic vessel was observed. Unstable operation of the safety relief valve (chattering) with significant overpressures in the range of up to 50 % with regard to the set pressure occurred during all experiments. Similar observations have been made during experiments at CERN [69]. Causes for chattering could be over-sizing as well as large pressure losses at the inlet of the safety relief valve. Such overpressures would trigger the bursting of a rupture disk in a staged cryostat pressure protection system if the margin between the set pressures of the safety relief valve and the rupture disk is too small [27]. Consequences of open systems involve large helium losses and the possible contamination with air humidity in the system. In systems without an additional protection level, the observed overpressures could even lead to plastic deformation or mechanical failure [27]. Therefore, the design of staged pressure relief systems with a sufficiently large margin between the set pressure of the safety relief valve and the bursting pressure of a rupture disk is recommended, provided this is in accordance with other design constraints. Furthermore, measures for a stable operation of safety relief valves without chattering, such as lower reseating pressures of safety relief valves or the additional use of control valves, have been proposed.

For experiments conducted with a small venting diameter, the heat flux caused by the deposition of the venting fluid did not exceed $\dot{q} = 1.2\,\mathrm{W/cm^2}$ and remained nearly constant for the time of interest, indicating a low time-dependence of the heat flux for minor incidents. During experiments conducted with large venting diameters, peak heat fluxes of up to $\dot{q}_{\max} = 5.7\,\mathrm{W/cm^2}$ were measured at the start of the experiments, which is considerably higher than the established literature values in the range of $\dot{q} = 3.1 \ldots 4\,\mathrm{W/cm^2}$ [23–25], but lower than the maximum calculated heat flux in [38] and comparable to [37, 39]. However, these maximum values only occurred for less than one second before the heat flux quickly decreased to about constant values in the range of $\dot{q} = 1.75\,\mathrm{W/cm^2}$ for the time of interest after the opening of the safety

relief valve. This corresponds well with both the shape and the absolute values of the heat flux measured at CEA [37] using a different experimental approach. The shape of the heat flux corresponds also well with [35, 38]. This reduced relevant heat flux has direct implications on the discharge mass flow rate and hence on the required discharge area. Following the common design codes for the sizing [17, 21], the consideration of the process dynamics leads to a considerable reduction of the discharge area by up to 50 %. Benefits are reduced acquisition costs, space requirements and helium leakage as well as a more reliable operation of safety relief devices. However, more experiments are needed to confirm these findings.

The reproducibility of the experimental results was shown for medium loss of insulating vacuum, which gives confidence in the experimental method. The comparison between experiments conducted with different venting fluids showed that gaseous nitrogen from a buffer vessel can be used to replace atmospheric air in experiments with MLI, if enough nitrogen can be supplied in the buffer throughout the experiment.

The experimental results emphasized the necessity of modelling the process dynamics during loss of insulating vacuum. The original dynamic model [16] based on differential equations linking the major time-dependent sub-processes was refined especially with respect to the heat and mass transfer at the cryogenic vessel wall as explained in Chapter 5. Through fitting of the measured average wall temperature as a function of the average helium temperature, a simplified overall heat transfer resistance was included in the model for major, medium and minor loss of vacuum, respectively. Based on the *Hertz-Knudsen equation*, the influence of the desublimation/condensation and simultaneous sublimation/evaporation of the venting fluid deposited at the cryogenic vessel wall was included in the refined model based on literature data of the sticking probability of gas molecules. By including an additional transmission factor, the influence of PICARD's specific design on the probability of gas molecules reaching the cold surface was considered and can be adapted to the design of other test facilities. Besides, the temperature increase of the cryogenic vessel wall was considered that reduces the heat flux transferred to the cryogenic fluid. Furthermore, the non-ideal venting process into the vacuum space through the venting orifice was added to refine the original model.

The refined model was compared to the experimental results for major, medium and minor loss of insulating vacuum. With regard to the results of model calculations based on the original model, great improvement concerning both the evolution and the absolute values of the time-dependent processes was achieved. Based on the kinetic theory used for the modelling of the mass transfer, the particular shape of the measured heat flux evolution could be well explained, which gives confidence in the refined model and the method for calculating the heat flux from experimental data. However, the presented refined dynamic model can only be an intermediate step towards a generally valid model as it includes the fitting of the wall temperature to experimental values and is therefore dependent on experimental input data. In order to generalize the model, the study of the observed inequality between the heat flux caused by deposition of the venting fluid and the heat flux transferred to the helium should be the focus of future studies. Hence, the refined model developed in the course of this work is a significant improvement on the previous state of the art with considerable scope for

further generalizations on the basis of a broader range of experimental data in the future.

In conclusion, the results of the experiments and of the modelling presented in this work provide an improved understanding of the process dynamics during LIV. The new cryogenic test facility PICARD offers the potential for a wide range of experimental studies as a basis for further conceptual developments as well as applications in the field of cryogenic safety research.

CHAPTER 7

Outlook

This work contributes to the continuing effort to improve cryogenic safety relief systems in the context of the ongoing German and European standardization efforts in the field of cryogenic safety. First experimental results already showed the significance of the experimental investigation of the loss of insulating vacuum in liquid helium cryostats. In order to further broaden the dataset and investigate measures to avoid unstable operation of safety relief devices, more experiments under variation of the experimental conditions are required. These could include, but are not limited to:

- experiments with smaller safety relief valves sized based on the reduced heat flux observed at the time of interest to avoid chattering,
- repetition of experiments to have a larger dataset for calculating Type A measurement uncertainties,
- experiments with MLI to investigate the influence of the number of layers and the winding method,
- investigation of measures to reduce the risk of chattering, including
  - experiments using a control valve as relief device and other alternatives to spring-loaded safety relief valves
  - experiments where e.g. a magnet is used to hold the spindle of the safety relief valve in order to mechanically keep the valve open for some seconds after the first opening,
  - experiments with a safety relief valve having a reduced reseating pressure to allow the pressure to decrease e.g. due to pressure losses during discharge without the safety relief valve closing too early,
  - experiments with a larger diameter upstream of the safety relief valve for a reduction of the pressure losses at the inlet of the valve,

- investigation of the occurrence and effects of two-phase flow through
  - experiments with set pressures close to the critical point and
  - experiments with varying initial liquid level,
- experiments with larger venting orifices to prevent the initial delay in the vacuum pressure increase and thus to determine whether $\dot{q} = 5.7\,\mathrm{W/cm^2}$ is the maximum possible heat flux during loss of insulating vacuum,
- experiments with smaller heat fluxes to simulate small leaks in the vacuum vessel,
- experiments with other cryogenic fluids such as liquid nitrogen or argon,
- investigation of other failure modes such as
  - experiments simulating the rupture of the cryogenic vessel by venting the insulating vacuum with liquid cryogenic fluid through a rupture disk installed at the cryogenic vessel,
  - experiments with a simulated (additional) sc. magnet quench, e.g. by adding heaters to a copper block inside the cryogenic vessel,
  - experiments with liquid nitrogen as venting fluid to simulate the leak of a nitrogen shield.

In order to improve the quality of the experimental data, faster pressure sensors especially for the measurement of the venting mass flow rate and the pressure inside the cryogenic vessel should be installed at PICARD. For experiments with gaseous nitrogen or other venting fluids, the buffer should be optimized, for instance by using a larger buffer vessel or a balloon in order to achieve buffer pressures closer to ambient pressure during the entire experiment. Besides this, experiments without or with a modified radiation shield could be conducted in order to investigate the influence of the radiation shield design on the process dynamics. In the course of this, liquid nitrogen pipes could be added to the radiation shield to conduct experiments with a nitrogen-cooled shield as it is often used in liquid helium cryostats. Furthermore, a small camera and a capacitive measurement could be installed to investigate the thickness, condition and distribution of the deposited venting fluid at the surface of the cryogenic vessel.

For a better understanding of the opening characteristics of cryogenic safety relief valves, further investigation of the adjustment methods is required, eventually leading to the definition of a universally and explicitly defined standard setting method. This could include the study of the influence of the process dynamics, the type and the temperature of the gas used for the setting and the type of safety relief valve.

In order to further improve the dynamic model, targeted experiments of the desublimation process of air and nitrogen especially at wall temperatures in the range between 20 K and the triple point of the venting fluid are required. To improve the evaluation of the heat flux and reduce the measurement uncertainty, the venting fluid enthalpy should be adjusted to include all humid air components. Therefore, fluid property data for oxygen and water below the triple point should be collected through systematic experiments.

For a generalization of the model, the prediction of the process parameters independent of experimentally obtained input data is of great importance. Therefore, the wall temperature increase could be modelled based on the observed inequality between the heat flux caused by desublimation of the venting fluid and the heat flux transferred to the cryogenic fluid. The calculation of the heat flux transmitted to the cryogenic fluid has not yet been included in the model. First experimental data indicate the heat transfer to the helium as limiting factor for major LIV, while the heat transfer during minor LIV is limited by the desublimation and condensation of the venting fluid at the cold surface. The detailed modelling of these processes would thus render the fitting of the wall temperature to experimental data unnecessary. Targeted flow experiments at room temperature using different venting sections and initial vacuum pressures would be beneficial to generalize the determination of the flow rate coefficient and to improve the accuracy of the predicted venting mass flow rate and thus of the heat flux prediction, eventually leading to a reliable method for dimensioning cryogenic safety relief devices. As a long-term aim, a comprehensive European standard tailored to the safety of liquid helium cryostats with a homogenized nomenclature would be highly beneficial.

APPENDIX A

Additional information on the data evaluation

A.1 Calculation of the heat flux in literature

Depending on the test setup and the experimental conditions, different approaches for calculating the heat flux during the venting of the insulating vacuum of a liquid helium cryostat can be found in literature. In this section, selected approaches are presented and discussed.

Lehmann and Zahn [23] use a cryostat that is not equipped with a safety relief device, but opens directly to atmosphere. They calculate the heat flux $\dot{q}_{\mathrm{Lehmann}}$ based on the evaporation of helium at ambient pressure as

$$\dot{q}_{\mathrm{Lehmann}} = \dot{m}_{\mathrm{v}} \cdot \Delta h_{\mathrm{v}} \tag{A.1}$$

with the helium evaporation mass flow rate $\dot{m}_{\mathrm{v}}$ and the enthalpy of evaporation Δh_{v}. As helium is released through a safety relief device at pressures above ambient pressure at PICARD, the method used in [23] cannot be used for the evaluation of the dataset in this work.

Harrison [25] and Ercolani et al. [37] both calculate the heat flux from the changing fluid property data of helium. The heat input $\dot{Q}_{\mathrm{Harrison}}$ is estimated for the closed cryogenic vessel from the change in internal energy of the helium, i.e. from the temperature and pressure increase inside the cryogenic vessel as

$$\dot{Q}_{\mathrm{Harrison}} = \frac{\mathrm{d}U_{\mathrm{He}}\left(p_{\mathrm{He}}, T_{\mathrm{He}}\right)}{\mathrm{d}\tau}\,, \tag{A.2}$$

with the internal energy U_{He}. For the venting process, the heat input is calculated based on the first law of thermodynamics as

$$\dot{Q}_{\mathrm{Harrison}} = c_{v,\mathrm{He}} \cdot \frac{\mathrm{d}(m_{\mathrm{He}} \cdot T_{\mathrm{He}})}{\mathrm{d}\tau} + \dot{m}_{\mathrm{Out}} \cdot \left(h_{\mathrm{He}} + \frac{w_{\mathrm{Out}}^2}{2}\right)\,, \tag{A.3}$$

where $m_{\mathrm{He}}, T_{\mathrm{He}}, c_{v,\mathrm{He}}$ and h_{He} are the helium mass, temperature, specific heat capacity and specific enthalpy, and $\dot{m}_{\mathrm{Out}}$ and w_{Out} are the mass flow rate and velocity of the discharged helium calculated using compressible flow equations for isentropic expansion into atmosphere [25]. In [25], the temperature is only measured by two temperature sensors and the liquid and vapour phase are treated separately with the liquid at the average temperature of the two sensors and the vapour at saturation temperature, thus assuming thermal equilibrium. Although a considerable stratification in the helium temperature is observed during the experiments in [25], no estimation of the resulting uncertainties is given.

Ercolani et al. [37] estimate the heat flux $\dot{q}_{\mathrm{Ercolani}}$ for discrete time steps only during isochoric pressure increase based on the first law of thermodynamics as

$$\dot{q}_{\mathrm{Ercolani}} = \rho_{\mathrm{He},0} \cdot \frac{V_{\mathrm{Cr}}}{A_{\mathrm{Cr}}} \cdot \frac{\Delta U_{\mathrm{He}}}{\Delta \tau} \,, \tag{A.4}$$

with the initial helium density $\rho_{\mathrm{He},0}$, the volume and surface of the cryogenic vessel V_{Cr} and A_{Cr} and the change in internal energy ΔU_{He} during the time step $\Delta\tau$ with

$$\Delta U_{\mathrm{He}} = U_{\mathrm{He,end}}\left(p_{\mathrm{He,end}}, \rho_{\mathrm{He,end}}\right) - U_{\mathrm{He},0}\left(p_{\mathrm{He},0}, \rho_{\mathrm{He},0}\right) \,, \tag{A.5}$$

using time steps of about 1/12 s. In [37], the helium temperature is measured with ten sensors at three different locations inside the cryogenic vessel. The change in internal energy is calculated for each location and combined to a total change of internal energy. Both Harrison [25] and Ercolani et al. [37] use small cryogenic vessels with a liquid helium volume of only 12 L and 10 L, respectively. Therefore, the temperature gradients within the cryogenic vessel are much smaller compared to this work where a liquid helium volume of up to 100 L is used. Especially during unstable operation of the safety relief valve, the fast changes in the internal energy (caused by the fast changes in pressure and temperature) and the thermodynamic non-equilibrium during this dynamic process render the derivative not representable for the general trend in this work. Therefore, this method is found inadequate for the calculation of the heat flux with the PICARD test setup.

Dhuley and Van Sciver [38, 39, 80–82] use a special test setup to investigate the propagation of nitrogen gas in long vacuum tubes surrounded by liquid helium such as used in particle accelerators. In [39], the heat flux caused by deposition of nitrogen is estimated from the mass of nitrogen $m_{\mathrm{N2,s}}$ solidified on the tube surface A_{Tube} and the associated enthalpy change as

$$\dot{q}_{\mathrm{Dep,Dhuley,1}} = \frac{1}{A_{\mathrm{Tube}}} \frac{\mathrm{d}m_{\mathrm{N2,s}}}{\mathrm{d}\tau} \cdot \left(h_{\mathrm{N2,g}} - h_{\mathrm{N2,s}}\right) \,, \tag{A.6}$$

with the enthalpies $h_{\mathrm{N2,g}}$ and $h_{\mathrm{N2,s}}$ of gaseous and solid nitrogen. The deposited mass is estimated from the vacuum pressure data, yielding an average deposition heat flux of 6 W/cm^2 [39]. In [38, 39], Dhuley and Van Sciver estimate the heat flux to liquid helium $\dot{q}_{\mathrm{LHe,Dhuley}}$ assuming nucleate boiling by interpolation of the heat transfer rates from [83] for the temperature difference between the liquid helium and the wall. From

this, the deposition heat transfer rate $\dot{q}_{\mathrm{Dep,Dhuley,2}}$ is estimated in a different approach presented in [38] considering the heat conduction along the tube in direction of the propagating air for the first few seconds of the venting process as

$$\dot{q}_{\mathrm{Dep,Dhuley,2}} = \frac{d_\mathrm{o}^2 - d_\mathrm{i}^2}{4\ d_\mathrm{i}} \cdot \left(\rho_\mathrm{Tube} \cdot c_\mathrm{Tube} \cdot \frac{\mathrm{d}T}{\mathrm{d}\tau} - \frac{\mathrm{d}}{\mathrm{d}x} \left[\lambda_\mathrm{Tube} \cdot \frac{\mathrm{d}T}{\mathrm{d}x} \right] \right) + \frac{d_\mathrm{o}}{d_\mathrm{i}} \cdot \dot{q}_\mathrm{LHe,Dhuley} \quad \text{(A.7)}$$

where d_o and d_i are the outer and inner tube diameter, x is the coordinate along the tube, and ρ_Tube, c_Tube and λ_Tube are the density, heat capacity and thermal conductivity of the tube material, respectively. This second method yields considerably higher maximum deposition heat fluxes of up to $40\,\mathrm{W/cm^2}$ [38]. The experimental conditions in [38,39,80–82] are very different from this work, where the venting fluid vents against the whole surface of a cryogenic vessel located inside a vacuum vessel.

Similar to [39], Cavallari et al. [24] estimate the initial heat load $\dot{Q}_{\mathrm{Dep,Cavallari}}$ for complete cryopumping of air at the cold surface of the cryogenic vessel and the change in enthalpy during the process as

$$\dot{Q}_{\mathrm{Dep,Cavallari}} = \frac{\Delta m_{\mathrm{Air,s}}}{\Delta \tau} \cdot \left(h_{\mathrm{Air,g}} - h_{\mathrm{Air,s}} \right) . \quad \text{(A.8)}$$

The desublimated mass of air $\Delta m_{\mathrm{Air,s}}$ is estimated from the difference between the inflowing air at a constant rate for vacuum pressures below 50 % of ambient pressure and the air contributing to the vacuum pressure increase [24]. The test setup in [24] is equipped with only a few sensors. For instance, the surface temperature of the cryogenic vessel wall is not measured, but the vacuum pressure is assumed to be the vapour pressure of the gas-solid interface or the gas-liquid-interface, thus assuming thermodynamic equilibrium and a homogeneous surface temperature profile. The temperature of the air remaining in the vacuum space after the start of the venting processes is assumed to be at a mean temperature between room temperature and the saturation temperature of air at the surface of the cryogenic vessel. Besides, the sampling interval of 1 s would be too slow to record peak heat loads lasting only for few milliseconds. Furthermore, Cavallari et al. [24] assume an intermediate temperature $T_{\mathrm{V,Cavallari}}$ of the air inside the vacuum space as

$$T_{\mathrm{V,Cavallari}} = \frac{T_\mathrm{A} + T_\mathrm{W}}{2} , \quad \text{(A.9)}$$

with the ambient temperature T_A and the wall temperature T_W. Thus, smaller heat fluxes especially in the beginning of the venting process are calculated in [24] than with the conservative assumption of $T_\mathrm{V} = T_\mathrm{A}$ used in this work, where a similar method for estimating the heat flux is used.

A.2 Calculation of the heat flux based on humid air enthalpies

Humid air is a mixture of nitrogen, oxygen, argon, water and traces of other components. The mole content of water in humid air y_{H2O} is determined at PICARD from the measured relative humidity MI31 as

$$y_{\mathrm{H2O}} = p_{\mathrm{Sat,H2O}}(\mathrm{TI31}) \cdot \mathrm{MI31}\,, \tag{A.10}$$

with the saturation pressure of water $p_{\mathrm{Sat,H2O}}$ at ambient temperature TI31. Dry air is a mixture of about $\zeta_{\mathrm{N2}} = 78.12\,\mathrm{mol\%}$ nitrogen, $\zeta_{\mathrm{O2}} = 20.96\,\mathrm{mol\%}$ of oxygen and $\zeta_{\mathrm{Ar}} = 0.92\,\mathrm{mol\%}$ of argon [13]. Thus, the molar concentrations y_i of the components $i = \{\text{nitrogen, oxygen, argon, water}\}$ can be calculated as

$$y_i = (1 - y_{\mathrm{H2O}}) \cdot \zeta_i\,. \tag{A.11}$$

As a first approximation, the assumption of an ideal gas mixture with the specific heat of monatomic gas $c_{p,\mathrm{Ar}} = 5/2 \cdot \mathrm{R}$, of two-atomic molecules $c_{p,\mathrm{N2}} = c_{p,\mathrm{O2}} = 7/2 \cdot \mathrm{R}$ and of three-atomic rigid molecules $c_{p,\mathrm{H2O}} = 8/2 \cdot \mathrm{R}$ with the universal gas constant R can be made. Consequently, the sensible enthalpy difference of the component i $\Delta h_{\mathrm{Sens,i}}$ between ambient temperature TI31 and the average wall temperature $\bar{T}_{\mathrm{W}}$ is estimated to

$$\Delta h_{\mathrm{Sens},i} = c_{p,i} \cdot (\mathrm{TI31} - T_{\mathrm{W}})\,. \tag{A.12}$$

Thus, the total enthalpy difference of humid air Δh_{ha} is calculated as

$$\Delta h_{\mathrm{ha}} = \begin{cases} \sum_i \left(M_i \cdot y_i \cdot \left[\Delta h_{\mathrm{Sens},i}(\mathrm{TI31}, \bar{T}_{\mathrm{W}}) + \Delta h_{\mathrm{Sub},i} \right] \right) & \bar{T}_{\mathrm{W}} > T_{\mathrm{Trip},i} \\ \sum_i \left(M_i \cdot y_i \cdot \Delta h_{\mathrm{Sens},i}(\mathrm{TI31}, \bar{T}_{\mathrm{W}}) \right) & \bar{T}_{\mathrm{W}} \leq T_{\mathrm{Trip},i} \end{cases} \tag{A.13}$$

with the molar masses M_i, the sublimation enthalpies $\Delta h_{\mathrm{Sub},i}$ given in Haefer [74] as

$$\Delta h_{\mathrm{Sub},i} = \begin{cases} 7364\,\mathrm{kJ/kmol} & i = \text{nitrogen} \\ 9178\,\mathrm{kJ/kmol} & i = \text{oxygen} \\ 8047\,\mathrm{kJ/kmol} & i = \text{argon} \\ 50680\,\mathrm{kJ/kmol} & i = \text{water} \end{cases} \tag{A.14}$$

and neglecting all enthalpy changes of the fluids below the triple point. Following this calculation, the difference between Δh_{ha} of humid air and Δh_{N2} of pure nitrogen is below 10 %.

A.3 Exemplary calculation of measurement uncertainties

Based on GUM [63], the combined measurement uncertainty u_C for each temperature data point T_i in this work is calculated following

$$u_\mathrm{C}(T_i) = \sqrt{u_\mathrm{Cal,T}(T_i)^2 + u_\mathrm{DAQ,T}(T_i)^2 + u_\mathrm{CS}(T_i)^2}\,, \tag{A.15}$$

with the calibration uncertainty $u_\mathrm{Cal,T}$, the uncertainty of the data acquisition system $u_\mathrm{DAQ,T}$ and the uncertainty of the current source u_CS. The uncertainty $u_\mathrm{Cal,T}$ is given by the calibration laboratory as

$$u^2_\mathrm{Cal}(T_i) = \frac{(0.01 \cdot T_i)^2}{3}\,. \tag{A.16}$$

Assuming a symmetric rectangular distribution, $u_\mathrm{DAQ,T}$ is calculated as

$$u^2_\mathrm{DAQ,T}(T_i) = \frac{[a_\mathrm{h,DAQ,T}(T_i)]^2}{3}\,, \tag{A.17}$$

with the half-width $a_\mathrm{h,DAQ,T}$ calculated based on the data of the measurement card NI 9205 provided by *National Instruments* as

$$a_\mathrm{h,DAQ,T}(T_i) = U_{\mathrm{T_i}} \cdot 10^{-6} + 0.2 \cdot 278 \cdot 10^{-6}\,\mathrm{V} + 3 \cdot 10^{-6}\,\mathrm{V}\,, \tag{A.18}$$

with the voltage U_T measured as raw data of the TVO sensor. Assuming again a symmetric rectangular distribution, u_CS of the current source is calculated as

$$u^2_\mathrm{CS}(T_i) = \frac{[a_\mathrm{h,CS}(T_i)]^2}{3}\,, \tag{A.19}$$

with the half-width $a_\mathrm{h,CS}$ calculated from the data of the current source type 6221 provided by *Keithley*

$$a_\mathrm{h,CS}(T_i) = \frac{U_\mathrm{T}(T_i) \cdot (0.05 \cdot 10^{-2} \cdot 30 \cdot 10^{-6} + 100 \cdot 10^{-9} + 3 \cdot 10^{-6})}{30 \cdot 10^{-6} \cdot S_\mathrm{T}(T_i) \cdot (-1)} \tag{A.20}$$

that depends on the sensitivity of the temperature sensor S_T, which is defined as the change of resistivity R_T with temperature,

$$S_\mathrm{T}(T_i) = \frac{\mathrm{d}R_\mathrm{T}(T_i)}{\mathrm{d}T}\,. \tag{A.21}$$

Because TVO sensors have a temperature-dependent electric resistivity with a negative temperature coefficient, the factor (-1) is necessary in Eq. (A.20). The uncertainties caused by cabling, calibration polynomial approximation, long-term stability, self-heating and mounting have been neglected since their impact was found to be in the range of $\leq 0.5\,\%$ of the overall uncertainty, respectively [64]. Exemplary for TI13,

Table A.1: List of the main contributions to the Type B measurement uncertainty for the temperature measurement chain of TI13 operated with a supply current of 30 μA assuming a rectangular distribution.

T	$u_{\mathrm{Cal,T}}$	$u_{\mathrm{DAQ,T}}$	u_{CS}	$u_{\mathrm{C,T}}$
K	K	K	K	K
4.2	$2.4 \cdot 10^{-2}$	$3.8 \cdot 10^{-3}$	$1.0 \cdot 10^{-5}$	$2.5 \cdot 10^{-2}$
20	$1.2 \cdot 10^{-1}$	$7.1 \cdot 10^{-2}$	$1.3 \cdot 10^{-4}$	$1.4 \cdot 10^{-1}$
40	$2.3 \cdot 10^{-1}$	$1.9 \cdot 10^{-1}$	$3.1 \cdot 10^{-4}$	$3.0 \cdot 10^{-1}$
80	$4.6 \cdot 10^{-1}$	$4.4 \cdot 10^{-1}$	$6.5 \cdot 10^{-4}$	$6.4 \cdot 10^{-1}$
270	1.6	1.9	$2.4 \cdot 10^{-3}$	2.5

Table A.2: Maximum deviations of the pressure transducers calibrated by *Wika*.

Transducer	b_{pos} in % of the measured value	b_{neg} in % of the measured value
PI12	+0.28	−0.00
PDI11	+0.03	−0.00
PDI31	+0.08	−0.04

typical measurement uncertainties of the measurement chain are shown in Table A.1.

Equivalently to the temperature measurement, the combined measurement uncertainty $u_{\mathrm{C,p}}$ for each pressure data point p_i is calculated according to GUM [63] as

$$u_{\mathrm{C,p}}(p_i) = \sqrt{u_{\mathrm{Cal,p}}(p_i)^2 + u_{\mathrm{DAQ,p}}(p_i)^2 + u_{\mathrm{Iso}}(p_i)^2}\,, \tag{A.22}$$

including the calibration uncertainty $u_{\mathrm{Cal,p}}$, the uncertainty by the measurement card of type NI 9203 $u_{\mathrm{DAQ,p}}$ and the uncertainty of the supply isolators u_{Iso}. The conservatively estimated calibration uncertainty $u_{\mathrm{Cal,p}}$ is based on the maximum positive and negative relative deviations b_{pos} and b_{neg} provided by *Wika* as

$$u^2_{\mathrm{Cal}}(p_i) = \frac{\left[b_{\mathrm{pos}} \cdot p_i + b_{\mathrm{neg}} \cdot p_i\right]^2}{12}\,. \tag{A.23}$$

The values of b_{pos} and b_{neg} can be found in Table A.2. The uncertainty $u_{\mathrm{DAQ,p}}$ is defined as

$$u^2_{\mathrm{DAQ,p}}(p_i) = \frac{\left[a_{\mathrm{h,DAQ,p}}(p_i)\right]^2}{3}\,, \tag{A.24}$$

with the half-width $a_{\mathrm{h,DAQ,p}}$, in case of for instance PI12

$$a_{\mathrm{h,DAQ,PI12}}(p_i) = \frac{0.54\,\% \cdot 21.5\,\mathrm{mA} + 0.66\,\% \cdot I_{\mathrm{p}}(p_i)}{S_{\mathrm{p}}(p_i)}\,, \tag{A.25}$$

Table A.3: List of the main contributions to the Type B measurement uncertainty for the measurement chain of PI12 assuming a rectangular distribution.

p bar(g)	$u_{\mathrm{Cal,p}}$ bar(g)	$u_{\mathrm{DAQ,p}}$ bar(g)	u_{Sep} bar(g)	$u_{\mathrm{C,p}}$ bar(g)
0	0.0	$1.3 \cdot 10^{-1}$	$2.6 \cdot 10^{-2}$	$1.3 \cdot 10^{-1}$
2	$1.6 \cdot 10^{-3}$	$1.4 \cdot 10^{-1}$	$2.6 \cdot 10^{-2}$	$1.4 \cdot 10^{-1}$
6	$4.9 \cdot 10^{-3}$	$1.5 \cdot 10^{-1}$	$2.6 \cdot 10^{-2}$	$1.5 \cdot 10^{-1}$
8	$6.5 \cdot 10^{-3}$	$2.2 \cdot 10^{-1}$	$2.6 \cdot 10^{-2}$	$1.6 \cdot 10^{-1}$

Table A.4: Calibration coefficients of the orifice measurement section for the three differently sized orifices by *TetraTec* used in the PICARD test setup.

d_{Or} mm	C_{A} $\mathrm{mbar}^{0.5}$	C_{B} –	C_{C} $\mathrm{mbar}^{-0.5}$	C_{D} mbar^{-1}	C_{E} $\mathrm{mbar}^{-1.5}$
12.5	$3.760724 \cdot 10^{5}$	$-3.279373 \cdot 10^{3}$	$2.549724 \cdot 10^{2}$	$-1.724653 \cdot 10$	$2.762988 \cdot 10^{-1}$
25	$4.074262 \cdot 10^{5}$	$-3.088849 \cdot 10^{3}$	$1.747029 \cdot 10^{2}$	$-1.294357 \cdot 10$	$1.566099 \cdot 10^{-1}$
30	$4.381178 \cdot 10^{5}$	$-2.424191 \cdot 10^{3}$	$1.011681 \cdot 10^{2}$	$-1.344474 \cdot 10$	$2.157243 \cdot 10^{-1}$

including the sensitivity of the pressure transmitter S_{p} and the raw data of the pressure measurement I_{p}. The uncertainty of the supply isolators from *Wago* used for HART communication u_{Iso} is defined as

$$u^2_{\mathrm{ISO}}(p_i) = \frac{1}{3} \cdot \frac{(a^2_{\mathrm{h,Offset}} + a^2_{\mathrm{h,Trans}})}{S_{\mathrm{p}}(p_i)^2}\,, \tag{A.26}$$

including the offset half-width $a_{\mathrm{h,Offset}} = 20\,\mu\mathrm{A}$ as well as the transmission half-width $a_{\mathrm{h,Trans}} = 0.1\,\% \cdot 20\,\mathrm{mA}$. The measurement uncertainties of the measurement chain for the exemplary pressure transmitter PI12 are shown in Table A.3.

The calibration coefficients of the three orifices used for measuring the venting mass flow rate are listed in Table A.4.

APPENDIX B

Additional information on the refined dynamic model

B.1 Determination of the transmission coefficient

The transmission coefficient α_{T} introduced in Subsection 5.1.3 for the PICARD setup has been determined through a parameter study comparing the measured and the modelled vacuum pressure increase. As can be seen in Figure B.1 exemplary for major and minor LIV, the curves of the modelled vacuum pressure increase show the best correspondence with the measured values for $\alpha_{\mathrm{T}} = 3 \cdot 10^{-2}$, especially during the first second after the start of the experiments. Nevertheless, a detailed study based on a broader set of data could further refine the definition of α_{T}. A detailed discussion of the modelled vacuum pressure increase can be found in Subsection 5.2.1.

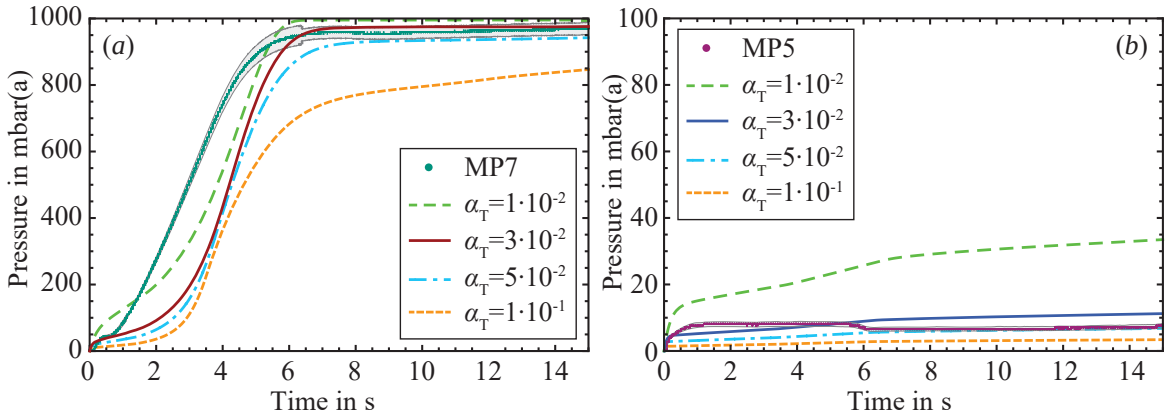

Figure B.1: Measured vacuum pressure with the corresponding measurement uncertainty displayed in light grey during (*a*) major LIV (MP7) and (*b*) minor LIV (MP5) in comparison to the results of the model calculations for different transmission coefficients α_T.

B.2 Determination of the venting coefficient

Figure B.2 shows the comparison between the measured venting mass flow rate during major and minor LIV in comparison to the predicted venting mass flow rate calculated with the refined model for the flow rate coefficients $K_{\text{Vent}} = 1$ and $K_{\text{Vent}} = 0.85$ chosen for the model presented in this work. As explained in Subsection 5.1.4, the flow rate coefficient K_{Vent} is defined as the ratio between the measured venting mass flow rate $\dot{m}_{\text{In,measured}}$ based on the calibration polynomial shown in Eq. (3.3) and the mass flow rate through an ideal nozzle $\dot{m}_{\text{In,ideal}}$ based on Eq. (2.13), calculated with the temperatures and pressures measured at the start of the experiment ($\tau = 0$) as

$$\dot{m}_{\text{In,measured}} = \frac{\pi}{4} \cdot d_{\text{Or}}^2 \cdot \sqrt{2 \cdot \rho_{\text{V,Strd}} \cdot \frac{\text{PI22[0]}}{p_{\text{Strd}}} \cdot \frac{T_{\text{Strd}}}{\text{TI31[0]}}} \cdot \left(C_{\text{A}} \cdot \Delta p_{\text{Or}}^{0.5} + C_{\text{B}} \cdot \Delta p_{\text{Or}} + C_{\text{C}} \cdot \Delta p_{\text{Or}}^{1.5} + C_{\text{D}} \cdot \Delta p_{\text{Or}}^2 + C_{\text{E}} \cdot \Delta p_{\text{Or}}^{2.5} \right) , \tag{B.1}$$

with $\Delta p_{\text{Or}} = (\text{PI32[0]} - \text{PI22[0]})$ and

$$\dot{m}_{\text{In,ideal}} = \frac{\pi}{4} \cdot d_{\text{Or}}^2 \cdot \sqrt{2 \cdot \text{PI32[0]} \cdot \rho_{\text{A}}(\text{PI32[0]}, \text{TI31[0]})} \left(\frac{2}{\kappa_{\text{V}} + 1} \right)^{\frac{1}{\kappa_{\text{V}} - 1}} \cdot \sqrt{\frac{\kappa_{\text{V}}}{\kappa_{\text{V}} + 1}} \tag{B.2}$$

for critical flow conditions. For MP7, $K_{\text{Vent,MP7}}(\tau = 0) = 0.85$ was calculated, while $K_{\text{Vent,MP5}}(\tau = 0) = 0.86$ was derived for MP5 with the input parameters listed in Table B.1.

As can be seen in Figure B.2, the modelled venting mass flow rate calculated according to Eq. 5.19 with $K_{\text{Vent}} = 1$ is considerably higher than the measured mass flow rate, while the modelled venting mass flow rate calculated with $K_{\text{Vent}} = 0.85$ is close to the measured values for both major LIV (MP7) and minor LIV (MP5). However, as

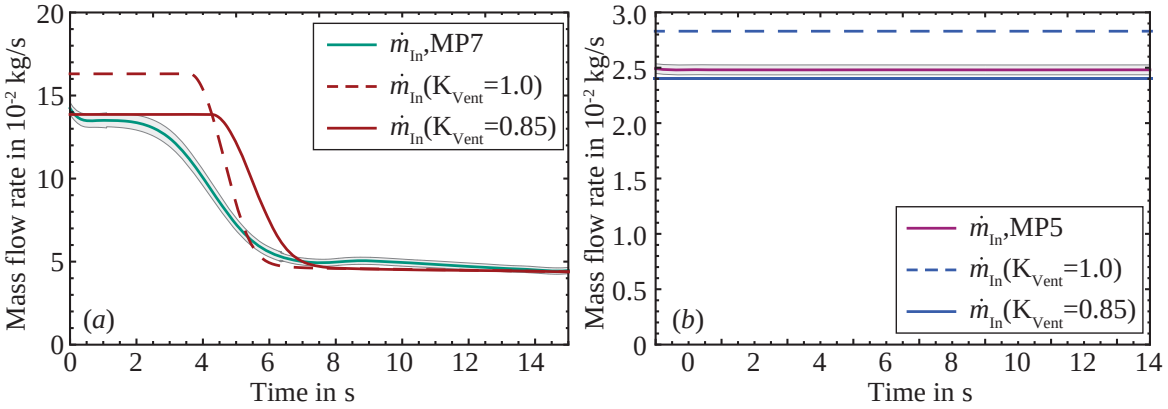

Figure B.2: Measured venting mass flow rate during (a) major LIV (MP7) and (b) minor LIV (MP5) in comparison to the results of the model calculations for different flow rate coefficients K_{Vent}.

Table B.1: Experimental results of MP7 (major LIV) and MP5 (minor LIV) at the beginning of the experiment ($\tau = 0$) as input parameters for the calculation of K_{Vent}.

Parameter	Symbol in P%ID	MP7	MP5
Ambient Temperature	TI31	K	K
Ambient Pressure	PI32	bar(a)	bar(a)
Vacuum Pressure	PI22	mbar(a)	mbar(a)

the predicted venting mass flow rate during major LIV is in the constant and supercritical range for about two seconds longer than measured during the experiment, a more detailed study of the venting process could help to improve the accuracy of the model. Furthermore, the thus found venting coefficient is only valid for the venting section at PICARD. For the further generalization of the model, experiments with different venting sections would be beneficial. One option could be venting experiments at room temperature under variation of the initial vacuum pressures and the venting section.

APPENDIX C

Data sheets of PICARD sensors and apparatus

C.1 Pressure sensors

Technical Data	PCR 280, 80 °C, DN 16 ISO-KF
Accuracy: $1 \cdot 10^{-3}$ – 100 hPa	± 15 %
Accuracy: 100 – 950 hPa	± 5 %
Accuracy: $5 \cdot 10^{-4}$ – $1 \cdot 10^{-3}$ hPa	± 50 %
Accuracy: 950 – 1050 hPa	± 2.5 %
Bakeout temperature	80 °C
Feature	Stainless steel, metal sealed
Feedthrough	Glass
Filament	Tungsten
Flange, Material	Stainless steel
Measurement range max.	$1.5 \cdot 10^{3}$ hPa | $1.12 \cdot 10^{3}$ Torr | $1.5 \cdot 10^{3}$ mbar
Measurement range min.	$5 \cdot 10^{-5}$ hPa | $3.75 \cdot 10^{-5}$ Torr | $5 \cdot 10^{-5}$ mbar
Method of measurement	Pirani/Capacitance
Nominal diameter	DN 16 ISO-KF
Output signal: Measurement range	1.2 – 8.68 V
Output signal: Minimum load	10 kΩ
Repeatability: $1 \cdot 10^{-3}$ – 1100 hPa	± 2 %
Seal	Metal
Supply: Power consumption max.	2.5 W
Supply: Voltage	15 – 30 V DC
Temperature: Operating	10-50 °C | 50-122 °F | 283-323 K
Temperature: Storage	-20-65 °C | -4-149 °F | 253-338 K
Volume	4.7 cm^3
Weight	120 g

Figure C.1: Extract from the data sheet of the vacuum pressure transducer PI22 of type *PCR280*, with kind support of the *Pfeiffer Vacuum GmbH* [84].

Technical Data	PKR 251, FPM sealed, DN 25 ISO-KF
Accuracy: $1 \cdot 10^{-8}$ – $1 \cdot 100$ hPa	± 30 %
Anode	Molybdenum
Bakeout temperature	Electronic removed, ≤ 150 °C
Feature	Interior FPM sealed
Feedthrough	Al_2O_3, Glass
Filament	Tungsten
Flange, Material	Stainless steel
Measurement range	$5 \cdot 10^{-9 - 1E3}$ hPa
Measurement range max.	$1 \cdot 10^{3}$ hPa | $7.5 \cdot 10^{2}$ Torr | $1 \cdot 10^{3}$ mbar
Measurement range min.	$5 \cdot 10^{-9}$ hPa | $3.75 \cdot 10^{-9}$ Torr | $5 \cdot 10^{-9}$ mbar
Method of measurement	Pirani/Cold Cathode
Nominal diameter	DN 25 ISO-KF
Output signal: Measurement range	1.8 – 8.6 V
Output signal: Minimum load	10 kΩ
Pressure max.	10,000 hPa | 7,500 Torr | 10,000 mbar
Repeatability: $1 \cdot 10^{-8}$ – 100 hPa	± 5 %
Seal	FKM
Sensor cable length max.	300 m
Supply: Power consumption max.	2 W
Supply: Voltage	15 – 30 V DC
Temperature: Operating	5-55 °C | 41-131 °F | 278-328 K
Temperature: Storage	-40-65 °C | -40-149 °F | 233-338 K
Volume	20 cm³
Weight	700 g

Figure C.2: Extract from the data sheet of the vacuum pressure transducer PI21 of type *PKR251*, with kind support of the *Pfeiffer Vacuum GmbH* [85].

Abnahmeprüfzeugnis nach EN 10204 - 3.1
Inspection certificate according to EN 10204 - 3.1

WIKA

Seite / *Page* 1 / 2

Kunde: / *Customer:*
KIT Karlsruher Institut für Technology
Hermann-von-Helmholtz-Platz 1
76344 Eggenstein-Leopoldshafen

Zeugnis-Nr. / *Certificate No.* **01972979**

Datum / *Date* **21.05.2015**

Kundenbestellnummer / *Customer Order No.*	**254/20596780/ITEP-KRY0/GFB**	Kunden Artikel-Nr. / *Customer Part. No.*		Bestelldatum / *Order Date*	**07.05.2015**
Auftrags-Nr. / Pos. / *Order No. / Item*	**21715386/1**	Artikel-Nr. / *Part No.*	**7745.20**	Ausgangssignal / *Output signal*	**4 ... 20 mA**
Typ / *Model*	**4302-242**	Seriennummer / *Serial number*	**229173-010**	Anzeigebereich / *Scale range*	**-400 ... 400 mbar rel.**
Klasse / *Class*	**0,1% FS**	Messstellen-Nr. / *Tag No.*			

Referenzgerät / *Reference*
CPC6000 0,01% FS -400 ... 400 mbar rel.
Agilent 34401A ME107

Kalibriernummer / *Calibration No.*
01773706
E 1039

Ergebnis / *Result*

Temperatur / *Temperature* **23 °C +/- 1 K**

Referenz Standard mbar	Prüfling Test Item mbar ↑	Prüfling Test Item mbar ↓	Referenz Standard mA	Prüfling Test Item mA ↑	Prüfling Test Item mA ↓	rel. Abweichung rel. Deviation % ↑	rel. Abweichung rel. Deviation % ↓
-400,000	-399,37	-399,36	4,0000	4,013	4,013	0,08	0,08
-300,000	-299,58	-299,37	6,0000	6,008	6,013	0,05	0,08
-200,000	-199,55	-199,48	8,0000	8,009	8,010	0,06	0,06
-100,000	-99,62	-99,48	10,0000	10,008	10,010	0,05	0,06
0,000	0,33	0,41	12,0000	12,007	12,008	0,04	0,05
100,000	100,24	100,45	14,0000	14,005	14,009	0,03	0,06
200,000	200,23	200,29	16,0000	16,005	16,006	0,03	0,04
300,000	300,08	300,23	18,0000	18,002	18,005	0,01	0,03
400,000	400,00	400,06	20,0000	20,000	20,001	0,00	0,01

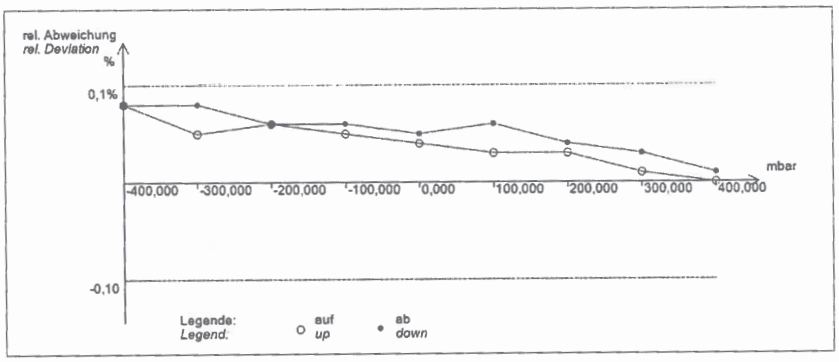

WIKA Alexander Wiegand SE & Co. KG
Alexander-Wiegand-Str. 30
63911 Klingenberg
Germany

Phone: +49 9372 132/0
Fax Inland: +49 9372 132/406
E-Mail: info@wika.de
Internet: www.wika.de

Figure C.3: Calibration data from *Wika* [86] of the differential pressure transducer PDI11 of type *4302* by *Jumo*.

Abnahmeprüfzeugnis nach EN 10204 - 3.1
Inspection certificate according to EN 10204 - 3.1

WIKA

Seite / *Page* 1 / 2

Kunde: / *Customer:*
KIT Karlsruher Institut für Technology
Hermann-von-Helmholtz-Platz 1
76344 Eggenstein-Leopoldshafen

Zeugnis-Nr. / *Certificate No.* **01972983**

Datum / *Date* **19.05.2015**

Kundenbestellnummer / *Customer Order No.*	**Lieferschein 5951**	Kunden Artikel-Nr. / *Customer Part. No.*		Bestelldatum / *Order Date*	**07.05.2015**
Auftrags-Nr. / Pos. / *Order No. / Item*	**21715386/2**	Artikel-Nr. / *Part No.*	**7745.20**	Ausgangssignal / *Output signal*	**4 ... 20 mA**
Typ / *Model*	**HE1150**	Seriennummer / *Serial number*	**[1*]**	Anzeigebereich / *Scale range*	**0 ... 25 bar rel.**
Klasse / *Class*	**0,5% FS**	Messstellen-Nr. / *Tag No.*			

Referenzgerät / *Reference*
CPC8000 0,008% IS-50 -1 ... 25 bar rel.
Agilent 34401A ME59

Kalibriernummer / *Calibration No.*
01797637
E 1056

Ergebnis / *Result*

Temperatur / *Temperature* **23°C +/- 1 K**

Referenz Standard bar	Prüfling Test Item bar ↑	Prüfling Test Item bar ↓	Referenz Standard mA	Prüfling Test Item mA ↑	Prüfling Test Item mA ↓	rel. Abweichung rel. Deviation % ↑	rel. Abweichung rel. Deviation % ↓
0,000	0,00	0,02	4,000	4,00	4,01	0,00	0,08
3,130	3,15	3,16	6,003	6,02	6,02	0,08	0,12
6,250	6,29	6,29	8,000	8,03	8,02	0,16	0,16
9,380	9,44	9,42	10,003	10,04	10,03	0,24	0,16
12,500	12,57	12,54	12,000	12,04	12,03	0,28	0,16
15,630	15,70	15,68	14,003	14,05	14,03	0,28	0,20
18,750	18,81	18,80	16,000	16,04	16,03	0,24	0,20
21,880	21,93	21,92	18,003	18,04	18,03	0,20	0,16
25,000	25,03	25,02	20,000	20,02	20,01	0,12	0,08

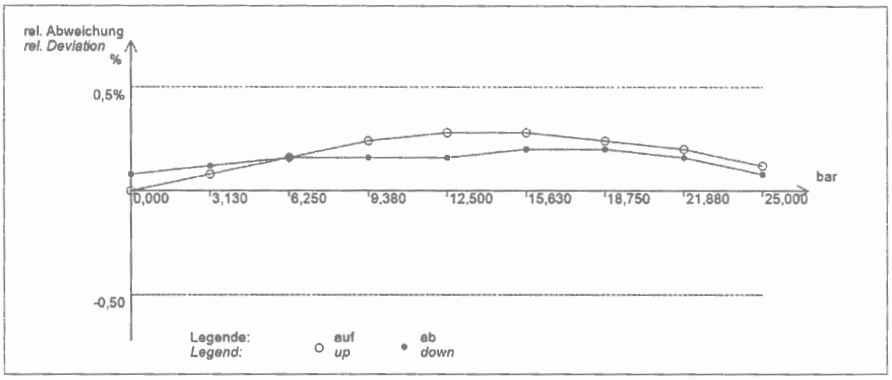

WIKA Alexander Wiegand SE & Co. KG
Alexander-Wiegand-Str. 30
63911 Klingenberg
Germany

Phone: +49 9372 132/0
Fax Inland: +49 9372 132/406
E-Mail: info@wika.de
Internet: www.wika.de

Figure C.4: Calibration data from *Wika* [86] of the pressure transducer PI12 of type *HE 1150* by *Hesch*.

Abnahmeprüfzeugnis nach EN 10204 - 3.1
Inspection certificate according to EN 10204 - 3.1

WIKA

Seite / *Page* 1 / 2

Kunde: / *Customer:* **KIT Karlsruher Institut für Technology, Hermann-von-Helmholtz-Platz 1, 76344 Eggenstein-Leopoldshafen**

Zeugnis-Nr. / *Certificate No.* **01972984**

Datum / *Date* **20.05.2015**

Kundenbestellnummer / *Customer Order No.*	**254/20596780/ITEP-KRY0/GFB**	Kunden Artikel-Nr. / *Customer Part. No.*		Bestelldatum / *Order Date*	**07.05.2015**
Auftrags-Nr. / Pos. / *Order No. / Item*	**21715386/2**	Artikel-Nr. / *Part No.*	**7745.20**	Ausgangssignal / *Output signal*	**4 ... 20 mA**
Typ / *Model*	**HE150**	Seriennummer / *Serial number*	**10530034894**	Anzeigebereich / *Scale range*	**0 ... 2,5 bar abs.**
Klasse / *Class*	**0,5% FS**	Messstellen-Nr. / *Tag No.*			

Referenzgerät / *Reference*
CPC8000 0,008% FS 0 ... 3,5 bar abs.
Agilent 34401A ME105

Kalibriernummer / *Calibration No.*
01691653
E 1037

Ergebnis / *Result*

Temperatur / *Temperature* **23 °C +/- 1 K**

Referenz Standard bar	Prüfling Test Item bar ↑	Prüfling Test Item bar ↓	Referenz Standard mA	Prüfling Test Item mA ↑	Prüfling Test Item mA ↓	rel. Abweichung rel. Deviation % ↑	rel. Abweichung rel. Deviation % ↓
0,0500	0,047	0,047	4,320	4,30	4,30	-0,12	-0,12
0,3130	0,314	0,314	6,003	6,01	6,01	0,04	0,04
0,6250	0,630	0,630	8,000	8,03	8,03	0,20	0,20
0,9380	0,945	0,945	10,003	10,05	10,05	0,28	0,28
1,2500	1,258	1,258	12,000	12,05	12,05	0,32	0,32
1,5630	1,570	1,570	14,003	14,05	14,05	0,28	0,28
1,8750	1,879	1,880	16,000	16,03	16,03	0,16	0,20
2,1880	2,188	2,188	18,003	18,00	18,00	0,00	0,00
2,5000	2,494	2,494	20,000	19,96	19,96	-0,24	-0,24

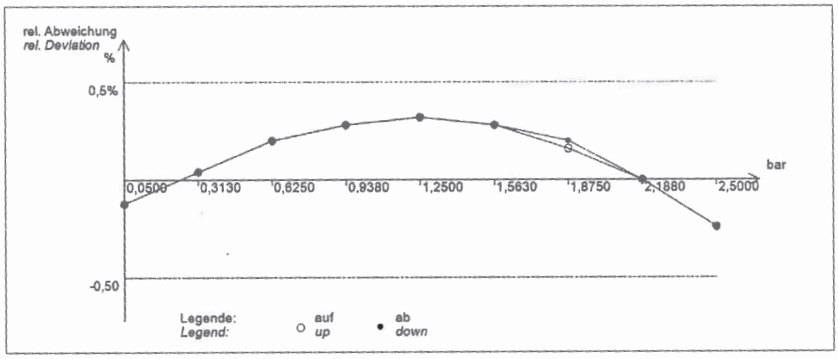

WIKA Alexander Wiegand SE & Co. KG
Alexander-Wiegand-Str. 30
63911 Klingenberg
Germany

Phone: +49 9372 132/0
Fax Inland: +49 9372 132/406
E-Mail: info@wika.de
Internet: www.wika.de

Figure C.5: Calibration data from *Wika* [86] of the pressure transducer PI32 of type *HE 150* by *Hesch*.

C.2 Venturi Tubes

DOSCH MESSAPPARATE GMBH

Berechnungsblatt/Calculation Sheet(EN ISO 5167-4) Version: 2.0.27

Dosch Kommission / Dosch commission	V14-1472			**Datum:**	17.06.2014
Bestellung / order :	723/20573548/ITEP-KRY0				
Projekt/ project :	/				
Tag No:	V14-1472-001	**DN**	50	**PN**	16
Medium :	Helium				
Bauart / construction :	**Venturirohr bearb. Einlauf / Venturi Tube mach. Cone**				
Rohrmaterial / pipe material :	1. 4571				
Wirkdruckgebermaterial / material of flow element	1. 4571				

Betriebsdaten / operating data

Rohrinnendurchmesser / internal pipe diameter(20°C) :	**54,50**	**[mm]**
Aggregatzustand / medium condition:	gasförmig / gaseous	
Massenstrom / massflow rate :	1,00	[kg / s]
Betriebsdichte / operation density	27,6600	[kg/m³]
Temperatur / temperature :	10,0	[Kelvin]
Druck / Pressure (abs.):	5,0000	[bar]
Differenzdruck / differential pressure :	1000,0000	[mbar]
Isentropenexponent / isentropic exponent :	1,630	
Viskosität / viscosity :	2,59E-06	[Pa s]
Rohrrauheit (pipe) / roughness (pipe) :	0,0200	[mm]
Kompressibilität / compressibility (k=Z1/Zn) :	1,0000	
Rohrinnend.(Betriebsbedingung) / int.pipe d.(at op.Temp.) :	54,2543	[mm]
Temp.korrekturfaktor / temp.correction factor (Rohr/pipe):	0,9955	
Temp.korrekturfaktor / temp.correction factor (Blende/Orifice):	0,9955	

Berechnungsdaten / calculation data

(gerechnet mit der vollen Durchflußmenge / calculated with full mass-flow)

Wirkdruckgeberdurchm. / flow element diam. (20 °C):	**24,31**	**[mm]**
Wirkdruckgeberd. / flowelement diam. (Betriebsbedingung):	24,20	[mm]
Durchmesserverhältnis / diameter ratio "ß" (ß=d/D) :	0,4460	
Öffnungsverhältnis / boreratio m = (d/D)² :	0,1989	
Reynoldszahl / reynolds number (100% Durchfluß) :	9,06E+06	
Durchflußzahl / flownumber : Alpha :	1,0306	
Durchflußkoeffizient / coefficient of discharge C :	1,0100	
Vorgeschwindigkeitsfakt. / velocity of approach factor E :	1,0204	
Expansionszahl / expansion factor Epsilon :	0,8972	
Strömungsgeschwindigkeit (Rohr) / Flow velocity (pipe) :	15,64	[m/s]
Strömungsgeschw. / Flow velocity (Blende/Orifice) :	78,63	[m/s]
bleibender Druckverlust / permanent pressure loss :	126,00	[Millibar]
Unsicherheit / uncertainty :	3,83	%
Abschätz. Strömungsgeräusche / estim. noiselevel of flow :	58	[dB(A)]

Erforderliche gerade Rohrstrecken/Requested pipe lengths (Mindestwerte) :

Klammerwerte gelten für 0,5 % Zusatzunsicherheit / ( ) -value +0,5% more uncertainty

Einlaufseite des Drosselgerätes/Upstream side of orifice :

Einfacher 90-Grad Krümmer / single bend 90°	0,44	(0,16)	[m]
Zwei oder mehr 90-Grad Krümmer in rechtwinkligen Ebenen/ Two or more bends in the rectangle levels :	0,44	(0,16)	[m]
Reduzierstück / Reducer	0,30	(0,14)	[m]
Diffusor / Diffusor	0,14	(0,07)	[m]
Schieber / Slide	0,19	(0,14)	[m]

Figure C.6: Data sheet of the smaller Venturi tube by *Dosch Messapparate* [87].

DOSCH MESSAPPARATE GMBH

Berechnungsblatt/Calculation Sheet(EN ISO 5167-4) Version: 2.0.27

Dosch Kommission / Dosch commission	V14-1472			**Datum:**	17.06.2014
Bestellung / order :	723/20573548/ITEP-KRY0				
Projekt/ project :	/				
Tag No:	V14-1472-002	**DN**	50	**PN**	16
Medium :	Helium				
Bauart / construction :	**Venturirohr bearb. Einlauf / Venturi Tube mach. Cone**				
Rohrmaterial / pipe material :	1. 4571				
Wirkdruckgebermaterial / material of flow element	1. 4571				

Betriebsdaten / operating data

Rohrinnendurchmesser / internal pipe diameter(20°C) :	**54,50**	**[mm]**
Aggregatzustand / medium condition:	gasförmig / gaseous	
Massenstrom / massflow rate :	2,00	[kg / s]
Betriebsdichte / operation density	27,6600	[kg/m³]
Temperatur / temperature :	10,0	[Kelvin]
Druck / Pressure (abs.):	5,0000	[bar]
Differenzdruck / differential pressure :	1000,0000	[mbar]
Isentropenexponent / isentropic exponent :	1,630	
Viskosität / viscosity :	2,59E-06	[Pa s]
Rohrrauheit (pipe) / roughness (pipe) :	0,0200	[mm]
Kompressibilität / compressibility (k=Z1/Zn) :	1,0000	
Rohrinnend.(Betriebsbedingung) / int.pipe d.(at op.Temp.) :	54,2543	[mm]
Temp.korrekturfaktor / temp.correction factor (Rohr/pipe):	0,9955	
Temp.korrekturfaktor / temp.correction factor (Blende/Orifice):	0,9955	

Berechnungsdaten / calculation data (gerechnet mit der vollen Durchflußmenge / calculated with full mass-flow)

Wirkdruckgeberdurchm. / flow element diam. (20 °C):	**33,64**	**[mm]**
Wirkdruckgeberd. / flowelement diam. (Betriebsbedingung):	33,48	[mm]
Durchmesserverhältnis / diameter ratio "ß" (ß=d/D) :	0,6172	
Öffnungsverhältnis / boreratio m = (d/D)² :	0,3809	
Reynoldszahl / reynolds number (100% Durchfluß) :	1,81E+07	
Durchflußzahl / flownumber : Alpha :	1,0924	
Durchflußkoeffizient / coefficient of discharge C :	1,0100	
Vorgeschwindigkeitsfakt. / velocity of approach factor E :	1,0815	
Expansionszahl / expansion factor Epsilon :	0,8840	
Strömungsgeschwindigkeit (Rohr) / Flow velocity (pipe) :	31,28	[m/s]
Strömungsgeschw. / Flow velocity (Blende/Orifice) :	82,11	[m/s]
bleibender Druckverlust / permanent pressure loss :	73,50	[Millibar]
Unsicherheit / uncertainty :	4,22	%
Abschätz. Strömungsgeräusche / estim. noiselevel of flow :	60	[dB(A)]

Erforderliche gerade Rohrstrecken/Requested pipe lengths (Mindestwerte) :

Klammerwerte gelten für 0,5 % Zusatzunsicherheit / ( ) -value +0,5% more uncertainty

Einlaufseite des Drosselgerätes/Upstream side of orifice :			
Einfacher 90-Grad Krümmer / single bend 90°	0,76	(0,16)	[m]
Zwei oder mehr 90-Grad Krümmer in rechtwinkligen Ebenen/ Two or more bends in the rectangle levels :	1,04	(0,16)	[m]
Reduzierstück / Reducer	0,57	(0,14)	[m]
Diffusor / Diffusor	0,30	(0,19)	[m]
Schieber / Slide	0,30	(0,19)	[m]

Figure C.7: Data sheet of the larger Venturi tube by *Dosch Messapparate* [87].

C.3 Safety valves

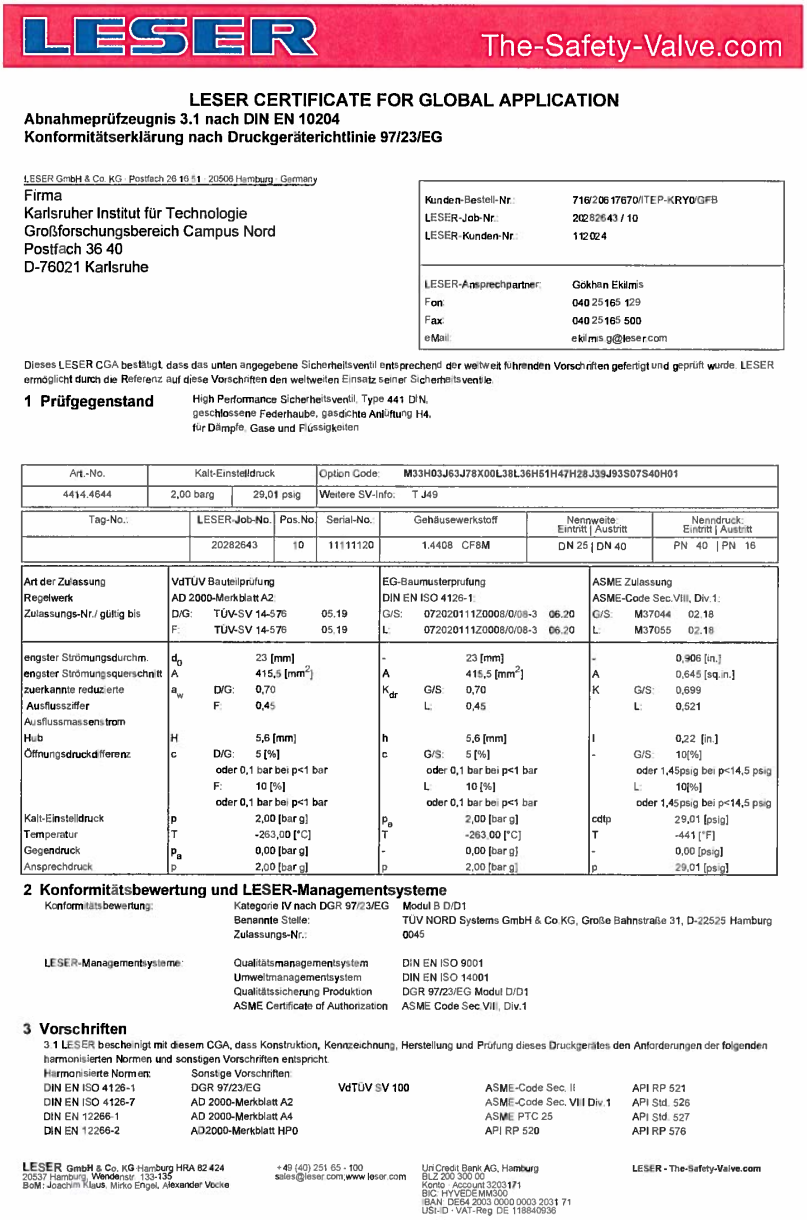

LESER The-Safety-Valve.com

LESER CERTIFICATE FOR GLOBAL APPLICATION
Abnahmeprüfzeugnis 3.1 nach DIN EN 10204
Konformitätserklärung nach Druckgeräterichtlinie 97/23/EG

LESER GmbH & Co. KG · Postfach 26 16 61 · 20506 Hamburg · Germany
Firma
Karlsruher Institut für Technologie
Großforschungsbereich Campus Nord
Postfach 36 40
D-76021 Karlsruhe

Kunden-Bestell-Nr.:	716/20617670/ITEP-KRY0/GFB
LESER-Job-Nr.:	20282643 / 10
LESER-Kunden-Nr.:	112024
LESER-Ansprechpartner:	Gökhan Ekilmis
Fon:	040 25165 129
Fax:	040 25165 500
eMail:	ekilmis.g@leser.com

Dieses LESER CGA bestätigt, dass das unten angegebene Sicherheitsventil entsprechend der weltweit führenden Vorschriften gefertigt und geprüft wurde. LESER ermöglicht durch die Referenz auf diese Vorschriften den weltweiten Einsatz seiner Sicherheitsventile.

1 Prüfgegenstand High Performance Sicherheitsventil, Type 441 DN, geschlossene Federhaube, gasdichte Anlüftung H4, für Dämpfe, Gase und Flüssigkeiten

Art.-No.	Kalt-Einstelldruck		Option Code:	M33H03J63J78X00L38L36H51H47H28J39J93S07S40H01
4414.4644	2,00 barg	29,01 psig	Weitere SV-Info:	T J49

Tag-No.:	LESER-Job-No.	Pos.No.	Serial-No.:	Gehäusewerkstoff	Nennweite: Eintritt | Austritt	Nenndruck: Eintritt | Austritt
	20282643	10	11111120	1.4408 CF8M	DN 25 | DN 40	PN 40 | PN 16

Art der Zulassung	VdTÜV Bauteilprüfung		EG-Baumusterprüfung		ASME Zulassung	
Regelwerk	AD 2000-Merkblatt A2		DIN EN ISO 4126-1:		ASME-Code Sec.VIII, Div.1:	
Zulassungs-Nr./ gültig bis	D/G: TÜV-SV 14-576	05.19	G/S: 07202011Z0008/0/08-3	06.20	G/S: M37044	02.18
	F: TÜV-SV 14-576	05.19	L: 07202011Z0008/0/08-3	06.20	L: M37055	02.18
engster Strömungsdurchm.	d_0	23 [mm]	-	23 [mm]	-	0,906 [in.]
engster Strömungsquerschnitt	A	415,5 [mm²]	A	415,5 [mm²]	A	0,645 [sq.in.]
zuerkannte reduzierte Ausflussziffer	a_w D/G:	0,70	K_{dr} G/S:	0,70	K G/S:	0,699
	F:	0,45	L:	0,45	L:	0,521
Ausflussmassenstrom						
Hub	H	5,6 [mm]	h	5,6 [mm]	l	0,22 [in.]
Öffnungsdruckdifferenz	c D/G:	5 [%]	c G/S:	5 [%]	- G/S:	10[%]
		oder 0,1 bar bei p<1 bar		oder 0,1 bar bei p<1 bar		oder 1,45psig bei p<14,5 psig
	F:	10 [%]	L:	10 [%]	L:	10[%]
		oder 0,1 bar bei p<1 bar		oder 0,1 bar bei p<1 bar		oder 1,45psig bei p<14,5 psig
Kalt-Einstelldruck	p	2,00 [bar g]	p_e	2,00 [bar g]	cdtp	29,01 [psig]
Temperatur	T	-263,00 [°C]	T	-263,00 [°C]	T	-441 [°F]
Gegendruck	p_a	0,00 [bar g]	-	0,00 [bar g]	-	0,00 [psig]
Ansprechdruck	p	2,00 [bar g]	p	2,00 [bar g]	p	29,01 [psig]

2 Konformitätsbewertung und LESER-Managementsysteme

Konformitätsbewertung:	Kategorie IV nach DGR 97/23/EG	Modul B D/D1
	Benannte Stelle:	TÜV NORD Systems GmbH & Co KG, Große Bahnstraße 31, D-22525 Hamburg
	Zulassungs-Nr.:	0045
LESER-Managementsysteme:	Qualitätsmanagementsystem	DIN EN ISO 9001
	Umweltmanagementsystem	DIN EN ISO 14001
	Qualitätssicherung Produktion	DGR 97/23/EG Modul D/D1
	ASME Certificate of Authorization	ASME Code Sec.VIII, Div.1

3 Vorschriften
3.1 LESER bescheinigt mit diesem CGA, dass Konstruktion, Kennzeichnung, Herstellung und Prüfung dieses Druckgerätes den Anforderungen der folgenden harmonisierten Normen und sonstigen Vorschriften entspricht.

Harmonisierte Normen:	Sonstige Vorschriften:			
DIN EN ISO 4126-1	DGR 97/23/EG	VdTÜV SV 100	ASME-Code Sec. II	API RP 521
DIN EN ISO 4126-7	AD 2000-Merkblatt A2		ASME-Code Sec. VIII Div.1	API Std. 526
DIN EN 12266-1	AD 2000-Merkblatt A4		ASME PTC 25	API Std. 527
DIN EN 12266-2	AD2000-Merkblatt HP0		API RP 520	API RP 576

LESER GmbH & Co. KG · Hamburg HRA 82 424
20537 Hamburg, Wendenstr. 133-135
BoM.: Joachim Kaus, Mirko Engel, Alexander Vocke
+49 (40) 251 65 - 100
sales@leser.com; www.leser.com
UniCredit Bank AG, Hamburg
BLZ 200 300 00
Konto - Account 3203171
BIC: HYVEDEMM300
IBAN: DE64 2003 0000 0003 2031 71
USt-ID - VAT-Reg: DE 118840936
LESER - The-Safety-Valve.com

Figure C.8: First data sheet of the new safety relief valve of type 441 by *Leser* [67].

LESER The-Safety-Valve.com

Job 20282643 / 10 / Ser.No. 11111120 /Seite 2

3.2 Prüfungen	Richtlinie	DIN EN ISO	DIN EN 12266		ASME CODE	API			AD2000 Merkblatt				LESER Standard
	97/23/EG Anhang 1	4126-1	Teil 1	Teil 2	Sec.VIII Div.1	526	527	576	A2	A4	HPO		LGS
Prüfung Einstelldruck	3.2.3	6.5			UG 136(d)(4)	4.2	2/3/4	6.2.14	11.1 11.4				LGS 0202
Prüfung Sitzdichtheit		6.6	4.4 (P12)		UG 136(d)(5)	4.3	2/3/4	6.2.17					LGS 0201
Prüfung Dichtheit nach Außen				4. (P21)	UG 136(d)(3)								LGS 0201
Funktionsprüfung		7		4. (F20)					11.3				LGS 0201
Prüfung Gehäusedichtheit			4.4 (P11)										LGS 0201
Hydrostatische Druckprüfung	3.2.2 7.4	6.3.1 6.3.2	4.4 (P10)		UG 136(d)(2)					6.1.(4)			LGS 0209
Zerstörungsfreie Prüfung					UG 136(f)					6.1.(5)			LGS 0203 bis LGS 0206
Prüfung auf Werkstoffverwechslung										6.1.(6)			LGS 0207
Kennzeichnung					UG 77				8	7.1	4		LGS 0218
Prüfung auf Maßhaltigkeit										6.1.(3)			LGS 0216

4 Werkstoffeignung und Kennzeichnung

4.1. LESER bescheinigt, dass die Eignung der verwendeten Werkstoffe den unter Punkt 3.1 zitierten Vorschriften entspricht.

4.2. Die Kennzeichnung der Werkstoffe sowie deren Übertragung erfolgte wie folgt:

Stckl-Pos	Benennung	Werkstoff	Hersteller	Schmelze	LESER-Code
1	Gehäuse	1.4408 CF8M	Peekay Steel Castings Pvt. Ltd	S6816	

5 Prüfungen

Die im Folgenden aufgeführten Prüfungen wurden auf Grundlage der angeführten LESER Standards ohne Beanstandungen durchgeführt:

5.1. Ventil-Gehäuse-Prüfung

Dichtheitsprüfung der Gehäuse
Hydrostatische Druckprüfung
Zerstörungsfreie Prüfung
Prüfung auf Werkstoffverwechslung bei Gehäuseteilen aus legierten Werkstoffen
Die Durchführung der Prüfungen erfolgte durch: LESER GmbH & Co. KG

5.2. Sicherheitsventil Einstellung und Prüfung

Sitzdichtheit
Dichtheit nach Aussen
Funktionsprüfung
Kalt-Einstelldruck

Die Einstellung auf 2,00 [X] barg [ ] psig
erfolgte mit [X] Luft [ ] Wasser [ ] Sattdampf
bei [X] Umgebungstemperatur [ ] Sattdampftemperatur [ ] _____ [ ] °C [ ] °F

Das Sicherheitsventil wurde gesichert mit einer Plombe, die gekennzeichnet ist mit:

Die Durchführung der Prüfung erfolgte durch: LESER GmbH & Co. KG

LESER GmbH & Co. KG Hamburg HRA 62 424
20537 Hamburg, Wendenstr. 133-135
BoM: Joachim Kraus, Mirko Engel, Alexander Vocke

+49 (40) 251 65 - 100
sales@leser.com;www.leser.com

UniCredit Bank AG, Hamburg
BLZ 200 300 00
Konto - Account 3203171
BIC: HYVEDEMM300
IBAN: DE84 2003 0000 0003 2031 71
USt-ID - VAT-Reg DE 118840936

LESER - The-Safety-Valve.com

Figure C.9: Second data sheet of the new safety relief valve of type 441 by *Leser* [67].

Approved Body of the TÜV NORD Systems GmbH & Co.KG
Postfach 45 02 20 - 22502 Hamburg

TÜV NORD

LESER GmbH & Co.KG
Postfach 26 16 51 D-20506 Hamburg
Wendenstr. 133-135 D-20537 Hamburg

Firma
Karlsruher Institut für Technologie
Großforschungsbereich Campus Nord
Postfach 36 40
76021 Karlsruhe

Customers Order No.	716/20617670/ITEP-KRY0/GFB
LESER-Job-No.	20282643 / 10
LESER-Customers-No.	112024
LESER-Contact:	Gökhan Ekilmis
Fon:	040 25165 129
Fax:	040 25165 500
eMail:	ekilmis.g@leser.com

Attention! Translation of original and signed document.
Inspection certificate 3.2 according to DIN EN 10204 for setting of safety valves
in accordance to AD 2000-Merkblatt A2 chapter 11.4, AD 2000-Merkblatt HP 512R chapter 5, HP 512 chapter 7 and PED 97/23/EG, annex I chapter 3.2.3

Test object

High Performance Safety Relief Valve, Type 441 DIN,
closed bonnet, gastight lifting device H4,
for steam, gas and liquid service

Art.-No.	Cold differential test pressure		Option Code:	M33H03J63J78X00L38L36H51H47H28J39J93S07S40H01
4414.4644	2,00 barg	29,0 psig	Further SV-Info:	T J49

Tag-No.	LESER-Job-No.	Pos.-No	Serial-No.	Body material	Nominal size: Inlet | Outlet	Pressure rating: Inlet | Outlet
	20282643	10	11111120	1.4408 CF8M	DN 25 | DN 40	PN 40 | PN 16

Kind of certification / Rules / Certification No. / valid until	VdTUEV Type Test Approval AD 2000-Merkblatt A2	EG-Type Examination DIN EN ISO 4126-1:	ASME Certification ASME-Code Sec.VIII, Div.1:
	D/G: TÜV-SV 14-576 05.19	G/S: 072020111Z0008/0/08-3 06.20	G/S: M37044 02.18
	F: TÜV-SV 14-576 05.19	L: 072020111Z0008/0/08-3 06.20	L: M37055 02.18
Flow diameter	d_0 23 [mm]	- 23 [mm]	- 0,906 [in.]
Flow area	A 415,5 [mm²]	A 415,5 [mm²]	A 0,645 [sq.in.]
Certified derated coefficient of discharge	a_w D/G: 0,70	K_{dr} G/S: 0,70	K G/S: 0,699
	F: 0,45	L: 0,45	L: 0,521
Certified capacity			
Lift	H 5,6 [mm]	h 5,6 [mm]	l 0,22 [in.]
Overpressure	c D/G: 5 [%]	c G/S: 5 [%]	- G/S: 10[%]
	F: 10 [%]	L: 10 [%]	L: 10[%]
Cold differential test pressure	p 2,00 [bar g]	p_e 2,00 [bar g]	cdtp 29,0 [psig]
Temperature	T -263,00 [°C]	T -263,00 [°C]	T -441 [°F]
Backpressure	p_a 0,00 [bar g]	- 0,00 [bar g]	- 0,00 [psig]
Set pressure	p 2,00 [bar g]	p 2,00 [bar g]	p 29,0 [psig]

Setting

Setting at 2,00 [X] barg [ ] psig
with [X] air [ ] water [ ] saturated steam
at [X] ambient temperature [ ] saturated steam temperature [ ] _____ [ ] °C [ ] °F
according to LGS 0202.

The safety valve is locked by a seal, marked with:

Attention! Translation of original and signed document.

Marinela Laschinski
Inspection Representative

Representative of the AB of the TÜVNORD

Figure C.10: Setting protocol of the new safety relief valve of type 441 by *Leser* [67].

LESER The Safety Valve

LESER CERTIFICATE FOR GLOBAL APPLICATION

Abnahmeprüfzeugnis 3.1 nach DIN EN 10204
Konformitätserklärung nach Druckgeräterichtlinie 97/23/EG

LESER GmbH & Co. KG · Postfach 26 16 51 · 20506 Hamburg, Germany
Firma
Forschungszentrum Karlsruhe GmbH
In der Helmholtz-Gemeinschaft
Postfach 36 40
76021 Karlsruhe

Kunden-Bestell-Nr.:	716/20346817/ITP
LESER-Job-Nr.:	20031165 / 10
LESER-Kunden-Nr.:	112024
LESER-Ansprechpartner:	Dirk Turowski
Fon:	040 25 165 129
Fax:	040 25 165 500
eMail:	turowski.d@leser.com

Dieses LESER CGA bestätigt, dass das unten angegebene LESER Sicherheitsventil entsprechend der weltweit führenden Vorschriften gefertigt und geprüft wurde. LESER ermöglicht durch die Referenz auf diese Vorschriften den weltweiten Einsatz seiner Sicherheitsventile.

1 Prüfgegenstand

High Performance Sicherheitsventil, Type 441 DIN,
geschlossene Federhaube, gasdichte Anlüftung H4,
für Dämpfe, Gase und Flüssigkeiten

Art.-No.	Kalt-Einstelldruck		Option Code:	**M33H03J63J78L38L36H51H47H28J39 J93S07S40H01**
4414.4644	2,00 barg	29,01 psig	Weitere SV-Info:	

Tag-No.:	LESER-Job-No.	Pos.No.	Serial-No.:	Gehäusewerkstoff	Nennweite: Eintritt | Austritt	Nenndruck: Eintritt | Austritt
	20031165	10	10135819	1.4408 / CF8M	DN 25 | DN 40	PN 40 D | PN 16 D

Art der Zulassung	VdTÜV Bauteilprüfung				EG-Baumusterprüfung				ASME Zulassung			
Regelwerk	AD 2000-Merkblatt A2:				DIN EN ISO 4126-1:				ASME-Code Sec.VIII, Div.1:			
Zulassungs-Nr./ gültig bis	D/G:	TÜV-SV 04-576	31.05.09		G/S:	072020111Z0008/0/08-2	01.07.10		G/S:	M37044	17.02.07	
	F:	TÜV-SV 04-576	31.05.09		L:	072020111Z0008/0/08-2	01.07.10		L:	M37055	30.01.07	
engster Strömungsdurchm.	d_0		23 [mm]		-		23 [mm]		-		0,906 [in.]	
engster Strömungsquerschnitt	A		415,5 [mm^2]		A		415,5 [mm^2]		A		0,645 [sq.in.]	
zuerkannte reduzierte	a_w	D/G:	0,70		K_{dr}	G/S:	0,70		K	G/S:	0,699	
Ausflussziffer		F:	0,45			L:	0,45			L:	0,521	
Ausflussmassenstrom												
Hub	H		5,6 [mm]		h		5,6 [mm]		l		0,22 [in.]	
Öffnungsdruckdifferenz	c	D/G:	5 [%]		c	G/S:	5 [%]		-	G/S:	10[%]	
		F:	10 [%]			L:	10 [%]			L:	10[%]	
Kalt-Einstelldruck	p		2,00 [bar g]		p_e		2,00 [bar g]		cdtp		29,0 [psig]	
Temperatur-Korrektur	-		-263,00 [°C]		T_0		10,2 [K]		T		-441 [°F]	
Gegendruck-Korrektur	-		0,00 [bar g]		p_b		0,00 [bar g]		p_0		0,00 [psig]	
Ansprechdruck	-		2,00 [bar g]		p		2,00 [bar g]		p		29,0 [psig]	

2 Konformitätsbewertung und LESER-Managementsysteme

Konformitätsbewertung:	Kategorie IV nach DGR 97/23/EG	Modul B D/D1	
	Benannte Stelle:	TÜV NORD Systems GmbH & Co.KG, Große Bahnstraße 31, D-22525 Hamburg	
	Zulassungs-Nr.:	0045	
LESER-Managementsysteme:	Qualitätsmanagementsystem	DIN EN ISO 9001:2000	Zulassungs-Nr. 07 100 0068
	Umweltmanagementsystem	DIN EN ISO 14001:2005	Zulassungs-Nr. 07 104 0068
	Qualitätssicherung Produktion	DGR 97/23/EG Modul D/D1	Zulassungs-Nr. 07 2020111 Z 0008/0/01-2
	ASME Certificate of Authorization	ASME Code Sec.VIII, Div.1	27,806

3 Vorschriften

LESER bescheinigt mit diesem CGA, dass Konstruktion, Kennzeichnung, Herstellung und Prüfung dieses Druckgerätes den Anforderungen der folgenden Vorschriften (Richtlinien, Regelwerke, Normen und Standards) entspricht.

Harmonisierte Normen:		Sonstige Vorschriften:		
DIN EN ISO 4126-1	DGR 97/23/EG	VdTÜV SV 100	ASME-Code Sec. II	API RP 521
DIN EN ISO 4126-7	AD 2000-Merkblatt A2	TRD 110	ASME-Code Sec. VIII Div.1	API Std. 526
DIN EN 12266-1	AD 2000-Merkblatt A4	TRD 421	ASME PTC 25	API Std. 527
DIN EN 12266-2	AD2000-Merkblatt HP0	TRD 721	API RP 520	API RP 576

LESER GmbH & Co. KG Hamburg HRA 82 424
GF · BoD Joachim Klaus, Martin Leser
20537 Hamburg, Wendenstr. 133-135
20506 Hamburg, P.O. Box 26 16 51

Fon +49 (40) 251 65 - 100
Fax +49 (40) 251 65 - 500
E-Mail sales@leser.com
Internet www.leser.com

Bank HypoVereinsbank, Hamburg
BLZ 200 300 00, Konto · Account 3203171
BIC: HYVEDEMM300
IBAN: DE64 2003 0000 0003 2031 71
USt-ID · VAT DE 118840936

LESER - The Safety Valve

Figure C.11: First data sheet of the older safety relief valve of type 441 by *Leser* [67].

LESER The Safety Valve

Job 20031165 / 10 / Ser.No. 10135819 /Seite 2

	Richtlinie	DIN EN ISO	DIN EN 12266		ASME CODE	API				AD2000 Merkblatt			TRD	LESER Standard
	97/23/EG Anhang 1	4126-1	Teil 1	Teil 2	Sec.VIII Div.1	520	526	527	576	A2	A4	HPO	TRD 110	LWN
Prüfung Einstelldruck	3.2.3	6.5			UG 136(d)(4)		4.2	2/3/4	6.2.14	11.1 11.4				220.04
Prüfung Sitzdichtheit		6.6	4.4 (P12)		UG 136(d)(5)		4.3	2/3/4	6.2.17					220.01
Prüfung Dichtheit nach Außen				4. (P21)	UG 136(d)(3)									220.07
Prüfung Funktionssicherheit	3.2.3			4. (F20)	UG 136(d)(5)	10.2			6.2.9	11.3				618.23
Konstruktionsprüfung											6.1.(1)		4.2.1(1)	300.00
Besichtigung auf Fehler	3.2.1										6.1.(2)		4.2.1(2)	618.23
Prüfung Maßhaltigkeit											6.1.(3)		4.2.1(3)	618.23
Prüfung Gehäusedichtheit			4.4 (P11)										4.2.1(4)	220.07
Hydrostatische Druckprüfung	3.2.2 7.4	6.3.1 6.3.2	4.4 (P10)		UG 136(d)(2)						6.1.(4)		4.2.1(5)	275.18
Zerstörungsfreie Prüfung					UG 136(f)						6.1.(5)		4.2.1(6)	275.30
Prüfung auf Werkstoffverwechslung											6.1.(6)		4.2.1(7)	275.40
Kennzeichnung					UG 77					8	7.1	4	5.	201.04

4 Werkstoffeignung und Kennzeichnung

4,1. LESER bescheinigt, dass die Eignung der verwendeten Werkstoffe den unter Punkt 3 zitierten Vorschriften entspricht.

4.2. Die Kennzeichnung der Werkstoffe sowie deren Übertragung erfolgte wie folgt:

Stckl-Pos	Benennung	Werkstoff	Hersteller	Schmelze	LESER-Code
1	ECKGEH DN 25 +SITZ H47H51L36L38	1.4408 A351 CF8M	ETC	L8287	

5 Prüfungen

Die im Folgenden aufgeführten Prüfungen wurden auf Grundlage der LESER Werknorm (LWN) ohne Beanstandungen durchgeführt:

5.1. Ventil-Gehäuse-Prüfung

Spannungstechnische Beurteilung und sicherheitstechnische Konstruktionsprüfung:	LWN 300.00
Besichtigung des fertigen Gehäuses auf Fehler:	LWN 618.23
Überprüfung der fertigen Gehäuse auf Maßhaltigkeit	LWN 618.23
Dichtheitsprüfung der Gehäuse:	LWN 220.07
Hydrostatische Druckprüfung:	LWN 275.18
Zerstörungsfreie Prüfung:	LWN 275.30
Prüfung auf Werkstoffverwechslung bei Gehäuseteilen aus legierten Werkstoffen:	LWN 275.40
Die Durchführung der Prüfungen erfolgte durch:	LESER GmbH & Co.KG

5.2. Sicherheitsventil Einstellung und Prüfung

Sitzdichtheit	LWN 220.01
Dichheit nach Aussen	LWN 220.07
Funktionssicherheit	LWN 618.23
Einstelldruck	LWN 220.04

Die Einstellung auf 2,00 [X] barg [_] psig

erfolgte mit [X] Luft [_] Wasser [_] Sattdampf

bei [X] Umgebungstemperatur [_] Sattdampftemperatur [_] _____ [_]

°C [_] °F

Das Sicherheitsventil wurde gesichert mit einer Plombe, die gekennzeichnet ist mit:

Die Durchführung der Prüfung erfolgte durch: LESER GmbH & Co. KG

6 CERTIFICATE OF SHOP COMPLIANCE

By the signature of the Certified Individual (CI) noted below, we certify that the statements made in this report are correct and that all details for design, material,

construction, and workmanship of the pressure relief devices are conform with the requirements of Section VIII, Division 1 of the ASME Boiler and Pressure

UV Certificate of Authorization No. 27,806
Expires June 16.2009

Martin Leser
LESER GmbH & Co. KG

Datum: 10.11.2006

Manfred Orlowski
Der Abnahmebeauftragte Werk Hohenwestedt
Certified Individual (CI)

LESER GmbH & Co. KG Hamburg HRA 82 424
GF · BoD Joachim Klaus, Martin Leser
20537 Hamburg, Wendenstr. 133-135
20506 Hamburg, P.O. Box 26 16 51

Fon +49 (40) 251 65 - 100
Fax +49 (40) 251 65 - 500
E-Mail sales@leser.com
Internet www.leser.com

Bank HypoVereinsbank, Hamburg
BLZ 200 300 00, Konto · Account 3203171
BIC: HYVEDEMM300
IBAN: DE64 2003 0000 0003 2031 71
USt-ID · VAT DE 118840936

LESER - The Safety Valve

Figure C.12: Second data sheet of the older safety relief valve of type 441 by *Leser* [67].

C.4 Vacuum pump

HiCube 80 Classic, DN 63 ISO-K, MVP 040, 230 V AC

- Combined pumping station including turbopump and backing pump for all high vacuum applications
- Air-cooled and ready for operation with HiPace 80 and dry diaphragm backing pump MVP 040
- Standard version with rubber feet (without cable set for external use)

Dimensions

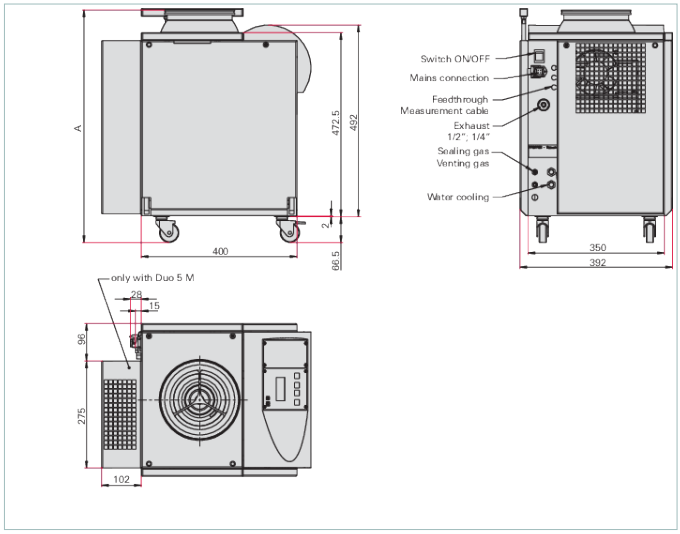

A 581 mm

Technical Data	HiCube 80 Classic, DN 63 ISO-K, MVP 040, 230 V AC
Backing pump	MVP 040
Cooling method, standard	Air
Flange (in)	DN 63 ISO-K
Flange (out)	G 1/2"; G 1/4"
Fore-vacuum safety valve	-
Mains requirement	230 V AC, 50/60 Hz
Pumping speed backing pump at 50 Hz	2.3 m³/h
Pumping speed for N_2	67 l/s
Turbopump	HiPace 80
Type	Turbo pumping station
Ultimate pressure	$< 1 \cdot 10^{-7}$ hPa | $< 7.5 \cdot 10^{-8}$ Torr | $< 1 \cdot 10^{-7}$ mbar
Weight	40.2 kg | 88.62 lb

Figure C.13: Extract from the data sheet of the vacuum pumping station of High Cube 80, with kind support of the *Pfeiffer Vacuum GmbH* [88].

Bibliography

[1] N. Kurti, *Cryogenics* **10**, 183 – 185 (1970), ISSN 0011-2275.

[2] Cryodata Inc., *GASPAK*, Horizon Technologies, 3.35$^{\text{th}}$ edn. (1999).

[3] S. W. Van Sciver, *Helium cryogenics*, International cryogenics monograph series, Springer, New York, 2012, 2$^{\text{nd}}$ edn., ISBN 978-1-441-99978-8; 1-441-99978-7.

[4] R. Radebaugh, *The MacMillan Encyclopedia Of Chemistry* (2002), URL `http://www.cryogenics.nist.gov/AboutCryogenics/about%20cryogenics.htm`, accessed: 2016-04-14.

[5] G. G. Haselden, editor, *Cryogenic fundamentals*, Acad. Pr., London, 1971, ISBN 0-12-330550-0.

[6] M. Stemmle, F. Merschel, M. Noe, and A. Hobl, 22$^{\text{nd}}$ *Int. Conf. Electricity Distribution* (2013).

[7] E. Shabagin, C. Heidt, S. Strauß, and S. Grohmann, *Cryogenics* **81**, 24 – 32 (2017), ISSN 0011-2275.

[8] C. O'Luanaigh, The Large Hadron Collider (2014), URL `http://cds.cern.ch/record/1998498`, accessed: 2016-04-14.

[9] B. Seeber, editor, *Handbook of applied superconductivity*, vol. 2: Applications, Institute of Physics Publ., Philadelphia, 1998, ISBN 0-7503-0377-8.

[10] M. N. Wilson, *Superconducting magnets*, Clarendon Press, Oxford, 2002, reprint. edn., ISBN 0-19-854810-9.

[11] Y. Iwasa, *Case studies in superconducting magnets - Design and operational issues*, Springer, 2009, 2$^{\text{nd}}$ edn., ISBN 978-0-387-09799-2.

[12] H. Frey, and R. A. Haefer, *Tieftemperaturtechnologie*, VDI-Verl., Düsseldorf, 1981, ISBN 3-18-400503-8.

[13] E. W. Lemmon, M. L. Huber, and M. O. McLinden, *NIST Standard Reference Database 23: Reference Fluid Thermodynamic and Transport Properties - REFPROP*, 9$^{\text{th}}$ edn. (2010).

[14] DIN SPEC 4683, Cryostats for liquefied helium - Safety devices for protection against excessive pressure (2015).

[15] 2014/68/EU, Directive 2014/68/EU of the European parliament and of the council of 15 May 2014 on the approximation of the laws of the member states concerning pressure equipment (2014).

[16] C. Heidt, S. Grohmann, and M. Süßer, *AIP Conf. Proc.* **1573**, 1574–1580 (2014).

[17] ISO 4126-1, Safety devices for protection against excessive pressure - Part 1: Safety valves (2004).

[18] AD 2000-Merkblatt A 1, Sicherheitseinrichtungen gegen Drucküberschreitung - Berstsicherungen (2006).

[19] AD 2000-Merkblatt A 2, Sicherheitseinrichtungen gegen Drucküberschreitung - Sicherheitsventile (2012).

[20] A. P. Varghese, and B. X. Zhang, *Adv. Cryog. Eng.* **37**, 1487–1493 (1991).

[21] ISO 21013-3, Pressure-relief accessories for cryogenic service - Part 3: Sizing and capacity determination; German version EN ISO 21013-3:2016 (2016).

[22] API 520-1, Sizing, selection, and installation of pressure-relieving devices in refineries - Part 1: Sizing and selection (2000).

[23] W. Lehmann, and G. Zahn, *Proc. Int. Cryog. Eng. Conf.* **7**, 569–579 (1978).

[24] G. Cavallari, I. Gorin, D. Güsewell, and R. Stierlin, *Proc.* 4^{th} *Workshop on RF Supercon.* **1**, 781–803 (1989).

[25] S. M. Harrison, *IEEE T. Appl. Supercon.* **12**, 1343–1346 (2002), ISSN 1051-8223.

[26] C. Heidt, H. Schön, M. Stamm, and S. Grohmann, *IOP Conf. Ser.: Mater. Sci. Eng.* **101**, 012161 (2015).

[27] C. Heidt, A. Henriques, M. Stamm, and S. Grohmann, *IOP Conf. Ser.: Mater. Sci. Eng.* **171**, 012044 (2017).

[28] W. Obert, J. R. Coupland, T. Hammond, D. P.and Cook, and K. Harwood, *Adv. Cryog. Eng.* **27**, 293 (1982).

[29] S. Grohmann, and M. Süßer, *AIP Conf. Proc.* **1573**, 1581–1585 (2014).

[30] P. Lee, "Superconducting Wires and Cables: Materials and Processing," in *Encyclopedia of Materials: Science and Technology (Second Edition)*, edited by K. H. Veyssiere, J. Buschow, R. W. Cahn, M. C. Flemings, Flemings, B. Ilschner, E. J. Kramer, and S. Mahajan, Elsevier, Oxford, 2003, pp. 1 – 11, 2nd edn., ISBN 978-0-08-043152-9.

[31] ISO 4126-10, Safety devices for protection against excessive pressure - Part 10: Sizing of safety valves for gas/liquid two-phase flow (2010).

[32] A. V. Belonogov, O. K. Tabunshchikova, and V. L. Morgunov, *Chemical and Petroleum Engineering* **14**, 243–245 (1978), ISSN 1573-8329.

[33] G. F. Xie, X. D. Li, and R. S. Wang, *Heat and Mass Transfer* **46**, 457–462 (2010).

[34] G. Xie, X. Li, and R. Wang, *Cryogenics* **50**, 682 – 687 (2010), ISSN 0011-2275.

[35] M. Zhu, and R. Wang, *Cryogenics* **52**, 331 – 335 (2012), ISSN 0011-2275.

[36] V. D. Bartenev, V. I. Dadskov, Y. A. Shishov, and A. G. Zel'dovich, *Cryogenics* **26**, 293–296 (1986).

[37] E. Ercolani, A. Gauthier, P. Gully, and J. Poncet, Quantification of heat flux in supercritical helium, Presentation at the 1st Cryogenic Safety - HSE Seminar at CERN (2016), URL `https://indico.cern.ch/event/495194/contributions/2181322/`.

[38] R. C. Dhuley, and S. W. V. Sciver, *IOP Conf. Ser.: Mater. Sci. Eng.* **101**, 012006 (2015).

[39] R. C. Dhuley, and S. W. V. Sciver, *IEEE T. Appl. Supercon.* **25**, 1–5 (2015), ISSN 1051-8223.

[40] E. S. Bosque, R. C. Dhuley, and S. W. Van Sciver, *AIP Conf. Proc.* **1573**, 260–267 (2014).

[41] M. Chorowski, J. Fydrych, J. Polinski, and M. Süßer, *Proc. Int. Cryog. Eng. Conf.* **21**, 141–144 (2006).

[42] M. Chorowski, J. Fydrych, and J. Polinski, Study for DPS2. Calculation of the quench gas line diameter and of the safety valve flow coefficient kv for the worst case: simultaneous quench of all magnets together with a sudden breakdown of the vacuum., internal report 325/20293676/IIP, Forschungszentrum Karlsruhe (2005).

[43] C. Heidt, *Untersuchungen zur Sicherheit von Flüssighelium-Druckbehältern*, Diplomarbeit, Karlsruhe Institute of Technology (KIT), Karlsruhe, Germany (2012).

[44] C. Heidt, S. Grohmann, and M. Süßer, Modellierung des Druckanstiegs in einem Flüssighelium-Behälter bei Zusammenbruch des Isoliervakuums, Tagungs-CD zur Deutschen Kälte- und Klimatagung (2012).

[45] T. A. Neumann, M. R. Albert, C. Engel, Z. Courville, and F. Perron, *Int. J. Heat Mass Tran.* **52**, 309–315 (2009).

[46] Wolfram Research, *Mathematica (Version 10.3.1.0.)* (2010).

[47] AD 2000-Merkblatt W 10, Werkstoffe für tiefe Temperaturen - Eisenwerkstoffe (2007).

[48] C. Heidt, S. Grohmann, H. Schön, and M. Stamm, Aufbau eines Versuchsstands zur Messung der Vorgänge in einem Flüssigheliumbehälter bei Zusammenbruch des Isoliervakuums, Tagungs-CD zur Deutschen Kälte- und Klimatagung (2013).

[49] V. I. Dadskov, and J. G. Weisend II, *Proc Int. Cryog. Eng. Conf.* **15**, 425–428 (1994).

[50] M. Süßer, *Proc Int. Cryog. Eng. Conf.* **17**, 699–702 (1998).

[51] Y. A. Dedikov, and Y. P. Filippov, *Proc Int. Cryog. Eng. Conf.* **18**, 627–630 (2000).

[52] K. Gieck, and R. Gieck, *Technische Formelsammlung*, Gieck, Germering, 2005, 31st German edn., 78th tot. circ. edn., ISBN 3-920379-25-X; 978-3-446-42031-1.

[53] M. Heiduk, N. Bagrets, and K. P. Weiss, *IEEE T. Appl. Supercon.* **22**, 9000604 (2012).

[54] Collaborative R&D on experimental testing on cryogenic pressure relief between CERN and KIT, KE2974/KT/DGS/222C (2015).

[55] Niehus, *LESER global standard - Assembly instruction for series 441,441 Full nozzle, 458, 429, 433, types 440,424, 546*, 1st edn. (2011).

[56] API 527, Seat tightness of pressure relief valves (2002).

[57] ISO 5167-2, Measurement of fluid flow by means of pressure differential devices inserted in circular cross-section conduits running full - Part 2: Orifice plates (2004).

[58] J. F. Kenney, and E. S. Keeping, *Mathematics of Statistics*, Part 1, Princeton, NJ: Van Nostrand, 1962, 3rd edn.

[59] F. Puente León, and H. Jäkel, *Signale und Systeme*, De Gruyter Oldenbourg, 2015, 6th edn.

[60] S. Deng, D. Cassidy, R. Greaves, and A. M. Jr., *Appl. Surf. Sci.* **253**, 9467 – 9469 (2007), ISSN 0169-4332.

[61] R. Span, E. Lemmon, R. Jacobsen, W. Wagner, and A. Yokozeki, *J. Phys. Chem. Ref. Data* **29(6)**, 1361–1433 (2000).

[62] ISO 5167-4, Measurement of fluid flow by means of pressure differential devices inserted in circular cross-section conduits running full - Part 4: Venturi tubes (2004).

[63] Working Group 1 of the Joint Committee for Guides in Metrology, *Evaluation of measurement data - Guide to the expression of uncertainty in measurement*, JCGM 100:2008, International Organization for Standardization, Genève, 2008, 1st edn.

[64] M. Süßer, Messunsicherheit und Temperaturauflösung in der kryogenen Temperaturmessung, Tagungs-CD zur Deutschen Kälte- und Klimatagung (2013).

[65] D. Ortiz-Vega, K. Hall, V. Arp, and E. Lemmon, *J. Phys. Chem. Ref. Data* **to be published** (2013).

[66] ISO 4126-9, Safety devices for protection against excessive pressure - Part 9: Application and installation of safety devices excluding stand-alone bursting disc safety devices (2008).

[67] LESER GmbH & Co. KG, *High Performance Catalog 1*, May 2012/2.000 edn. (2012).

[68] G. Dahlquist, and Å. Björk, *Numerical Methods*, Dover Books on Mathematics, Dover Publications, 2003, ISBN 9780486428079.

[69] V. Benda, Block 4 and cluster D - safety, Presentation at the 1st Cryogenic Safety - HSE Seminar at CERN (2016), URL `https://indico.cern.ch/event/495194/contributions/2149421/`.

[70] V. A. Konstantinov, V. G. Manzhelii, V. P. Revyakin, and V. V. Sagan, *Low Temperature Physics* **31**, 419–422 (2005).

[71] T. Scott, *Physics Reports* **27**, 89 – 157 (1976), ISSN 0370-1573.

[72] Spranz, Gunter, *Cryogenic Data Mathematica Package*, Ing.-Büro Elmar Röther, 1.0st edn. (2011).

[73] D. Friend, V. Arp, and McCarty, *HEPAK (©copyright Cryodata, Inc.*, 3.4th edn. (1998).

[74] R. A. Haefer, *Cryopumping : Theory and Practice*, Monographs on cryogenics ; 4, Clarendon Pr., Oxford, 1989, 1st publ. in Engl. edn., ISBN 0-19-854812-5.

[75] M. Bond, and H. Struchtrup, *Phys. Rev. E* **70**, 061605 (2004).

[76] R. Brown, and J. H. Jr., *Adv. Cryogen. Eng.* **13**, 243 – 251 (1968).

[77] R. Marek, and J. Straub, *Int. J. Heat Mass Tran.* **44**, 39 – 53 (2001), ISSN 0017-9310.

[78] H. Sigloch, editor, *Technische Fluidmechanik*, Springer, 2009, 7$^{\text{th}}$ edn.

[79] D. Rist, *Dynamik realer Gase: Grundlagen, Berechnungen und Daten für Thermogasdynamik, Strömungsmechanik und Gastechnik*, Springer, Berlin, 1996, ISBN 978-3-642-64822-9; 3-540-58638-5.

[80] R. C. Dhuley, E. S. Bosque, and S. W. Van Sciver, *Adv. Cryog. Eng.* **1573**, 626–632 (2014).

[81] R. Dhuley, and S. V. Sciver, *Int. J. Heat Mass Tran.* **96**, 573 – 581 (2016), ISSN 0017-9310.

[82] R. Dhuley, and S. V. Sciver, *Int. J. Heat Mass Tran.* **98**, 728 – 737 (2016), ISSN 0017-9310.

[83] W. Steward, *Int. J. Heat Mass Tran.* **21**, 863 – 874 (1978), ISSN 0017-9310.

[84] Pfeiffer Vacuum GmbH, *PCR 280,* 80°C*, DN 16 ISO-KF*, URL `https://www.pfeiffer-vacuum.com/productPdfs/PTR26855.en.pd`, accessed: 2017-06-20.

[85] Pfeiffer Vacuum GmbH, *PKR 251, FPM sealed, DN25 ISO-KF*, URL `https://www.pfeiffer-vacuum.com/productPdfs/PTR26000.en.pdf`, accessed: 2017-11-30.

[86] WIKA Alexander Wiegand SE & Co. KG, *Calibration & service centre*, URL `http://en-co.wika.de/service_calibration_service_pressure_en_co.WIKA`, accessed: 2017-11-30.

[87] Dosch Messapparate GmbH, *Venturi Tubes*, URL `http://www.dosch-gmbh.de/en/flow/dp-flow-elements/venturi-tubes/`, accessed: 2017-11-30.

[88] Pfeiffer Vacuum GmbH, *HiCube 80 Classic, DN 63 ISO-K, MVP 040, 230 V AC*, URL `https://www.pfeiffer-vacuum.com/productPdfs/PMS2123000.de.pdf`, accessed: 2017-11-30.

List of abbreviations and symbols

Latin symbols

Symbol	Quantity	Unit
a	Liquid level	cm
$\bar{A}$	Average area	m^2
A	Surface area	m^2
A_0	Smallest cross-section of safety relief valve	m^2
a_h	Half-width of an interval (GUM)	
A_{Vent}	Cross-section for venting	m^2
B	Magnetic field	T
b_{neg}	Maximum negative relative deviation	-
b_{pos}	Maximum positive relative deviation	-
c	Specific heat capacity	$kJ/(kg \cdot K)$
C	Capacitance	F
C_A	Orifice calibration coefficient	-
C_B	Orifice calibration coefficient	$Pa^{-0.5}$
C_C	Orifice calibration coefficient	$Pa^{-0.75}$
C_D	Orifice calibration coefficient	Pa^{-1}
C_E	Orifice calibration coefficient	$Pa^{-1.25}$
C_{Or}	Flow coefficient of orifice	m^2
c_p	Specific heat capacity at constant pressure	$kJ/(kg \cdot K)$
c_v	Specific heat capacity at constant volume	$kJ/(kg \cdot K)$
$C_{Venturi}$	Flow coefficient of venturi tube	m^2
$\dot{C}_W$	Heat capacity increase	$kJ/(K \cdot s)$
d	Diameter	m
D	Inlet and outlet diameter	m
d_0	Discharge diameter	m
d_i	Inner diameter	m
d_o	Outer diameter	m

h	Enthalpy	kJ/kg
I_{C}	Condensation/Desublimation mass flux	$\mathrm{kg/(m^2 \cdot s)}$
I_{E}	Evaporation/Sublimation mass flux	$\mathrm{kg/(m^2 \cdot s)}$
I_{p}	Electric current, raw data measured with a pressure transmitter	A
J	Current density	$\mathrm{A/m^2}$
k	Coverage factor (GUM)	-
k_{Des}	Desublimation coefficient	m/s
K_{dr}	Certified discharge coefficient	-
K_{Vent}	Flow rate coefficient	-
l	Length	m
L'	Specific heat input	kJ/kg
m	Mass	kg
M	Molar mass	kg/kmol
$\dot{m}$	Mass flow rate	kg/s
$\dot{m}_{\mathrm{Cr}}$	Change of mass inside the cryogenic vessel	kg/s
$\dot{m}_{\mathrm{Dep}}$	Deposition mass flow rate	kg/s
$\dot{m}_{\mathrm{Des}}$	Desublimation mass flow rate	kg/s
$\dot{m}_{\mathrm{In}}$	Venting mass flow rate	kg/s
$\dot{m}_{\mathrm{Out}}$	Discharge mass flow rate	kg/s
$\dot{m}_{\mathrm{v}}$	Evaporating mass flow rate	kg/s
n	Number of a quantity	-
N	Number of quantities (GUM)	-
p	Pressure	bar
p_0	Relieving pressure (safety relief valve)	bar(g)
p_{b}	Back pressure (safety relief valve)	bar(g)
p_{open}	Opening pressure (safety relief valve) under experimental conditions	bar(g)
p_{S}	Maximum allowable working pressure	bar(g)
p_{set}	Set pressure (safety relief valve) under service conditions	bar(g)
$\dot{q}$	Heat flux	$\mathrm{W/m^2}$
$\dot{Q}$	Heat flow	W
r	Radius	m
R	Universal gas constant	$\frac{\mathrm{kg \cdot m^2}}{\mathrm{s^2 \cdot mol \cdot K}}$
$R_{\alpha\mathrm{WCr}}$	Thermal resistance between the cryogenic vessel wall and the cryogenic fluid	K/W
$R_{\lambda\mathrm{Dep}}$	Thermal resistance within the layer of deposited venting fluid	K/W
$R_{\lambda\mathrm{W}}$	Thermal resistance within the cryogenic vessel wall	K/W
R_{T}	Electric resistivity, measured with a temperature sensor	Ω
R_{tot}	Total thermal resistance	K/W
R_{V}	Specific gas constant of the venting fluid	$\mathrm{J/(kg \cdot K)}$
s	Thickness	m

s_i	Datapoint	-
S	Sensitivity of a sensor	
T	Absolute temperature	K
$\bar{T}$	Average temperature	K
u	Specific internal energy	kJ/kg
u_i	Measurement uncertainty of i	
u_A	Measurement uncertainty of Type A (GUM)	
u_B	Measurement uncertainty of Type B (GUM)	
u_C	Combined measurement uncertainty (GUM)	
U_He	Helium internal energy	kJ
U_T	Voltage, raw data measured with a temperature sensor	V
v	Specific volume	$\mathrm{m^3/kg}$
V	Volume	$\mathrm{m^3}$, L
v_l	Specific volume of saturated liquid	$\mathrm{m^3/kg}$
v_v	Specific volume of saturated vapour	$\mathrm{m^3/kg}$
w	Velocity	m/s
x	Coordinate	m
x_i, y_i	Estimate of value (GUM)	
X_i, Y_i	Value of measurand (GUM)	
y	Mole content	

Greek symbols

Symbol	Quantity	Unit
α_C	Condensation coefficient, sticking coefficient	-
$\alpha_\mathrm{C,eff}$	Effective condensation coefficient	-
α_E	Evaporation coefficient	-
α_T	Transmission coefficient	-
α_w	Discharge coefficient	-
α_WCr	Heat transfer coefficient between the cryogenic vessel wall and the cryogenic fluid	$\mathrm{W/(m^2 \cdot K)}$
β	Diameter ratio	-
Δ	Difference	-
Δh_V	Enthalpy of evaporation	kJ/kg
Δh_Sub	Enthalpy of sublimation	kJ/kg
Δh_Sens	Sensible enthalpy difference	kJ/kg
ϵ	Emissivity	-
ϵ_0	Electric constant	F/m
ϵ_Or	Expansion coefficient of orifice	-
ϵ_r	Relative permittivity	-
$\epsilon_\mathrm{Ventrui}$	Expansion coefficient of Venturi tube	-
ζ	Molar content	mol%
κ	Isentropic exponent	-
λ	Thermal conductivity	$\mathrm{W/(m \cdot K)}$

λ_{Dep}	Thermal conductivity of the deposited venting fluid	$\mathrm{W/(m \cdot K)}$
λ_{W}	Thermal conductivity of the cryogenic vessel wall	$\mathrm{W/(m \cdot K)}$
Ψ	Discharge function	-
ρ	Density	$\mathrm{kg/m^3}$
$\bar{\rho}$	Average density	$\mathrm{kg/m^3}$
θ	Parameter for determining discharge mass flow rate	kJ/kg
τ	Time	s

Indices

Symbol	Quantity
0	At a certain point ($\tau = 0$)
a	Arithmetic mean
A	Ambient
Ar	Argon
b	Boiling point
C	Critical (superconductivity)
Cal	Calibration
Cr	Cryogenic vessel, cryogenic fluid
Crit	Critical (thermodynamics)
CS	Current source
Cyl	Cylinder
Dep	Deposition (desublimation, condensation), deposited venting fluid
Des	Desublimation
end	At the end of a time step
g	Gaseous
H2O	Water
He	Helium
i	Index of list element
In	Flowing in
interpol	Interpolated
Iso	Supply isolator
l	Liquid
λ	At the lambda point
ha	Humid air
LHe	Liquid helium
max	Maximum
n	Index of summation
N2	Nitrogen
nb	Normal boiling point
O2	Oxygen
Offset	Offset of signal
open	When safety relief valve opens
Or	Orifice
Out	Flowing out

s	Solid
Sat	Saturation
Strd	At standard conditions
T	Temperature
tot	Total
Trans	Transmission
Trip	Triple point
Tube	Of a tube
V	Vacuum vessel, venting fluid
Vent	Venting section
Venturi	Venturi tube
VDep	At the interface between vacuum space and deposited venting fluid
W	Cryogenic vessel wall
WCr	At the interface between cryogenic vessel wall and cryogenic fluid

Abbreviations

Abbreviation	Meaning
ADC	Analog-to-digital converter
bar(a)	Bar absolute
bar(g)	Bar gauge
BT	Bubble test
CEA	French Alternative Energies and Atomic Energy Commission
CERN	European Organization for Nuclear Research
DAQ	Data acquisition system
f	Function of
FMECA	Failure mode effects and critical analysis
GUM	Guide to the Expression of Uncertainty in Measurement
HAZOP	Hazard and operability study
He	Helium
IAD	Initial audible discharge
ITEP	Institute for Technical Physics at KIT
KIT	Karlsruhe Institute of Technology
LHC	Large Hadron Collider
LHe	Liquid helium
LI	Liquid level probe
LIV	Loss of insulating vacuum
MCA	Maximum credible accident
MLI	Multilayer insulation
MI	Humidity probe
MP	Measurement point
N_2	Nitrogen
P&ID	Piping and Instrumentation Diagram
PED	European Pressure Equipment Directive
PDI	Differential pressure transducer

PI	Pressure transducer, absolute or relative
PICARD	Name of a test facility
PLC	Programmable logic controller
sc.	Superconducting
s-l	Solid-liquid
TI	Temperature sensor
TVO	Carbon resistance thermometers

Acknowledgements

I would like to take the opportunity to thank the people whose contributions and support have been invaluable for this project.
First, I would like to express my sincere gratitude to my advisor Prof. Dr.-Ing. Steffen Grohmann who gave me the opportunity to continue research on cryogenic safety after my Diplomarbeit and who introduced me to this great scientific environment. His continuous support and advice during both my Diplomarbeit and PhD thesis have been greatly appreciated.
I would also like to thank Prof. Dr.-Ing. Thomas Wetzel for his interest in this thesis and for agreeing to act as a second examiner.
I would like to express my gratitude towards the technical staff at ITEP, especially Uwe Fuhrmann, Didier Holländer, Eugen Specht and Michael Stamm who untiringly helped me with the design, construction and assembly of the PICARD test facility. Their motivation, expertise and their readiness to do their magic even if it was already Friday afternoon was what made the work on this project so very special.
For friendly support with their ideas and experience I would like to express my thanks to Ingeborg Meyer, Ralf Müller, Alexander Reiner, Heinz Schön and the whole ITEP Cryo-group as well as the ITEP administration and IT support.
Furthermore, I would like to thank Andre Henriques of CERN for the fruitful collaboration and the KSETA graduate school for the support.
For the many helpful discussions, encouragement and for proofreading the draft of this thesis I would like to thank David Gomse, Andreas Janzen, Jana Stengler, Christina Weber, Dr. Max Zoller and Christopher Zoller-Blundell. Besides, I would like to thank Nicole Barkholz, Ariane Bisten, Jana Stengler and Simone Wolff for the many convivial dinners.
Last but not least I would like to thank my family and friends, in particular Max Zoller, Christian Heidt, Gerdi and Ekkehard Heidt, Waltraud and Udo Lauther, Annette and Bruno Zoller, Lisa-Marie and Christopher Zoller-Blundell, who always support me and make me happy.